Mechanochemistry of collagen network remodeling in the sclera

by
Michelle L. Chen

A dissertation submitted to The Johns Hopkins University
in conformity with the requirements for the degree of
Doctor of Philosophy

Baltimore, Maryland
February, 2019

Abstract

The primary load-bearing tissue of the eye is the sclera, the eye's white outer shell. It helps the eye maintain its shape by resisting intraocular pressure and protects the delicate intraocular structures. The sclera is able to respond to mechanical changes in its environment by adapting to its environment, a process known as remodeling. This process, which alters the microstructure and/or properties of the tissue, can occur over the normal course of aging or under physiological conditions but may also contribute to pathological diseases such as glaucoma and myopia when an imbalance in the remodeling process occurs. It is therefore important to understand the underlying mechanisms that drive the remodeling process, and how it affects tissue microstructure and its mechanical properties. This work focuses on two main parts of the connective tissue microstructure: collagen, which serves as the primary load-bearing component and dominates the anisotropic large-strain mechanical response of the tissue, and glycosaminoglycans (GAGs), which regulate the spacing between collagen fibrils and help determine tissue hydration. The objective of this work is to study the effect of remodeling on mechanical behavior of the posterior sclera. We investigate this through three case studies.

The first part of this work studies the mechanical role of GAGs in the human posterior sclera. Although alterations in mechanical properties and GAG content have been reported in glaucomatous eyes, it is unknown if the change in GAG content directly contributes to the observed changes in mechanical properties. Experimental protocols and analysis methods

were developed for determining the inflation response of posterior human sclera, measured before and after enzymatic GAG degradation. It was shown that GAGs play a measurable role in altering the structural response and mechanical behavior of the posterior human sclera, likely through their effects on hydration and their interactions with the collagen fibrils.

The second case study investigates how cyclic preconditioning of a collagenous substrate induces material property changes and morphological changes in collagen fibrils. Experimental studies have shown that repeated cyclic loading of an acellular collagen construct increased collagen stiffness, but did not significantly change fibril anisotropy. A model for the collagen fibril substrate was developed to show that the changes in the collagen anisotropy measured in experiments were insufficient to explain the measured increase in the stiffness of the collagen constructs with cyclic loading. The findings suggest that mechanical loading can induce changes in the stiffness and failure properties of the collagen fibril network through passive chemomechanical processes.

The last part of this work examines the effect of changes in the geometry of the sclera, collagen anisotropic structure, and material properties from glaucoma on the inflation response of the mouse sclera. An inverse finite element method was used to fit model parameters describing fibril properties to the average measured scleral edge displacements of glaucoma and normal mouse eyes. The findings show that changes in collagen fibril material properties were responsible for the observed stiffening effect in glaucoma mouse eyes. The observed structural changes associated with glaucoma did not meaningfully stiffen the mechanical response.

Thesis Committee

Primary Reader:

Thao D. (Vicky) Nguyen
Professor
Marlin U. Zimmerman Jr. Faculty Scholar
The Johns Hopkins University
Department of Mechanical Engineering

Secondary Readers:

Jeffrey W. Ruberti
Professor
Northeastern University
Department of Bioengineering

Kaliat T. (K.T.) Ramesh
Professor
Alonzo G. Decker Jr. Professor of Science and Engineering
The Johns Hopkins University
Department of Mechanical Engineering

Acknowledgments

This work would not have been possible without the continuous support and guidance of my advisor, Professor Vicky Nguyen. She gave me the opportunity to join her group despite having no prior background in either mechanical engineering or biology, and provided the funding for my studies and research. It is through her mentorship and diligence that I have grown as a scientist and researcher. I would like to extend my gratitude to Professor Jeffrey Ruberti for his guidance and insight on collagen network remodeling. I would also like to thank the readers of this dissertation, Professors Vicky Nguyen, Jeffrey Ruberti, and KT Ramesh for their time and attention.

I am grateful to everyone who has helped me accomplish this research. Dr. Barbara Murienne, who developed the s-GAG degradation protocol, and patiently trained me on the inflation experiments. Dr. Monica Susilo, Cathy Nguyen, Professor Harry Quigley, Professor Kristin Myers, Professor Katia Genovese, and Professor Craig Boote, all generously shared their code, data, and methods. Thank you.

I thank my labmates, past and present, for their many interesting and productive conversations throughout the research process: Barbara Murienne, Aurelie Azoug, Dan Midgett, Jingkai Guo, Bahram Notghi, Zheng Jia, Jiayu Liu, Tracy Ling, Zheliang Wang, Cristina Martin Linares, Arina Korneva, and Cameron Czerpak.

Thank you to everyone who has provided friendship and support over the years, in particular Joel Bretheim, Gianna Valentino, Tracy Ling, Zoe Hendrickson, Carl Shapiro, Alessan-

dro Gnoli, Daniel Case, and Danielle Barnette.

Finally, I would like to thank my family, my parents Minhua and Changyi, and Daniel Willen for their unwavering love and encouragement.

Table of Contents

List of Tables

List of Figures

Chapter 1

Introduction

This chapter provides a background on the anatomy, structure, and function of the sclera. Particular attention is paid to the mechanical behavior of the sclera and its microstructure. The sections below summarize the methods typically used to characterize the mechanical response of the sclera and its material properties: how the scleral structure and properties can change in response to alterations to the mechanical environment; and highlights its importance in pathologies such as glaucoma and myopia. The chapter concludes with the objectives of this work.

1.1 The sclera

1.1.1 The sclera as part of the eye

The human eye is the sensory organ and optical system that enables vision. Light entering the eye is transformed into electrical signals, which are then transmitted to the brain and interpreted to form a visual image. This occurs as light enters the eye through the cornea and is refracted by the lens, which can adjust its curvature to change the focal distance of the eye (Fig. 1.1). The light is focused on the retinal surface in the posterior portion of the eye, where photoreceptors convert the photons to electrical signals to the retinal ganglion cells (RGC). The RGC axons exit the eye through the optic nerve head (ONH), a structure

in the back of the eye wall, and form an optic cable that connect to the visual cortex of the brain.

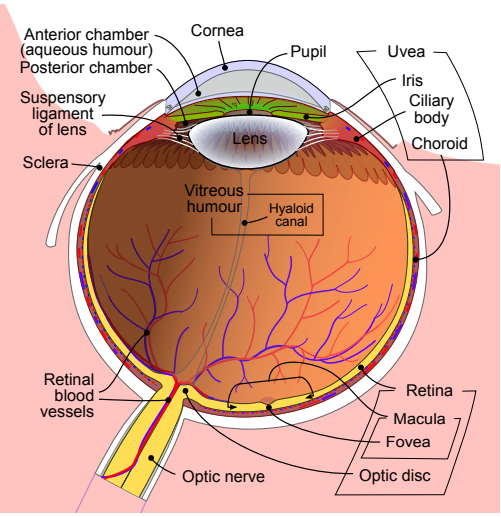

Figure 1.1: Schematic of the human eye. The light enters the eye through the cornea and is focused on the retina by the cornea and lens. Diagram by Rhcastilho and Jmarchn, distributed under a CC-BY 2.0 license.

The eye can experience a wide range of external and internal loads. Internally the intraocular pressure (IOP) ranges between 10-21 mmHg in healthy humans [140], and can be as high as 50 mmHg in eyes with ocular hypertension[128]. To achieve a focused retinal image, the internal components of the eye need to be protected from external loading, and fluctuations in IOP. This is the primary responsibility of the sclera, the white outer shell of the eye that constitutes 80% of the eye wall [164], and serves as the main load-bearing structure of the eye.

Anteriorly, the sclera is connected to the cornea, and is posteriorly connected to the ONH. The junction between the sclera and the cornea is known as the limbus, and the the region where the sclera meets the ONH is known as the peripapillary sclera. Within the ONH, spanning the scleral canal, is the lamina cribrosa (LC). The LC helps mechanically support the RGC axons as they exit the eye.

The healthy human sclera is approximately spherical and has an average diameter of 24.4 mm [10]. Its thickness varies from 0.8 mm near the limbus, to its thinnest portion 0.4-0.6 mm near the equator, and to its thickest portion about 1.0 mm near the ONH [164]. Moreover, at the posterior pole, the superior and temporal quadrants in humans have been shown to be thicker than the inferior and nasal quadrants [111].

1.1.2 Microstructure of the scleral connective tissue

The extra-cellular matrix (ECM) of the scleral tissue consists of a collagen fiber network embedded in a compliant ground matrix interwoven with elastin fibers and proteoglycans with their associated glycosaminoglycans (GAGs). These components are created by scleral fibroblasts, which help maintain the ECM [1].

Collagen

Collagen is the most abundant protein in the ECM. It accounts for 80% of the dry weight in the sclera [8]. Collagen in the sclera are primarily fiber-forming (type I, 90% and type III, $\leq 5\%$) [169] and have a complex hierarchal structure (Fig. 1.2).

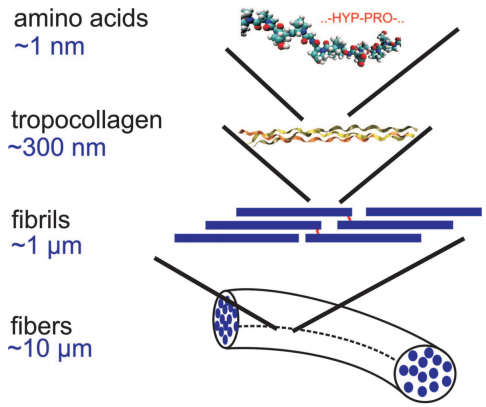

Figure 1.2: Hierarchy of collagen structure. Reprinted from Buehler 2006 with permission (Copyright (2006) National Academy of Sciences, USA.)[18].

Triple-helical structures, made up of polypeptide strands, form tropocollagen molecules.

The tropocollagen are arranged in staggered arrays to form fibrils, which then pack into fibers [18]. The collagen fibrils in the sclera exhibit a small intrinsic crimp [68, 64], and are aligned in parallel to form lamellae [174] (Fig. 1.3). The lamellae branches, interweaves, and superimposes on itself to form a dense network structure, with most of the fibril bundles lying parallel to the surface of the sclera [169].

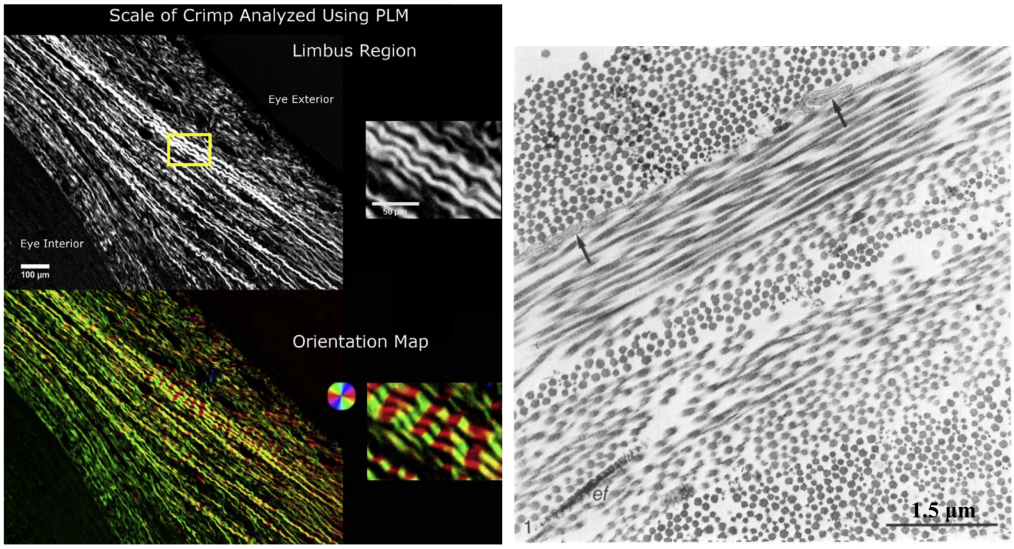

Figure 1.3: (Left) Crimped collagen from sheep eyes at the limbus region, via polarized light microscopy. Reprinted from Jan et al. 2018 with permission from [77]. (Right) Fibrils arranged in lamellar structure in rabbit sclera, via electron microscopy. Reprinted from Young 1985 with permission from the Journal of Cell Science [174].

There are two regions where collagen is highly oriented in the sclera: around the ONH, the fibril bundles are circumferentially aligned [91], and near the limbus where the fibrils circumscribe the cornea [14, 109] (Fig. 1.4). The diameter of the collagen fibrils vary through the scleral thickness, from 58 nm to 160 nm in the outer sclera, and from 50 nm to 76 nm in the inner sclera [174].

Elastin

Elastin comprise approximately 2% of the dry weight of the sclera [138, 100]. Elastin fibers are interwoven throughout the collagen network and supplement the tissue's extensibility.

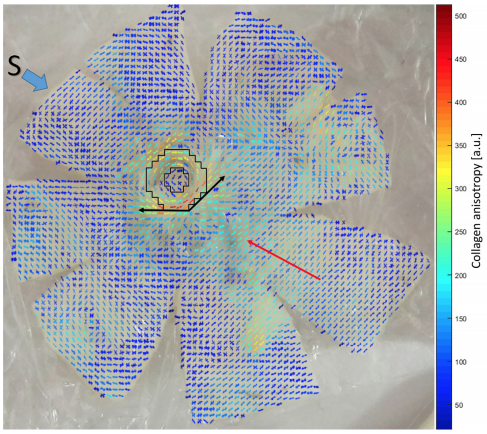

Figure 1.4: Polar plot of preferential collagen orientation in the human posterior sclera obtained by wide-angle X-ray scattering (WAXS). Warmer colors indicate higher degrees of anisotropy. Reprinted from Markov et al. 2018, distributed under a CC-BY 3.0 license [91].

The fibers are composed of an amorphous elastin core that is encased by longitudinally aligned microfibrils [81]. Although elastin has the longevity of a human lifespan [150], its properties change with age. The diameter of the scleral microfibrils increases, and the elastin core becomes more dense with age [80]. The presence of elastin in the sclera only exists in the limbus and peripapillary sclera. Elastin fibers in the peripapillary region encircle the ONH with a 300 μm region [129]. Beyond this region, the density of elastin decreases and can only be found in the inner sclera. The fibers remain parallel to the scleral surface, but show no preferential orientation [58].

Proteoglycans and glycosaminoglyans

Proteoglycans occupy the interfibrillar space in the scleral ECM, where they influence the hydration of the tissue [164], regulate fibrillogenesis [166, 134], and help maintain the structural integrity of the collagen network [135]. Proteoglycans are composed of a protein core covalently attached to one or more branches of GAGs, polysaccharide chains of repeating disaccharide units. These core proteins can attach to collagen fibrils, allowing the proteoglycans to interweave between fibrils, or attach two adjacent fibrils together (Fig. 1.5) [87, 174].

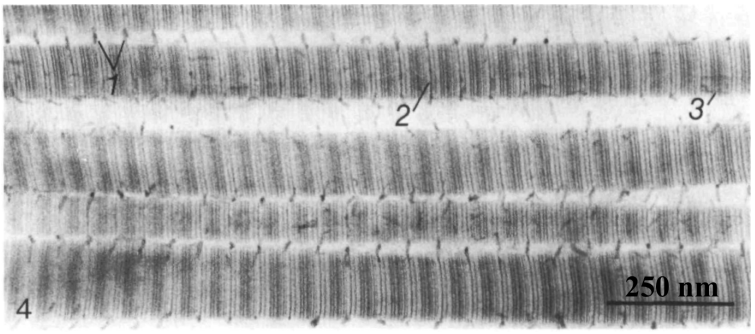

Figure 1.5: Longitudinal sections of collagen fibrils in rabbit sclera. Proteoglycancs can be seen at (1) extending from the fibrils, and interconnecting neighboring fibrils (2) encircling the fibril (3) lying in parallel with the fibril. Images taken via electron microscopy. Reprinted from Young 1985 with permission from the Journal of Cell Science [174].

Although the proteoglycan core proteins and their associated GAG side chains make up less than 3% of the dry weight of the sclera, they are responsible for 70% water content in the sclera [164]. GAGs are anionic and attract positively charged ions that create local concentration gradients which in turn, attract water molecules via osmosis [47, 87]. These additional water molecules occupy volume between collagen fibrils and force the fibrils farther apart [87]. However, this swelling is balanced by the collagen network elasticity [96] and a thermal motion that causes the proteoglycans to vibrate, thereby decrease the end-to-end distance of the proteoglycan [87].

The adult human sclera contains mainly 3 proteoglycans: decorin, biglycan, and aggrecan [135]. Decorin and biglycan are small proteoglycans with protein cores of $\approx$ 45kDa and contain one or two chondroitin-dermatan sulfate GAG side chains, respectively. Aggrecan has a core protein size of $\approx$ 350kDa with over a hundred chondroitin sulfate chains and tens of keratan sulfate chains [135][88]. Decorin and biclycan can be found distributed throughout the sclera, and decorin has been shown to bind to type I collagen and affect fibrillogenesis [166]. Aggrecan is found in the highest concentration in the posterior sclera [136], and with its numerous hydrophilic GAG side chains, provide the tissue with increased hydration [16] and resistance to compressive forces [102].

1.1.3 Mechanical properties

The mechanical properties of the sclera are governed by the properties of its microstructure, and from a mechanistic viewpoint, the sclera can be thought of as a fiber-reinforced substrate. The preferential alignment of the fibers, their morphology, and their composition directly inform the non-linear stress-strain behavior of the tissue.

Like other collagenous tissues, the stress-strain curve of the sclera is anisotropic and has a distinctive "J-shaped" curve [54, 73] (Fig. 1.6). At small strains, the collagen fibrils are still crimped, and the mechanical behavior is determined by the ground matrix of proteoglycans and elastin. Elastin helps the sclera resist deformation and is responsible for scleral elasticity. Compared to collagen, elastin is stiffer at low strains, but more compliant at high strains [73]. The retention of water by proteoglycans and GAGs give the sclera compressive stiffness, making it nearly incompressible [49]. GAGs may also affect mechanical behavior of the sclera through their interactions with collagen fibrils [143]. The direct mechanical role of GAGs in the sclera is still not well understood, but enzymatic removal of GAGs in young porcine sclera has been shown to made the tissue more compliant [105].

As strain increases, the collagen fibrils straighten and carry load, causing the scleral tissue to stiffen. Tissues with a dominant collagen fibril orientation exhibit a stiffer stress-strain response in the dominant direction, than in the in-plane orthogonal direction. This behavior may protect the tissue from being stretched beyond physiological levels. In the sclera, the circumferential arrangement of fibrils around the ONH and limbus mechanical reinforces tissue, resisting expansion of the ONH opening and maintaining the curvature of the cornea [129, 109]. Collagen can cause additional stiffening in the tissue through cross-linking [147].

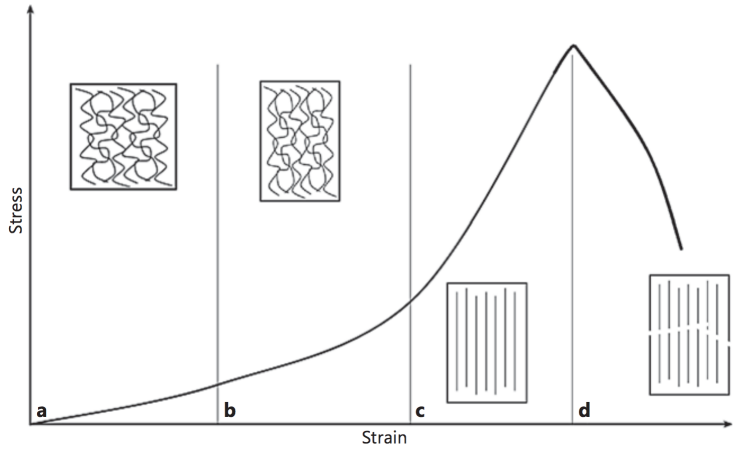

Figure 1.6: Schematic of a stress-strain curve for typical collagenous tissue and corresponding collagen fibril microstructure (a) toe region (b) heel region (c) linear region (d) failure. Reprinted from Aziz et al. 2016 with permission from [7].

1.1.4 Mechanical testing method

Numerous experimental techniques have been used to investigate the mechanical behavior of the sclera, including uniaxial tests [48, 25], biaxial tests [45], indentation tests [9], and inflation tests [107, 35]. The different experimental methods have not produced consistent results, rather they reported a range of scleral material properties spanning several orders of magnitude [21]. While uniaxial and biaxial loading are straight-forward testing methods, they are not representative of the *in vivo* loading state of the sclera. Not only do these techniques involve the severing of collagen fibrils at tissue boundaries and flattening of the scleral shell in preparing the samples for testing, but they also demonstrate preconditioning effects. In preconditioning, collagen fibrils rearrange in the direction of stress in the first few load-unload cycles, causing the stress-strain curve to shift rightward and the strip to permanently lengthen [163] (Fig. 1.7). Inflation tests of the sclera better mimic the *in vivo* loading state than uniaxial and biaxial tests, and effects of the stress concentrations at the boundaries of the fixture are considered negligible away from the fixture. Moreover, it has been shown that inflation tests incur minimal preconditioning effects [160].

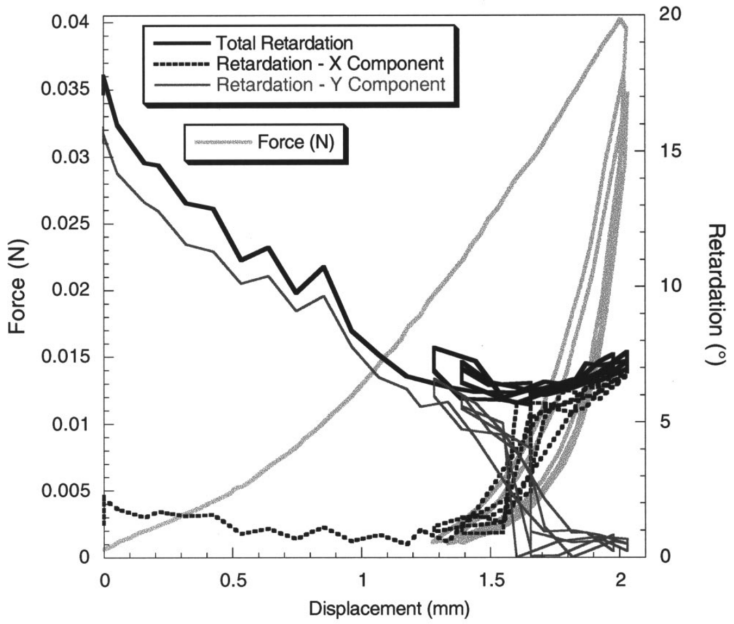

Figure 1.7: Retardation versus displacement and force versus displacement curves for a tissue construct that is subjected to three preconditioning cycles to zero force. The initial fiber alignment of the construct is perpendicular to the loading direction.The change in retardation reflects the change in fiber realignment with preconditioning. Reprinted from Tower et al. 2002 with permission from [163].

1.2 Constitutive models

Constitutive models are commonly used to characterize the nonlinear, anisotropic mechanical behavior of the sclera. Typically, the sclera is modeled as a hyperelastic material. The deformation gradient, $\mathbf{F} = \frac{\partial \varphi(\mathbf{X})}{\partial \mathbf{X}}$, which maps the undeformed configuration to the deformed configuration, describes the kinematics of the tissue. In the theory of hyperelasticity, the material does not dissipate energy, and therefore the Cauchy stress, σ, can be derived from a strain energy density function, Ψ, for any deformation state

$$\sigma = \frac{2}{J}\mathbf{F}\frac{\partial \Psi\left(\mathbf{C}\right)}{\partial \mathbf{C}}\mathbf{F}^{\mathrm{T}} \tag{1.1}$$

where $J = \det\left(\mathbf{F}\right)$ is the Jacobian of the deformation gradient and $\mathbf{C} = \mathbf{F}^{\mathrm{T}}\mathbf{F}$ is the right

Cauchy-Green tensor. The Lagrange strain tensor $\mathbf{E}$, is defined as half the difference of the right Cauchy-Green and the identity matrix $\mathbb{I}$,

$$\mathbf{E} = \frac{1}{2}\left(\mathbf{C} - \mathbb{I}\right) \tag{1.2}$$

To ensure material frame indifference (i.e. objectivity), the strain energy density is written in terms of invariants of $\mathbf{C}$ (i.e. $I_1 = \mathrm{tr}\left(\mathbf{C}\right)$, $I_2 = \frac{1}{2}\left(\mathrm{tr}\left(\mathbf{C}\right)^2 - \mathrm{tr}\left(\mathbf{C}^2\right)\right)$, $I_3 = \det\left(\mathbf{C}\right)$).

Attempts at determining constitutive models for soft tissues have resulted in numerous expressions for the strain energy density functions. Early attempts at capturing the non-linearity and anisotropy characteristics of soft tissues include Fung [56, 159], which assume an exponential form for the strain energy density. While computationally simple, the parameters for such a model do not have a physical interpretation, and the model is purely phenomenological. This motivated the development of models that incorporate the tissue microstructure in the mechanical response. Lanir [85] proposed that by assuming an affine deformation (i.e. the same deformation gradient is applied for all components of the tissue), the strain energy density contribution can be additively decomposed into an isotropic ground matrix contribution and an anisotropic collagen fiber contribution,

$$\Psi\left(\mathbf{C}\right) = \Psi_{matrix}\left(\mathbf{C}\right) + \Psi_{fibers}\left(\mathbf{C}\right) \tag{1.3}$$

The matrix is usually represented as an isotropic, quasi-incompressible Neo-Hookean material,

$$\Psi_{matrix}\left(\mathbf{C}\right) = \frac{\mu}{2}\left(\bar{I}_1\left(\mathbf{C}\right) - 3\right) + \Psi_{vol}\left(I_3\left(\mathbf{C}\right)\right) \tag{1.4}$$

where μ is the shear modulus of the matrix, $\bar{I}_1 = I_3^{-\frac{1}{3}} I_1$ the distortional component of I_1, and Ψ_{vol} the volumetric component.

For tissues where the fibers are mainly in the plane, collagen distribution in the tissue can be modeled as a probability density distribution of preferential orientation, $\rho(\theta)$. Then, the anisotropic collagen contribution can be written as the integral sum of individual fiber contributions across all orientations, $-\pi \leq \theta < \pi$,

$$\Psi_{fibers}(\mathbf{C}) = \int_{-\pi}^{\pi} \Psi_{fib}(\theta)\, \rho(\theta)\, d\theta. \tag{1.5}$$

The fiber strain energy contribution, Ψ_{fib}, have been described phenomenologically, usually in the form of an exponential function [121, 37]. Micro-mechanical models have also been developed to provide a more detailed description of collagen fiber structure and deformation. These models assume the collagen fiber to be a linear elastic material, and use the straightening of the fiber to give rise to the characteristic nonlinear behavior. Typical model parameters include initial crimp angle, fiber morphology, and elastic stiffness of the fiber. Examples of such micro-mechanical models include Comninou and Yannas [28], who represent the collagen fibers as thin planar sinusoidal beams and Grytz and Meschke [63], who represent the fibers as extensible helical springs. These more detailed models and extra parameters come at computational expense, and only recently have studies incorporating micro-mechanical fiber models into tissue models emerged [162, 65, 64].

Although viscoelastic models have been used to capture the sclera's stress relaxation behavior [44], in this work only the elastic properties of the sclera will be discussed.

1.3 Scleral remodeling

Thus far, the scleral tissue has been considered a passive material with static properties. However, the sclera is a dynamic tissue whose structure and collagen network properties can be altered in response to changes its environment. In turn, these changes can give rise to alterations in mechanical properties, in a process known as remodeling [94, 136]. While

remodeling can occur over the normal course of aging or under physiological conditions, a disruption or imbalance in the remodeling process may give rise to disease states such as glaucoma or myopia [66].

Glaucoma is the second-leading cause of blindness in the world [142], and is characterized by the progressive damage and death of RGC axons in the scleral canal, causing irreversible vision loss [124]. While glaucoma and its severity are strongly correlated with high levels of IOP in the eye [22, 113], patients with IOP lower than 21 mmHg still develop glaucoma [125]. Burgoyne et al. [19] hypothesized that imbalances in the remodeling process may alter the scleral mechanical properties such that even at physiological levels of IOP, pathological levels of stress at the ONH occur.

Glaucoma eyes have different mechanical properties and structure than normal healthy eyes. In animal [44, 110] and human [35] studies, the posterior sclera from glaucoma eyes were shown to have a stiffer strain response than normal eyes. Glaucoma eyes in monkeys [43] and mice [110] also had thinner scleral shells. Recently, there have also been studies explicitly characterizing the change in collagen fiber network in glaucoma and normal eyes [119, 37, 120]. While the preferential collagen fiber orientations in glaucoma eyes and normal eyes were both circumferential around the ONH and limbus, the fiber orientation was less aligned in glaucoma eyes [119, 120, 129]. The total content of fiber-forming types of collagen, primarily type I collagen, was also slightly lower than normal eyes[120].

Myopia, colloquially known as near-sightedness, most commonly occurs when the globe of the eye abnormally elongates axially, causing the the retina to lie behind the focal plane. The axial elongation is commonly accompanied by other structural changes such as scleral thinning and a reduction of collagen fibril diameters [138]. Type 1 collagen content is reduced, as is GAG content [112]. Phillips et al. [118] demonstrated that myopic eyes in tree shrews have different viscoelastic properties than normal eyes via an increased creep rate, defined

as percent extension under constant tension. Simulations run by Grytz and Siegwart Jr. [64] found that the changes in axial elongation rate in myopic tree shrew sclera could be temporally associated with changes in the crimp angle of scleral collagen fibrils, suggesting that the axial elongation may be controlled by a remodeling mechanism that also controls collagen fibril crimp.

It has been shown that the sclera remodels in response to changes in stress. Specifically, scleral fibroblasts can sense changes in mechanical stimuli and alter the surrounding ECM composition. When human scleral fibroblasts were biaxially stretched by Shelton and Rada [151], they found increased production of metalloproteinases (MMPs), proteins responsible for collagen degradation initiation, and decreased production of proteins that regulate MMPs, TIMP-2 mRNA. Their findings suggest that mechanical strain could contribute to scleral ECM degradation and scleral thinning. Similarly, Fujikura et al. [55] also found increased MMP activity in embryonic chick scleral fibroblasts subjected to pulsatile mechanical stretch. Cui et al. [39] tracked the changes in gene expression of human scleral fibroblasts induced by mechanical stretching. After stretching for 30 minutes, they measured 237 genes with significant changes in expression, including 28 unexpressed genes that turned on, 31 expressed genes that turned off, and 25 genes that showed a three-fold change in expression. Among these are genes that control protein synthesis in the ECM. After stretching for 24 hours, 308 genes showed a significant change in expression. These results imply that the sclera is continuously remodeling, degrading and producing ECM components, in response to its mechanical environment.

Recent studies have shown that remodeling can occur through passive chemomechanical mechanisms in acellular tissue constructs. Stretch-mediated enzymatic degradation of collagen fibrils has been shown to alter the anisotropic structure of collagen networks [51, 74, 13, 175]. Flynn et al. [51] found that collagen fibrils exposed to MMPs under ap-

plied mechanical strain were shown to have a longer degradation time than unloaded collagen fibrils exposed to MMPs. This suggests that mechanical strain can stabilize collagen fibrils aligned with the loading direction against degradation, but fibrils oriented away from the loading direction are degraded. In a study by Susilo et al. [156], acellularized collagen tissue constructs are preconditioned with different number of cycles and at different strain levels, before being loaded in uniaxial tension to failure. The findings showed that cyclic loading induced a stiffening effect, measured as an increase in the slope of the linear portion of the strain-stiffening stress response, on the collagen constructs, and a permanent elongation of the specimen.

1.4 Objective of this work

Characterizing how the scleral structure and properties change during remodeling is essential to understanding the pathophysiology of diseases such as glaucoma and myopia. Although there is a broad consensus that remodeling processes take place in the sclera, we still do not fully understand the structural and mechanical impact that these processes have. Namely, there is a disconnect in understanding the implications of tissue-level changes on fiber-level properties and vice versa, the implications of fiber property changes on tissue-level response. While it is known that the mechanical environment of the sclera can alter collagen network properties, we have very little knowledge about how specific collagen fiber properties are altered (e.g. fiber stiffness, fiber morphology, spatial orientation) or which properties are most affected. Nor is the problem well understood in the opposite direction: while it has been shown that mechanical stimuli can affect ECM chemistry and composition, there have been few studies investigating how the altered ECM changes the mechanical behavior of the posterior sclera. A better understanding of the multi-scale effects of remodeling could lead to development of better diagnostics and new treatments of glaucoma and myopia.

To improve our understanding of the mechanochemistry of collagen network remodeling in the sclera, we are broadly interested in the following:

1. How changes in the ECM composition influence the mechanical response of the tissue
2. How changes in mechanical load affect the collagen network properties
3. How properties of the collagen network affect the mechanical response of the tissue

However, a thorough investigation of this is beyond the scope of this thesis. Instead we present three case studies, each addressing one of the above. The objective of these case studies are:

1. Determine the mechanical contribution of GAGs to the inflation response of the posterior human sclera
2. Investigate whether cyclic loading affects collagen fibril-level mechanical properties
3. Evaluate how changes in material and structural properties from glaucoma affect the simulated inflation response in mouse eyes

Each of the following chapters addresses one of these case studies and includes its individual relevant literature review and discussion.

Chapter 2 quantifies the mechanical and structural changes in human posterior sclera upon the enzymatic degradation of GAGs. This was a collaborative work with Dr. Barbara Murienne, who had previously examined the mechanical role of GAGs in porcine sclera. However, there was motivation to examine this response in humans, as this would be more relevant to the understanding of glaucoma. Older humans have a stiffer sclera than young pigs, and the experimental design had to be improved to accurately measure the smaller displacements during inflation testing. This chapter details the adaptation of the experimental and analysis method from porcine to human donor tissue, and the differences in findings.

Chapter 3 develops an anisotropic micromechanical model to investigate changes in collagen fibril properties of an engineered collagen material following cyclic loading. A previous experimental study demonstrated that cyclic loading of acellular collagen constructs caused significant stiffening and strengthening. The model was used to investigate whether the measured tissue-level changes can be attributed to changes in the anisotropic collagen structure or mechanical properties of the collagen fibrils. The latter implies that cyclic mechanical loading can induce collagen network changes through chemomechanical processes separate from those of cells.

Chapter 4 applies the model developed in the previous chapter to an inverse finite element analysis to characterize how changes in material properties and structure from glaucoma affect the inflation response of mouse eyes. Experimentally, glaucoma mouse sclera have a stiffer pressure-strain response than normal mouse sclera and exhibit a less anisotropic collagen fiber structure. The model was fit to the inflation test data of normal mouse sclera and glaucoma mouse sclera to determine how the collagen material properties and morphology was altered by glaucoma . A parameter study was conducted to investigate the effects of structural and material property changes on the pressure-displacement response.

Chapter 5 summarizes the key findings and discusses future work beyond this thesis. The Appendix contains further details about the donors, experimental procedures, and additional figures.

Chapter 2

The contribution of glycosaminoglycans to the mechanical behavior of the posterior human sclera

This chapter characterizes the mechanical and structural changes of the human posterior sclera after experimental digestion of GAGs. Mechanical testing was done by pressure-controlled inflation using 3-dimensional digital image correlation (3D-DIC), and thickness was measured using an ultrasound transducer. Scleral specimen were incubated in a buffer solution to restore hydration, underwent inflation testing, treated in a solution to enzymatically digest the GAGs, then underwent inflation testing again. The experimental procedures for this chapter were adapted from a similar earlier study done on porcine sclera by Barbara J. Murienne. However, the equipment setup and data analysis methods were improved to capture the smaller displacements of the human sclera compared to the pig sclera. This chapter has been reprinted from *Journal of the Royal Society Interface* under the title "The contribution of glycosaminoglycans to the mechanical behavior of the posterior human sclera", with Barbara J. Murienne, Michelle L. Chen, Harry A. Quigley and Thao D. Nguyen as authors [106].

2.1 Introduction

The mechanical behavior of the sclera has been shown to play an important role in the initiation and development of ocular diseases such as glaucoma and myopia in both experimental and modeling analyses. Glaucoma is the second leading cause of blindness worldwide [142] and is characterized by the dysfunction [126, 99] and loss [57, 132] of the axons of the retinal ganglion cells (RGCs) at the optic nerve head (ONH) [127]. Intraocular pressure (IOP) can produce a high level of stresses and strains in the tissues of the ONH, depending on the mechanical properties of the sclera. This mechanical insult can potentially cause direct damage to the RGC axons, and/or lead to poor vascular nutrition and the activation of astrocytes. These events can occur at any level of IOP, whether higher or lower than that found in non-glaucoma eyes [50, 19, 11, 153]. Myopia is a common refractive error often characterized by the axial elongation of the eye wall [3]. Patients with high myopia are at increased risk for several blinding diseases, such as macular degeneration [23] and glaucoma [90]. Elongation of the sclera occurs by remodelling of the extracellular matrix structure and is accompanied by significant changes in the mechanical properties of the sclera.

The tensile and viscoelastic behavior of the posterior sclera is altered in glaucoma and myopia. The peripapillary sclera of human glaucomatous eyes has a lower creep rate and higher stiffness compared to that of normal eyes [36]. In a monkey model of glaucoma, the posterior sclera also exhibits a higher stiffness [62] and the peripapillary sclera shows a higher equilibrium modulus after stress relaxation following a rapid deformation, but no change in the time-dependent parameters compared to that of normal eyes [44]. The posterior sclera of human myopic eyes reaches a higher strain at maximum pressure than that of normal eyes [4]. In a tree shrew model of myopia, the posterior sclera also shows a greater strain at the peak pressure [117, 118], as well as a higher creep rate [152, 118], but a similar high-pressure elastic modulus [117, 152] than those of normal eyes.

Collagen represents 80% of the dry weight of the sclera [8], whereas elastin fibers and proteoglycan (PG) core proteins represent 2% of its dry weight [138, 6]. In comparison, GAGs represent only 0.5 to 1% of the scleral dry weight [17]. The changes in the mechanical properties of the posterior sclera are associated with specific changes in the collagen and elastin structure in glaucoma [131, 119, 31, 130] and myopia [41, 112, 95]. In addition, alterations in the s-GAG content have also been reported in glaucoma and myopia. In the human glaucomatous eyes, the s-GAG content is higher in the anterior sclera, trabecular meshwork and LC compared to that in normal eyes [83], but there are currently no data for the posterior sclera. In a tree-shrew model of myopia, the s-GAG content is lower than that of the contralateral control eyes in the posterior sclera [112].

GAGs are assemblies of disaccharide units into chains of various lengths, most of them attached to a core protein to form PGs. The most abundant GAGs in the posterior sclera are chondroitin sulfates and dermatan sulfates [165, 137]. GAGs attract and retain water through their negative ionic charges [12, 164], as well as their osmotic pressure [29, 46, 149]. They also directly interact with collagen fibrils [114, 122, 69, 139] through electrostatic interactions [92, 114] and have been hypothesized to regulate collagen fibril spacing through hydration (swelling) [93, 149, 75], GAG-GAG charge repulsion [15] and GAG-GAG antiparallel interactions [148].

We recently studied the effect of s-GAG removal on the mechanical behavior of the porcine posterior sclera [104]. The degradation of s-GAGs with ChABC from a hydrated state induced significant decreases in the scleral stiffness at low pressure, in the hysteresis and in the creep rate, while causing an increase in the stiffness at high pressure and strain at the onset of strain stiffening (i.e. length of the toe region). Those changes were found to be opposite to the changes observed from an increase in hydration from a baseline to a hydrated state. In addition, differences in the inflation response between the meridional and

circumferential directions were significantly reduced after enzymatic s-GAG degradation. These changes in both the tensile and viscoelastic behaviors showed that s-GAGs play an important role in the mechanical behavior of the posterior sclera. Specifically, the observed findings were interpreted to exceed the effects of hydration alone and suggested an interactive effect on the collagen fibrils.

In this study, we performed inflation testing of the human posterior sclera after incubation in buffer alone and after treatment in buffer containing ChABC to degrade the s-GAGs. We compared the inflation behavior for each specimen before and after treatment with ChABC. The results were used to evaluate whether s-GAG degradation induced changes in the mechanical response of the posterior human sclera and whether the changes in humans were comparable to those in a prior study on pigs. The findings were interpreted for their significance to the mechanical and pathological contribution of s-GAGs to the scleral mechanical behavior in glaucoma and myopia.

2.2 Methods

2.2.1 Specimens and glycosaminoglycan degradation

Eleven human donor eyes were obtained from the National Disease Research Interchange (NDRI) from 6 donors with an average age of 74.0 ± 9 years, whose medical records show no history of glaucoma (Table 2.1). All structural and mechanical outcomes were measured in the 4 anatomical quadrants of the posterior scleral shell (superior-nasal (SN), superior-temporal (ST), inferior-nasal (IN), inferior-temporal (IT)), outside the peripapillary region. To confirm the effectiveness of our s-GAG degradation protocol, we first determined the s-GAG content, in μg per mg wet tissue weight, of 2 samples taken in each of the 4 quadrants of a single eye. Both samples from each quadrant were divided into 2 experimental groups (Fig. 2.2). In the first group, the specimens were incubated for 18 h at 37 °C in a modified

	Number of specimens
s-GAG quantification	n=1*/1
Hydration	n=1*/1
Mechanical testing	n=9#/5
Thickness measurement	n=9#/5

Table 2.1: Number of specimens used for s-GAG quantification, hydration measurement, mechanical testing and thickness measurements. 1/1 indicates that 1 eye was used from 1 donor, 9/5 indicates that 9 eyes were used from 5 donors, * denotes that both eyes were from the same pair and # denotes that the same eyes were used for both experiments.

Trizma buffer at pH 8.0 (buffer-treated). In the second group, the specimens were incubated for 18 h at 37 °C in Trizma buffer containing ChABC (C2905, SigmaAldrich, St. Louis MO) at 2 units/ml (enzyme-treated). ChABC is known to degrade chondroitin and dermatan sulfates at pH 8.0. We then inferred the s-GAG content in μg per mg dry tissue weight from hydration measurements on 2 samples taken in each quadrant of the contralateral eye, and each one incubated in either buffer alone or buffer containing ChABC (Fig. 2.2). The remaining 9 eyes were inflation tested after incubation for 18 h in buffer alone (buffer-treated) followed by incubation for 18 h in the enzyme solution (enzyme-treated). Scleral thicknesses were measured at the end of each inflation test. We confirm that our research followed the tenets of the Declaration of Helsinki.

2.2.2 Specimen preparation

The eyes were received in a closed container, on a gauze pad soaked with saline solution to reduce dehydration, and used within 48 h *post-mortem*. The extraocular fat and muscles were removed, leaving a clean scleral surface. For 2 eyes, we used a 8 mm biopsy punch to excise samples from each quadrant for s-GAG quantification and hydration measurements (Fig. 2.2). The samples were punched 2 mm away from the ONH and away from visible arteries and veins. Two 3x3 mm square samples were then cut from each disc, from which we gently removed the retina and choroid (Fig. 2.2).

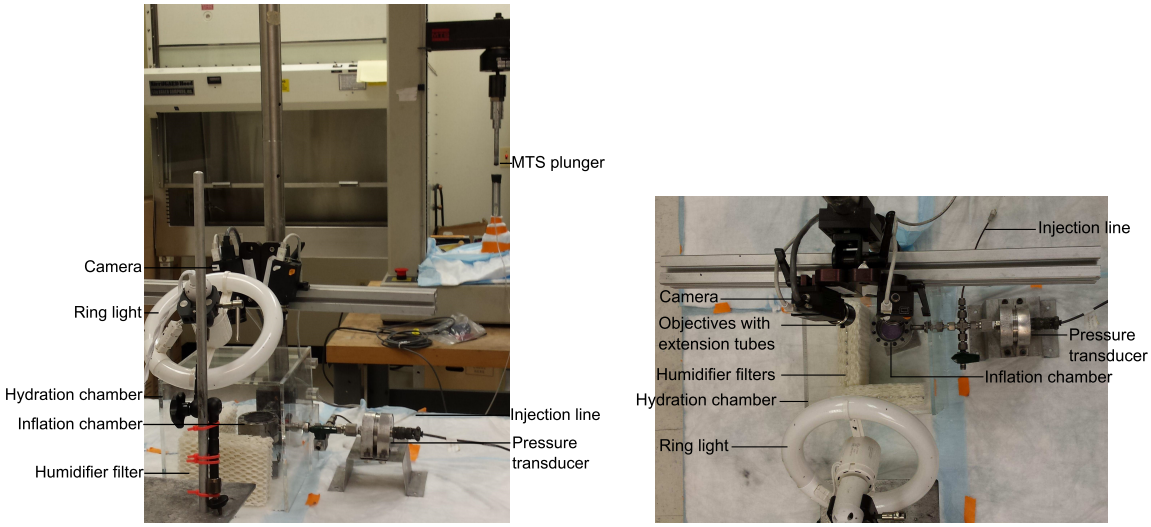

(a) (b)

Figure 2.1: (a) Side view and (b) top view of the experimental setup showing the inflation chamber, pressure transducer, MTS, hydration chamber, as well as the imaging and lighting systems.

The eyes used for mechanical testing and thickness measurements were glued to a custom-made acrylic holder centered about the ONH using cyanoacrylate (Permabond 910, Electron Microscopy Sciences, Hatfield PA) (Fig. 2.3(a)). The anterior sclera was cut away and the intraocular structures, including the retina and choroid, were removed from the remaining posterior scleral shell.

2.2.3 Glycosaminoglycan quantification

The protocol for s-GAG content quantification was previously described [104]. Briefly, the s-GAG content was assessed on 3x3 mm samples, taken in each of the 4 quadrants of a single eye (Fig. 2.2) and subjected to either buffer treatment or enzyme treatment, using the Blyscan assay (Accurate Chemical & Scientific Corporation, Westbury NY). The samples were first blotted dry on Whatman paper for 1 min, weighed wet and incubated in a solution of Papain (P3125, SigmaAldrich, St. Louis MO) for 18 h at 60 °C, following Boubriak et al. protocol [16]. The s-GAG content per dry tissue weight in each quadrant was inferred

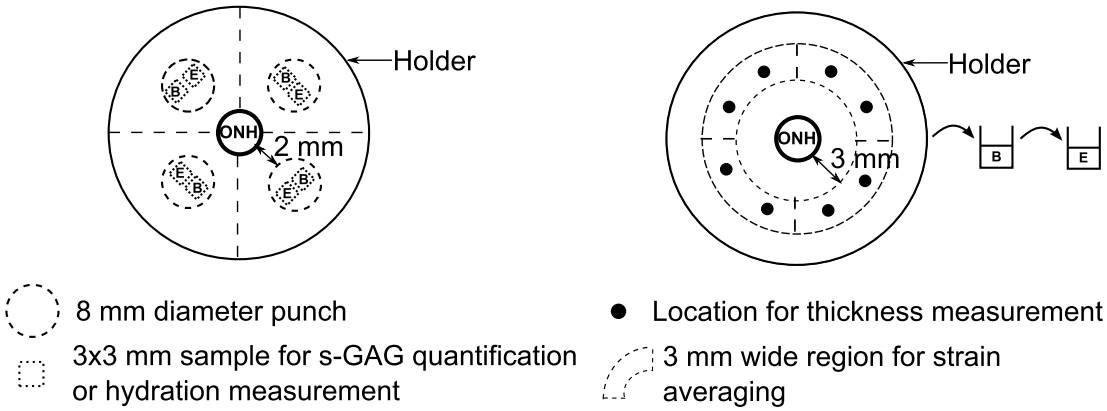

Figure 2.2: Schematic of the human posterior sclera protruding from the holder showing the ONH as well as the locations of the samples used for the s-GAG quantification and hydration, the locations of the thickness measurements, and the regions where the strains were averaged. The letter B indicates the samples incubated in buffer alone, while the letter E indicates samples treated with the enzyme. For the s-GAG quantification and hydration measurement, samples from the same eye were subjected to each condition, while for the mechanical testing the specimens were subsequently treated with the buffer alone and then with the enzyme solution.

using hydration measurements of the wet over dry sample weight ratio. The wet sample weight was measured after blotting the samples dry on Whatman paper for 1 min using a precision balance (XP26DR, Mettler-Toledo LLC, Columbus OH). The wet samples were weighed inside pre-weighed eppendorf tubes to prevent further evaporation. The samples were then dehydrated by incubation for 48 hours in an oven at 60 °C and weighed in the same manner.

2.2.4 Mechanical testing

For inflation testing, the specimens that were glued to the custom plastic holder were then clamped to a custom inflation chamber (Fig. 2.1(a) and (b)). Dulbecco's phosphate-buffered saline (DPBS) was injected into the chamber using an MTS-actuated syringe (MTS, Eden Prairie MN) (Fig. 2.1(a)). The pressure inside the chamber was monitored using a pressure transducer (TJE, 2 psig range, Honeywell, Morristown NJ) and fed back into the MTS

testing machine to control the motion of the MTS crosshead (MTS, Eden Prairie MN) using a PID controller (Fig. 2.1(a) and (b)). The specimens were first equilibrated at the baseline pressure 0.21 kPa for 30 min, then subjected to a load-unload cycle from baseline pressure to 6 kPa at 0.13 kPa/s, followed by a 30 min recovery period at baseline pressure. The baseline pressure was then maintained for the thickness measurements. The inflation chamber was enclosed in a clear perspex humidity chamber with 90% humidity to prevent dehydration of the specimens during testing (Fig. 2.1(a) and (b)).

2.2.5 Thickness measurement

The scleral thickness was measured at 8 locations, 2 in each of the 4 quadrants of the eyes (Fig. 2.2) using an 15 MHz ultrasound transducer (V26045, Olympus NDT Inc., Waltham MA) fitted with 1.5 mm diameter Sonopen tip (DLP-302, Olympus NDT Inc., Waltham MA), as described in a previous work [104]. The ultrasound transducer was linked to a pulser-receiver (5073PR-15-U, Olympus NDT Inc., Waltham MA) and the echoes from the outer and inner scleral surfaces were recorded from an oscilloscope (TDS220, Tektronix Inc., Beaverton OR). The scleral thickness T was calculated as:

$$T = \frac{1}{2} c_{sclera} \Delta t \tag{2.1}$$

where c_{sclera} =1597 m/s [61] is the speed of sound in the sclera and Δt is the time difference between the peaks of the outer and inner sclera echoes. The thickness in each quadrant was reported as the average of both measurements.

2.2.6 Digital Image Correlation

The posterior sclera was speckled with black India ink (Fig. 2.3(a)) using an airbrush (ECL4500 HP-CS, Iwata Medea Inc., Portland OR) prior to mechanical testing to enhance the contrast for the 3D surface displacement measurements using 3D-DIC. Images were ac-

quired using a stereoscopic system equipped with 2 monochrome cameras with a 2 Mpixel resolution (GRAS-20S4M-C, Point Grey, Richmond BC, Canada), 26° stereo angle, and objectives with a 35 mm focal length (Xenoplan 1.9/35mm-0901, Schneider Optics, Hauppauge NY) fitted with 5 mm long extension tubes (54-628, Edmund Optics, Barrington NJ). Illumination was provided by circline light bulb (90922L, Commercial Electric, Cleveland OH) to increase image contrast and maintain even lighting across the specimen. Images with a 0.018 mm/pixel resolution were captured every 2 seconds during mechanical testing with Vic-Snap 2009 (Correlated Solutions Inc., Columbia SC) and imported into Vic3D 2012 (Correlated Solutions Inc., Columbia SC) for 3D-DIC analysis. The 3D-DIC correlation was performed using a 33 pixels correlation window and 5 pixels step size.

2.2.7 Strain calculation

For each correlated point at every pressure increment, 3D-DIC provided the 3D surface displacements (u_x, u_y, u_z), from the reference geometry at the baseline pressure, on a 2D Cartesian grid $(\mathbf{e}_x, \mathbf{e}_y)$ with a 0.090 mm resolution (Fig. 2.3(a)). However, given the geometry of the sclera, strains were calculated along circumferential and meridional directions, $\mathbf{e}_\theta$ and $\mathbf{e}_\phi$, respectively (Fig. 2.3(a) and (b)). To define the new circumferential-meridional coordinate system, we identified the center of the ONH base as the pole. The separation of the ONH region from the scleral region was found by an iterative least-squares fitting process. A sphere was fit to the reference position of the posterior scleral shell, and the points with 3% error from the spherical fit radius were removed until the fitting error converged. These corresponded to the ONH. Then, another sphere was fit to remaining points to obtain a more accurate description of the posterior scleral shell over which the strains were calculated. An oblique cylinder was then fitted to the ONH region, and the center of the bottom face was defined as the ONH center (Fig. 2.3 (b)).

Surface strains were calculated over triangular domains formed by 3 nearest neighbor

points with average grid spacing of 0.10 mm, as described in Genovese et al. [59]. Triangular domains were constructed using the Delaunay triangulation algorithm in MATLAB, and were sufficiently small to be assumed planar. The meridional direction $\mathbf{e}_\phi$ was defined for each triangle by projecting the vector $\mathbf{v}^{MN}$ connecting the triangle centroid M to the ONH center N onto the plane of the triangular domain. The circumferential direction $\mathbf{e}_\theta$ was calculated as the cross product between the meridional direction and the outward unit normal of the triangular plane $\mathbf{e}_n$ (Fig. 2.3 (b)).

The unit orientation vectors ($\mathbf{n}^{AB}$, $\mathbf{n}^{BC}$, $\mathbf{n}^{CA}$) were calculated for the sides of the triangle using the reference positions and transformed to the spherical coordinate system. The stretch sides of the triangular domain (λ^{AB}, λ^{BC}, λ^{CA}) were calculated using the reference positions and displacement vectors. They were used to calculate the components of the right Cauchy-Green stretch tensor $C_{\theta\theta}$, $C_{\phi\phi}$ and $C_{\theta\phi}$ using the following system of equations:

$$\begin{cases} \left(\lambda^{AB}\right)^2 = \mathbf{n}^{AB} \cdot \mathbf{C}\mathbf{n}^{AB} \\ \left(\lambda^{BC}\right)^2 = \mathbf{n}^{BC} \cdot \mathbf{C}\mathbf{n}^{BC} \\ \left(\lambda^{CA}\right)^2 = \mathbf{n}^{CA} \cdot \mathbf{C}\mathbf{n}^{CA} \end{cases} \tag{2.2}$$

The Green-Lagrange strains in the circumferential and meridional directions were evaluated as, $E_{\theta\theta} = 0.5(C_{\theta\theta} - 1)$, $E_{\phi\phi} = 0.5(C_{\phi\phi} - 1)$. The shear strain was $E_{\theta\phi} = 0.5(C_{\theta\phi})$. The strain components were reported for each quadrant as an average over a 3 mm region in the meridional direction, spanning the entire quadrant and located 3 mm away from the ONH.

2.2.8 Hoop stress calculation

The hoop stresses $\sigma_{\theta\theta}$ in the circumferential direction and $\sigma_{\phi\phi}$ in the meridional direction were reported at each pressure level for each quadrant as:

$$\sigma_{\theta\theta} = \sigma_{\phi\phi} = \frac{Pr}{2T} \tag{2.3}$$

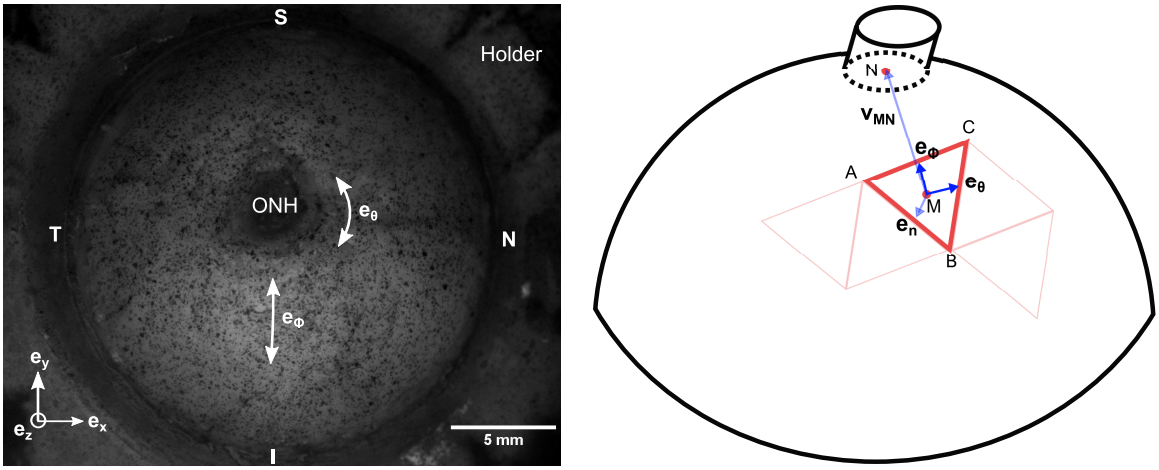

(a) (b)

Figure 2.3: (a) Image of a left human scleral shell mounted on a holder and speckled for 3D-DIC tracking, showing the eye anatomical quadrants and directions. (b) Schematic showing how the local basis was defined for each Delaunay triangle. For each triangle, the vector $\mathbf{v}_{MN}$ was defined from the centroid of the triangle M to the center of the ONH base N. This vector was then projected onto the plane of the triangle and normalized to find the meridional direction $\mathbf{e}_\phi$. The circumferential direction $\mathbf{e}_\theta$ was defined as the cross product $\mathbf{e}_\phi \times \mathbf{e}_n$, where $\mathbf{e}_n$ is the outward normal unit vector to the plane of the triangle.

where P is the pressure, r is the radius of the shell obtained by fitting a sphere to the 3D-DIC reference position data and T is the scleral thickness in a particular quadrant, averaged over 2 measurements. All 3 parameters were specific to the specimen treatment state.

2.2.9 Mechanical data analysis

Four mechanical outcomes were extracted from the stress-strain curves for each scleral shell, quadrant and experimental condition: buffer-treated and enzyme-treated. The low-pressure stiffness was defined as the slope at low pressure calculated by fitting the data points of the loading curves that were within the first 25% of the strain at maximum pressure. The high-pressure stiffness was defined as the slope at high pressure calculated from the fit of the last 30% of the data points of the loading curves. The hysteresis was defined as the area between the loading and unloading curves, calculated by numerical integration using a trapezoidal

rule. Outliers were treated using the MATLAB function *smooth* with the *rlowess* and *rloess* methods for the loading and unloading curves, respectively. The function *rlowess* performs a local linear interpolation, while *rloess* applies a second-order polynomial local interpolation. Different smoothing methods were used because the loading stress-strain curves for all the specimen were nearly linear, while the unloading curves were significantly more nonlinear (Figs. 2.4 and 2.5). Since the loading curves were linear and did not show a clear transition between the toe and linear regions, the strain at maximum pressure rather than the strain at the onset of strain stiffening was extracted as a measure of the tissue extensibility at the maximum pressure.

2.2.10 Statistical analysis

To evaluate the effect of treatment with the enzyme from a buffer-treated state on the mechanical outcomes and thickness data, we used a repeated measures ANOVA implemented with the MATLAB function *ravova*, using the data for all eyes and quadrants. Repeated measures ANOVA not only indicated whether the mechanical outcomes were different between the experimental groups or between the quadrants, but it also indicated if there was an interaction between group and quadrant. Similarly, we used repeated measures ANOVA to evaluate the difference in mechanical outcomes between the circumferential and meridional directions in both the buffer-treated and enzyme-treated groups.

2.3 Results

2.3.1 Glycosaminoglycan degradation

The s-GAG content in all 4 quadrants of a single eye for samples subjected to either buffer treatment or enzyme treatment are shown in Table 2.2. The decrease in s-GAG content after treatment with the enzyme was >98% in all quadrants. No statistics were performed

	ST	SN	IT	IN
Buffer-treated	5.29	5.87	6.47	3.22
Enzyme-treated	0.074	0.066	0.026	0.022

Table 2.2: s-GAG content [μg/mg dry tissue weight] in each quadrant of a single eye, for samples in the buffer-treated and enzyme-treated groups. No statistical analysis.

	Buffer-treated	Enzyme-treated	p-value
Thickness	0.92 $\pm$ 0.26	0.80 $\pm$ 0.18	$<$0.001

Table 2.3: Thickness [mm] averaged over all specimens and quadrants in the buffer-treated and enzyme-treated groups. Repeated measures ANOVA used for the statistical analysis.

as a single specimen was studied only to confirm the s-GAG degradation protocol previously developed for pig scleras [104] was as effective in humans.

2.3.2 Thickness data

The thickness averaged over all eyes and quadrants after treatment with buffer alone and after treatment with enzyme are presented in Table 2.3. The average thickness from the buffer-treated state decreased by 13.3% with enzyme treatment ($p<0.001$). There was no interaction between experimental group and quadrant. We did not detect significant spatial differences in the thickness measurements.

2.3.3 Mechanical behavior

Comparing the buffer-treated and enzyme-treated groups

We first compared the mechanical outcomes averaged over the 4 quadrants and specimens after buffer treatment and after enzyme treatment (Table 2.4). In the circumferential direction, treatment with the enzyme from a buffer-treated state increased the low-pressure stiffness by 30.3% ($p<0.005$), high-pressure stiffness by 11.0% ($p<0.05$) and hysteresis by 41.6% ($p<0.001$). In the meridional direction, the low-pressure stiffness increased by 24.2% ($p<0.05$), the high-pressure stiffness by 11.4% ($p<0.05$) and the hysteresis by 16.5% ($p=0.28$)

after enzyme treatment. Treatment with the enzyme had no statistically significant effect on the strain at maximum pressure. There was no interaction between experimental group and quadrant for any of the mechanical outcomes. In addition, we did not detect significant spatial differences in any of the mechanical outcomes measured.

	Circumferential			Meridional		
	Buffer-treated	Enzyme-treated	p-value	Buffer-treated	Enzyme-treated	p-value
Low-pressure stiffness [kPa]	7331.1 ± 3478.8	9552.2 ± 5345.2	<0.005	4641.1 ± 3376.0	5763.0 ± 2828.9	<0.05
High-pressure stiffness [kPa]	15544.2 ± 6172.2	17254.4 ± 5510.9	<0.05	6819.4 ± 4031.7	7599.1 ± 4739.9	<0.05
Hysteresis [kPa]	0.030 ± 0.016	0.043 ± 0.019	<0.001	0.120 ± 0.129	0.140 ± 0.088	0.28
Strain at max pressure [mm/mm]	0.0038 ± 9.77e-4	0.0038 ± 8.96e-4	1.0	0.010 ± 0.0046	0.0090 ± 0.0032	0.10

Table 2.4: Comparison of the mechanical outcomes, averaged over all quadrants, between the buffer-treated and enzyme-treated groups, in the circumferential and meridional directions. Repeated measures ANOVA used for the statistical analysis.

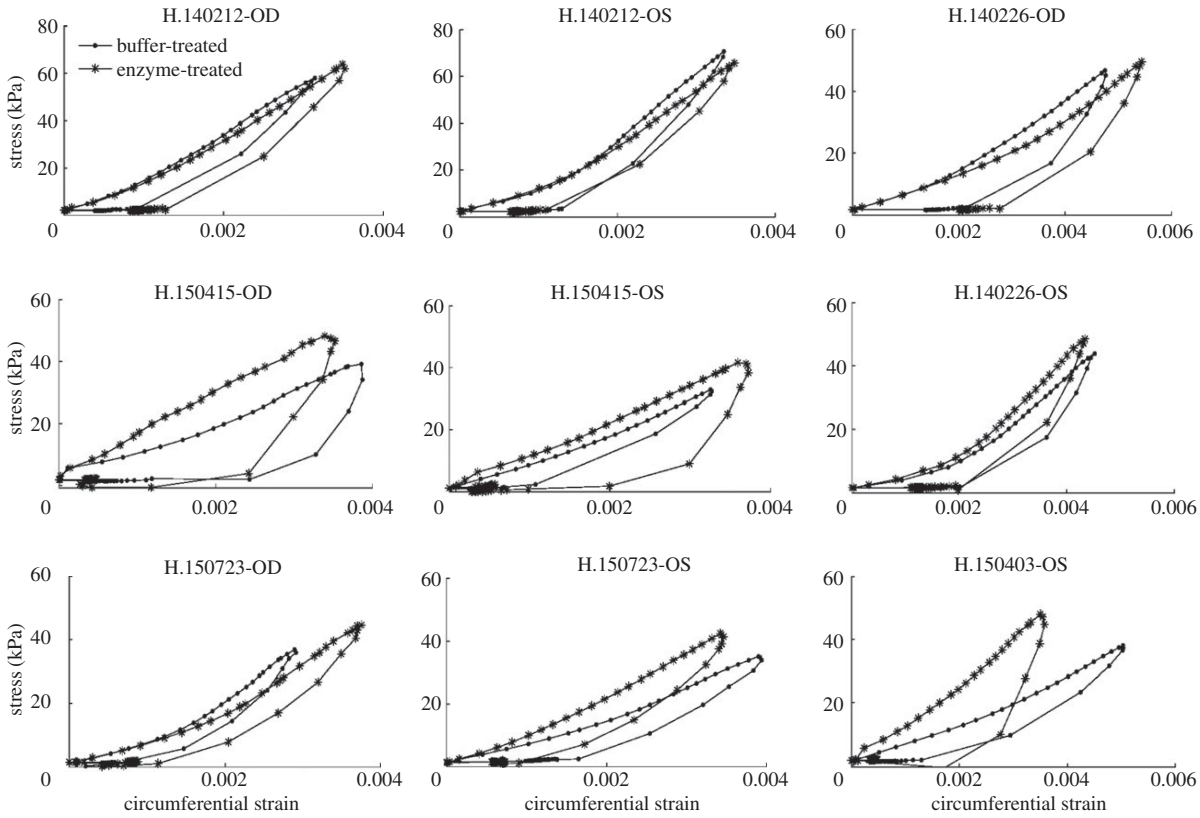

Figure 2.4: Stress-strain curves in the circumferential direction for all human specimens, averaged over the 4 anatomical quadrants, after buffer-treatment and after enzyme-treatment. The outliers were locally treated with the MATLAB function *smooth*.

Comparing the circumferential and meridional directions

We also compared the difference between the mechanical outcomes in the circumferential and meridional directions, averaged over all specimens and quadrants, after incubation in buffer alone and after incubation with the enzyme. In both the buffer-treated and enzyme-treated groups, the high-pressure stiffness, hysteresis and strain at maximum pressure were significantly different in the circumferential and meridional directions ($p<0.001$ for all mechanical outcomes and experimental groups). In the buffer-treated group, the circumferential low-pressure stiffness was 58.0% higher and its high-pressure stiffness was 127.9% larger than meridionally. Furthermore, the circumferential strain at maximum pressure was 62.1%

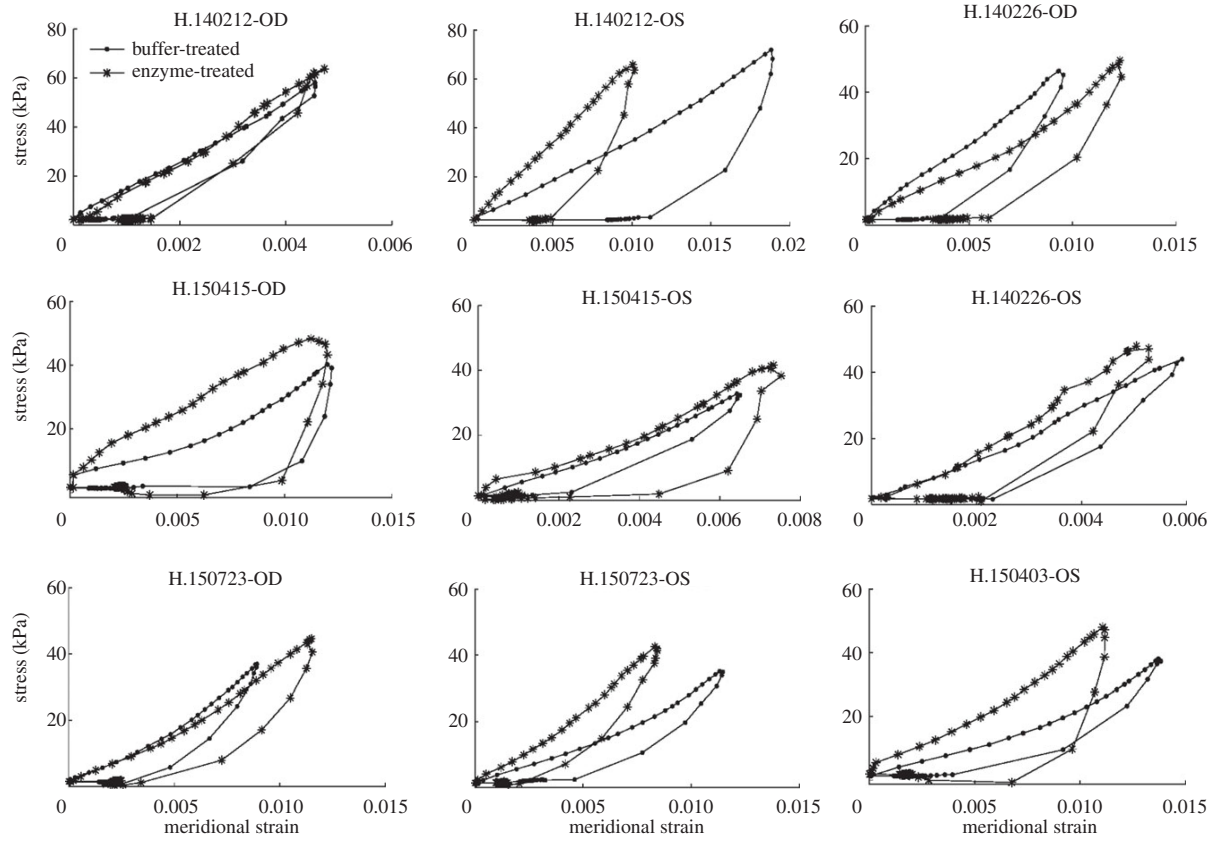

Figure 2.5: Stress-strain curves in the meridional direction for all human specimens, averaged over the 4 anatomical quadrants, after buffer-treatment and after enzyme-treatment. The outliers were locally treated with the MATLAB function *smooth*.

smaller and its hysteresis was 74.7% lower than meridionally. These findings were similar in the enzyme-treated group, with the circumferential low-pressure stiffness 65.8% higher, high-pressure stiffness 127.1% larger, strain at maximum pressure 57.6% smaller, and hysteresis 69.3% lower than in the meridional direction.

2.4 Discussion

To understand better the role of s-GAGs in the tensile properties of the posterior human sclera, we compared its thickness and mechanical behavior under inflation after buffer hydration with a s-GAG depleted state after treatment with ChABC. This comparison provided

a better understanding of the role of the s-GAGs in the tensile properties of the human posterior sclera.

The s-GAG content of the hydrated sclera reported here is similar to that previously reported in human eyes [16] and to our results in the porcine sclera [104]. The s-GAG content was also consistent between pig and human in Schultz et al. [147]. The degradation procedure used here removed nearly all s-GAGs in human eyes as it had in the porcine sclera. The minimal remaining s-GAGs quantified after enzyme treatment could represent: 1) s-GAGs that are not sensitive to ChABC, such as keratan sulfates, 2) incompletely degraded, but normally sensitive s-GAGs to ChABC, or 3) incompletely removed but degraded s-GAGs.

s-GAG removal caused a significant increase in the low-pressure stiffness, high-pressure stiffness and hysteresis, but did not affect the strain at maximum pressure. The combined effect was a significantly stiffer response, though the effect was modest. The increase in the low-pressure stiffness could be due to collagen fibril fusion, as decribed by Quacci et al. for the glycanolytic digestion of bovine cartilage [123], or to a decreased tissue hydration. It could also explain the non-significant change in the strain at maximum pressure, compared to the increased peak-pressure strain observed in the porcine sclera [104]. The increase in the high-pressure stiffness could be due to the lower tissue hydration or the increased free versus bound water, due to the loss of s-GAGs which regulate the water retention capacity of the tissue [12], that would increase the friction between the collagen fibrils. It may also arise from the fusion of the collagen fibrils. The reason why both the high-pressure stiffness and hysteresis increase remains unclear and more study of the structural role of GAG-collagen interaction in the sclera is needed. In addition, the mechanical behavior of the circumferential and meridional directions did not significantly change compared to each other after enzyme treatment, suggesting that removal of the s-GAGs did not affect the anisotropy of the collagen fibril arrangement or the anisotropy of their connection, as hypothesized in the porcine sclera

[104], probably due to the abundance of the non-enzymatic collagen crosslinks.

s-GAGs therefore contribute significantly to the mechanical properties of the human posterior sclera through their effects on hydration and collagen-collagen interaction. The results presented here are not consistent with the increase in tissue extensibility [4, 117, 118] and creep rate [152, 118] observed in myopia. On the contrary, they are in the same direction as the increase in stiffness [62, 36] and decrease in creep rate [36] observed in glaucoma. *In-vivo* collagen crosslinking of the posterior sclera in a mouse model of glaucoma using glyceraldehyde was shown to increase damage to the RGCs [82], suggesting that an increased stiffness is a detrimental effect in the glaucoma eye. However, scleral stiffening might be beneficial for myopia, as suggested by the blockage of the eye elongation in a guinea pig model of myopia following the *in-vivo* injection of genipin [168].

The posterior human sclera was significantly stiffer than the porcine sclera [104], which agreed with uniaxial strip tests [147] and is consistent with the higher number of non-enzymatic collagen crosslinks [147]. The hysteresis was larger in the posterior human scleras than that reported for the porcine scleras [104]. The overall effect of s-GAG degradation was to make the inflation response slightly stiffer in humans, whereas the same treatment dramatically reduced the stiffness of the porcine sclera. Differences in the scleral collagen crosslink structure, and s-GAG content and types, might contribute to the differences in the s-GAG degradation effects observed between humans and pigs.

Interestingly, we found that scleral thickness significantly decreased after enzyme treatment in human eyes, whereas it increased in pig eyes [104]. The human scleral thicknesses in this investigation were comparable to those reported in other studies [111, 167]. The decrease in thickness could result from a loss of water with s-GAGs degradation, since s-GAGs attract and can bind water. The difference between human and pig sclera in thickness could result from several features of the scleral content. The specific s-GAG composition of

both species might differ in several respects. The amount and type of negative ionic charges determine scleral capacity for water absorption [12], which is also limited by the collagen interfibrillar spacing, itself governed by GAG-GAG charge repulsion [15] and GAG-GAG anti-parallel interactions [148]. Enzymatic digestion of chondroitin sulfates was shown to reduce swelling in the cornea [70] and to reduce the "re-expansion" capability of collagen fibrils in dentin upon rehydration [116]. Compared to the pig, the human sclera has 53% less collagen per dry tissue weight but its collagen has 1.6 times more non-enzymatic "glycation-type" crosslinks [147]. This was likely because of the older age of human donors compared to the pigs. A higher collagen crosslink density could lead to a stiffer extracellular matrix and reduced collagen interfibrillar spacing, which in turn would increase the resistance to swelling. Experiments have shown that treating the human posterior sclera with glutaraldehyde, a collagen crosslinking agent, significantly reduces hydration and possibly reduces the collagen intrafibrillar spacing [16]. In human corneal stroma, the increase in non-enzymatic crosslinks with age also correlated with a decrease in the collagen interfibrillar spacing [89]. However, no significant decrease in hydration was detected in the human posterior sclera after s-GAG removal with ChABC compared to hydrated scleras by others [16], suggesting a possible microstructural rearrangement. The removal of s-GAG leads to the fusion and thinning of collagen fibrils in cartilage [123] and in decorin and biglycan deficient mice [42, 33], which can also lead to a smaller tissue thickness without a decrease in hydration. Taken together, these findings suggest that a tissue rearrangement rather than a decreased hydration may underlie the scleral thinning we observed.

There were several limitations of this study. Mechanical testing and hydration measurement after treatment could not be performed in the same eyes. In addition, we were testing eyes *post-mortem*. They were received at various times after death and, while in humidified jars, their hydration state surely varied. We chose to test them after re-hydration and cannot

know their true hydration *in-vivo*. Finally, the small strains that we identified would only have found large regional differences.

2.5 Conclusion

In conclusion, nearly complete s-GAG digestion of the human posterior sclera decreased its thickness and led to a small, significant increase in the overall stiffness and hysteresis of the scleral inflation response. While others have reported minimal effects of GAGs on the tensile or viscoelastic mechanical behavior of connective tissue, we found that s-GAGs play a measurable role in the mechanical behavior of the posterior human sclera.

Chapter 3

Increased Stiffness of Collagen Fibrils following Cyclic Tensile Loading

This chapter investigates the changes in collagen fibril properties following cyclic loading. A previous experimental study demonstrated that cyclic loading of acellular collagen constructs caused significant stiffening and strengthening. An anisotropic hyperelastic model of the collagen constructs was developed to determine whether the measured changes in the tissue-level properties can be attributed to changes in the anisotropic collagen structure or mechanical properties of the collagen fibrils. The model was fit to the stress-stretch response measured for the constructs subjected to different preconditioning strains and cycles. This chapter has been reprinted from the *Journal of the Mechanical Behavior of Biomedical Materials* under the title "Increased stiffness of collagen fibrils following cyclic tensile loading", with Michelle L. Chen, Jeffrey W. Ruberti and Thao D. Nguyen as authors [26].

3.1 Introduction

Collagen is the main contributor to the stiffness and strength of soft connective tissues, such as the cornea, tendon, and blood vessels. The collagen of soft tissues exhibit a highly organized hierarchical structure, in which molecules are assembled into fibrils, then into fibers or lamellar microstructures, and finally into larger scale anisotropic tissue-level structures.

Numerous studies have shown that the anisotropic collagen structure, fibril morphology, and mechanical properties can be altered by mechanical loading through fibril reorientation and damage mechanisms, typically associated with preconditioning [163, 157], and through remodeling mechanisms attributed to cellular activity. Changes in the mechanical loading and mechanical properties of the extracellular environment can induce a complex chain of cellular signaling events that results in the degradation and synthesize of extracellular matrix (ECM) proteins, including collagen. Miller et al. [98] found that strenuous exercise such as kicking, elevated the synthesis rates of tendon collagen, muscle collagen, as well as myofibrillar and sarcoplasmic protein, peaking at 24 hours after exercise. In another study by Wong et al. [172], cyclic tension of chondrocyte-seeded alginate constructs upregulated the expression of collagen and matrix metalloproteinases (MMPs). Collagen deposits were found to be the greatest in areas of largest stress produced by human dermal fibroblasts cast in fibrin gels undergoing biaxial stretch [146]. Cells have also been shown to affect collagen fiber morphology. Foolen et al. [53] reported that culturing compressed, buckled strips of the periosteum of chick embryos a caused leftward shift of the transition strain of the stiffening stress-strain curve to the applied compressive strain. This was caused by a remodeling of collagen fiber crimp driven by cell contraction.

Recent studies have shown that the collagen structure and mechanical properties can be altered also in acellular tissue constructs through passive chemomechanical mechanisms. Zhang and Sacks [176] showed that in exogenously crosslinked collagen bioprosthetic tissues, long term cyclic loading can alter the reference configuration and anisotropic wavy collagen structure through the breaking and reformation of collagen crosslinks in the loaded state, leading to a leftward shift in the stress response and a stiffer stress response. Flynn et al. [51] showed that the anisotropic structure of collagen networks can be altered by stretch-mediated enzymatic degradation of collagen fibrils (see also [74, 13, 175]). Mechanical stretch can slow

and, beyond a threshold, halt enzymatic degradation of collagen fibrils [52]. Thus, fibrils aligned with the loading axis were protected from degradation, while those oriented away from the loading axis were degraded [161]. Susilo et al. [156] preconditioned acellularized collagen tissue constructs at different strains levels using different number of cycles, then subjected the preconditioned tissues to uniaxial tension to failure to measure the effect of cyclic loading on the mechanical properties of the constructs. The results showed that cyclic loading increased the stiffness and strength of the collagen constructs. A greater stiffening effect was measured for the larger applied strain amplitude. The stiffening effect occurred as an increase in the slope of the linear portion of the strain-stiffening stress response and was accompanied by an increase in the reference length of the specimen. The permanent elongation of the specimen can be explained by the breaking of crosslinks and the reorientation of fibrils along the loading direction and is commonly observed in preconditioning studies [133, 157]. However the resulting rightward shift of the stress-strain curve is typically accompanied by a softening rather than stiffening of the stress-strain response. Moreover, Susilo et al. [156] did not measure statistically significant changes in collagen fibril area fraction or anisotropic structure with cyclic loading, both of which would have explained the significant increase in stiffness and strength.

In this study, we aimed to investigate the changes in fibril-level properties from the tissue-level properties measured by Susilo et al. [156] using a modeling approach. Specifically, we aimed to determine if the tissue-level changes can be attributed to alterations in the anisotropic structure or the mechanical properties of the collagen fibrils. The latter implies that cyclic mechanical loading can induce collagen stiffening through chemomechanical processes separate from those of cells. We developed a micromechanical model for the anisotropic hyperelastic behavior with damage of the collagen constructs. The collagen fibrils were described by wavy elastica fibers arranged in all orientations according a probability density

distribution of the orientations, obtained from experimental measurement using transmission electron microscopy (TEM). The model parameters for the effective fibril stiffness, crimp angle, slenderness ratio, threshold strain for damage initiation, and damage growth rates were fit to the experimentally measured uniaxial tension response. Statistical analyses were applied to analyze the effects of the number of cycles and strain amplitude on the properties of the collagen fibrils and whether alterations in the fibril properties with cyclic loading were more significant than the variations in the measured anisotropic structure.

3.2 Experimental methods

The following sections provide a brief summary of the mechanical testing, and imaging methods used in the experimental study of Susilo et al. [156].

3.2.1 Mechanical Testing

Dense, disorganized collagenous substrates (DDCS) were mounted between two spring-loaded grips, with the resulting force from the applied strain measured using a 500g load cell (Honeywell, Morristown, NJ). To precondition, the DDCS strips underwent displacement-controlled cyclic uniaxial tension to either 13% strain or 26.7% strain for either 1 cycle or 50 cycles, forming four experimental groups. The 13% strain magnitude corresponded to the linear region of the load-to-failure stress-stretch curve, and the 26.7% stain corresponded to the region of the stress-stretch curve where damage was observed to occur. Immediately after preconditioning, at least four specimens of each experimental group were loaded to failure. The resulting engineering stress P_{exp} was defined as the force fit to the average load to failure curve divided by the average initial cross-section area measured for all specimens within the group after preconditioning (Table 3.1). The remaining three specimens of each experimental group were removed from the test setup and prepared for TEM imaging as described in

Experiment Group	Area (mm^2)
1 cycle 13% strain	0.426
50 cycle 13% strain	0.408
1 cycle 26.7% strain	0.422
50 cycle 26.7% strain	0.359

Table 3.1: The average initial cross sectional area of samples tested to failure measured after preconditioning [156]. The areas for the 50 cycle groups were statistically significantly smaller than for the 1 cycle groups.

detail in the next section.

3.2.2 Fibril structure characterization

To characterize the fibril structure, TEM images of the *en face* DDCS sections were taken (JEOL JEM 1010 Electron Microscope, Peabody, MA). For each strip of DDCS used for TEM imaging, at least five images were taken per strip. Using the Fourier transform method detailed in Sander and Barocas [145], a normalized histogram of the fibril orientation θ, in the plane of the tissue, relative to the loading axis was created with a five degree angular resolution to form a probability density distribution $\rho(\theta)$ for each TEM image(Fig. B.1). The TEM images were also applied to measure the areal density of the collagen fibrils. The results showed that cyclic loading did not change the areal density of the collagen fibrils, thus this effect was not incorporated into the micromechanical model for the collagen substrates developed in the next section.

3.3 Modeling Methods

We developed a distributed fiber model to describe the anisotropic, nonlinear stress response of the DDCS up to the point of failure. The DDCS was assumed to be composed by a planar arrangement of wavy collagen fibrils within a compliant isotropic matrix. The arrangement of the fibrils were described by a probability distribution function of fibril orientation prescribed

by the normalized $\rho(\theta)$. The wavy fibrils respond to an applied force by first straightening, then stretching, and finally becoming damaged when the stretch exceeds a damage threshold. The following subsections describe the fibril-level kinematics, tissue-level stress response, and procedure for determining fibril material parameters.

3.3.1 Fibril-level model for the stress response and damage

For the collagen fibrils, we applied the wavy elastica model developed by Comninou and Yannas [28], which represents the fibrils as planar sinusoidal beams following the assumptions of the Reisnner beam theory [141] (Fig. 3.1). The midline of the undeformed fibril is given by $X_2 = a\sin(bX_1)$, where $(X_1,\ X_2)$ are the coordinates along the horizontal and vertical directions, $\Theta_0 = ab$, is the initial crimp angle, which is defined as the maximum angle that fibril makes with the horizontal axis, and $L = 2\pi/b$ is the length of the fibril projected onto the horizontal axis. The beam is assumed to be simply supported and subjected to a horizontal force F applied at $X_1 = L$. The applied force is described by the non-dimensionalized parameter $\alpha = F/EA$, where A is the cross-section area, E is the Young's modulus of the fibril, and EA describes the axial stiffness of the fibril. The bending stiffness of the fibril is described by $E\beta$, where $\beta = b^2r^2$ is the slenderness ratio, and r is the fibril radius.

For small crimp angles, the rotation angle of the midline, $\tan\Theta(X_1) = dX_2/dX_1$, can be approximated as $\Theta(X_1) = ab\cos(bX_1)$. Further assuming small microscopic fibril strain, an analytical solution can be obtained for both the deformed rotation angle, ϑ, and λ_f [28, 161]:

$$\vartheta(X_1) = \frac{\beta}{4\alpha(1+\alpha)+\beta}\Theta(X_1) \tag{3.1}$$

$$\lambda_f(X_1) = 1 + \alpha\cos(\vartheta(X_1)). \tag{3.2}$$

The microscopic fibril stretch λ_f signifies the axial stretch of the midline of the wavy fibril. We further define a macroscopic fibril stretch from the elongation of the wavy elastica along the horizontal direction: $\bar{\lambda} = x(L)/L$, where $x(L)$ signifies the position of the elastica at

the applied force (Fig. 3.1). Solving for $x(L)$ by integrating $\frac{dx}{dX_1} = \lambda_f \frac{\cos(\vartheta)}{\cos(\Theta)}$ gives,

$$\bar{\lambda} = \frac{1}{L}\int_0^L \lambda_f \frac{\cos\vartheta(X_1)}{\cos\Theta(X_1)} dX_1. \tag{3.3}$$

We assumed that mechanical loading beyond a critical strain threshold, $\varepsilon_{f\text{crit}}$ can initiate damage by degrading the fibril modulus as $E = (1-\xi)E_0$ where E_0 is the Young's modulus of the undamaged fibril and $0 < \xi < 1$ is the damage factor. The stress response to failure measured for the different experimental groups exhibited different rates of strain softening (Fig. 3.2). To capture the softening rate and its alteration with cyclic loading, we applied the following evolution equation adapted from Pena et al. [115] for the fibril damage factor,

$$\frac{d\xi}{dt} = \begin{cases} C(1-\xi)\left(\frac{\widetilde{\varepsilon}_f}{\varepsilon_{f\text{crit}}} - 1\right)\frac{\dot{\widetilde{\varepsilon}}_f}{\varepsilon_{f\text{crit}}} & \text{if } \widetilde{\varepsilon}_f = \max(\widetilde{\varepsilon}_{f\max},\ \varepsilon_{f\text{crit}}) \\ 0 & \text{otherwise,} \end{cases} \tag{3.4}$$

where $C > 0$ is the damage growth rate and $\varepsilon_{f\text{crit}}$ is the threshold strain for damage initiation. The average fibril strain is defined as,

$$\widetilde{\varepsilon}_f = \frac{1}{L}\int_0^L (\lambda_f - 1)\, dX_1, \tag{3.5}$$

and $\widetilde{\varepsilon}_{f\max}$ signifies the maximum $\widetilde{\varepsilon}_f$ of the loading history. Therefore at time $t_{n+1} = t_n + \delta_t$, the damage parameter $\xi_{n+1} = \xi(t_{n+1})$ can be integrated as,

$$\xi_{n+1} = \begin{cases} 1 - \exp\left(-C\left(\frac{\widetilde{\varepsilon}_{f_{n+1}}}{\varepsilon_{f\text{crit}}} - 1\right)^2\right) & \text{if } \widetilde{\varepsilon}_{f_{n+1}} = \max(\widetilde{\varepsilon}_{f\max},\ \varepsilon_{f\text{crit}}) \\ \xi_n & \text{otherwise.} \end{cases} \tag{3.6}$$

Finally, we introduce a renormalized fibril force as,

$$\alpha_0 = \frac{F}{E_0 A}, \tag{3.7}$$

thus $\alpha = \frac{\alpha_0}{1-\xi}$. The fibril damage law is characterized by 2 parameters, the critical strain for damage initiation and the damage growth rate. More complicated models have been developed that use more parameters to describe the strain softening behavior leading up

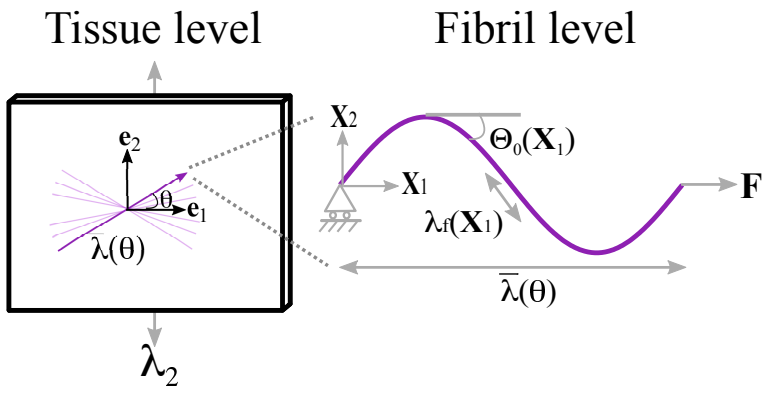

Figure 3.1: Collagen fibrils are represented as planar sinusoidal beams *(right)*, which are described on the tissue level with a fibril orientation distribution $\rho(\theta)$ that is directly obtained from the experimental TEM images *(left)*.

to failure [115]. However, we chose to use a simpler model with a minimum number of parameters to facilitate fitting to experiments. Following Tonge et al. [161], the fibril strain energy density with damage can be written as the sum of a bending component for the straightening of the wavy fibril and an axial component for the axial stretching of the fibril as,

$$\Psi^0_{fib} = \frac{1}{L}\int_0^L \underbrace{\left[\frac{(1-\xi)\,E_0\beta}{8}\left(\vartheta\left(X_1\right)-\Theta\left(X_1\right)\right)^2\right]}_{\Psi^0_{bending}} dX_1 + \frac{1}{L}\int_0^L \underbrace{\left[\frac{(1-\xi)\,E_0}{2}\left(\lambda_f\left(X_1\right)-1\right)^2\right]}_{\Psi^0_{axial}} dX_1, \quad (3.8)$$

where the deformed angle ϑ and axial stretch λ_f are affected by damage through α in Eq. (3.1).

3.3.2 Tissue-level model for the stress response

We assumed at the tissue level that the fibrils deform affinely with the macroscopic deformation gradient $\mathbf{F}$. This allows the fibril to be represented by a material line with orientation

θ and the macroscopic fibril stretch to be computed from the deformation gradient as,

$$\bar{\lambda}(\theta) = \sqrt{\mathbf{C} : (\mathbf{a}_0(\theta) \otimes \mathbf{a}_0(\theta))}, \tag{3.9}$$

where $\mathbf{a}_0$ is a unit vector denoting the fibril direction and $\mathbf{C} = \mathbf{F}^T\mathbf{F}$ is the right Cauchy-Green deformation tensor. The strain energy density of the tissue is assumed to be additively decomposed into an isotropic component for the matrix and an anisotropic component from the fibrils,

$$\Psi = \frac{\mu}{2}(\mathrm{I}_1 - 3) + \int_{-\pi}^{\pi} \Psi_{fiber}\left(\bar{\lambda}(\theta)\right)\rho(\theta)\, d\theta - \frac{p}{2}(I_3 - 1), \tag{3.10}$$

where μ is the shear modulus of the matrix, p the incompressibility constraint, and I_1 and I_3 are the first and third invariants of the right Cauchy-Green deformation tensor. The first Piola-Kirchoff stress response, defined as $\mathbf{P} = \mathbf{F}\left(2\frac{\partial\Psi}{\partial\mathbf{C}}\right)$, can be evaluated for the strain energy density in Eq. (3.10).

$$\mathbf{P} = \mu\mathbf{F} + \int_{-\pi}^{\pi} 2\rho(\theta)\,\mathbf{F}\frac{\partial\Psi_{fib}}{\partial\mathbf{C}}d\theta - p\mathbf{F}^{-T}. \tag{3.11}$$

3.3.3 Material Parameter Determination

For each experimental group, the parameters of the constitutive model, which included the fibril modulus, E_0, slenderness ratio β, and crimp angle Θ_0, were fit to the specimen-averaged uniaxial tension engineering stress-stretch curve up to the failure point, defined by the maximum stress. The zero stress reference point of the stress-stretch curve was determined as the point where all subsequent stress values were non-negative. The stress-stretch curve was then shifted to the right so that the zero stress reference point was set to $\lambda = 1$. This effectively removed the permanent elongation that developed from precondition and that caused the stress to oscillate noisily about zero, creating a well defined toe-region of the stress-strain curve for parameter fitting.

The TEM measurements of the orientation probability distribution function of the pre-conditioned specimens were used for $\rho(\theta)$. To determine the significance of the inter-specimen

variation of the collagen anisotropy, one set of material parameters was fit to the average engineering stress-stretch response for each measured $\rho(\theta)$, yielding three parameter sets for each experimental group.

The uniaxial tension test was simulated by prescribing $F_{22} = \lambda_2$, where λ_2 was the applied vertical deformation in the experiment, and $F_{21} = 0$ to approximate the clamped boundary conditions of the top and bottom surfaces of the specimen. Furthermore, $F_{13} = F_{31} = F_{23} = F_{32} = 0$ because we assumed that the fibrils were oriented in the plane of the tissue. $F_{33} = \frac{1}{F_{11}F_{22}}$ and $p = \mu\left(F_{33}\right)^2$ were solved by assuming incompressibility and plane stress conditions, $P_{33} = 0$, respectively. F_{11} and F_{12} were found by applying traction-free boundary conditions to the $\mathbf{e}_1$ surfaces. For simplicity, we set the matrix shear modulus to $\mu = 0.01$ MPa, because it primarily affected the unknown out-of- plane deformation. A preliminary parameter study showed that μ had a negligible impact on the in-plane stress response for the fibril parameters obtained in Table 3.2.

The material parameters were determined by minimizing the cost function r, defined by the L2-norm of the difference between the computed P_{22} and the experimental uniaxial engineering stress normalized by the number of points n: $r = \frac{1}{n}\sqrt{\sum_{i=1}^{n}\left(P_{22}^i - P_{exp}^i\right)^2}$. The material parameters E_0, Θ_0, and β do not influence the development of damage. Thus, they were fit first to the portion of the stress-stretch curve prior to the inflection point λ_{ip}, where $\frac{d^2P_{22}}{d\lambda^2} > 0$, using the interior-point algorithm of the MATLAB function *fmincon* (MATLAB 9.1). The bounding values given for the material parameters were, 0.001 MPa $< E_0 <$ 1000 MPa, $0 < \Theta_0 < \pi/4$, and $0 < \beta < 0.1$. To check that the resulting material parameter set corresponded to the global minimum of the cost function, the fit was performed using three different initial guesses spanning the full range of the parameter space. All returned the same the converged parameter set. We next fit the damage parameters C and $\varepsilon_{f\text{crit}}$ to the stress-stretch curve up to $\lambda_{ip} + 0.1$, which for most specimens approached the maximum

stress. The damage parameters were fit by evaluating the cost function for a 50×50 evenly spaced grid with the domain $0 < \varepsilon_{f\text{crit}} < 0.3$ and $0 < C < 1$ to find the minimum. The results for all specimens showed that the global minima occurred for $10^{-6} < \varepsilon_{f\text{crit}} < 10^{-1.5}$ and $10^{-6} < C < 10^{-2}$. The solution was refined by calculating the cost function over a finer 40×40 evenly spaced grid in the logarithmic parameter space spanning this range.

3.3.4 Statistical Analysis and Parameter Study

Paired t-tests were applied to analyze for effects of loading cycle and strain amplitude on the fibril properties. The model parameters in Table 3.2 determined for the 50 cycle group ($n = 3$) were compared with those of the 1 cycle group ($n = 3$) of the same strain level to determine whether they were altered significantly altered by cyclic loading. In addition, the parameters obtained for the 13% strain group ($n = 3$) were compared to those of the 26.7% strain group ($n = 3$) for the 50 loading cycle case to determine whether the applied strain amplitude affected the alterations in the fibril properties with cyclic loading.

We next performed a parametric study to evaluate the effect of the parameters and their alterations on the stress-strain response of the DDCS. This was done by first evaluating the baseline stress response for the average the material parameters in Table 3.2 and the average TEM measured orientation distribution function for the 1 cycle, 26.7% strain experimental group. Each parameter was varied one-by-one from the average values of the 1 cycle group to those of the 50 cycle group. The resulting stress-stretch curve was compared to the experimental data to determine whether the alteration was larger than the the variation in the stress-stretch response measured for the 1 cycle group. A similar study was conducted to study the effects of fibril orientation distribution. Simulated stress-stretch curves using averaged parameters in the 1 cycle group from Table 3.2 were plotted with various von Mises distributions to examine the possibility of achieving a similar response to cyclic loading by

Material Parameter	$\varepsilon = 0.13$		$\varepsilon = 0.267$	
	1 cycle	50 cycle	1 cycle	50 cycle
E_0 (MPa)	10.77	13.50	9.53	18.29
	10.99	14.98	8.73	15.782
	10.15	14.35	10.16	17.16
Average	10.64	14.28	9.48	17.08
Θ_0 (rad)	0.54	0.37	0.67	0.54
	0.54	0.37	0.67	0.54
	0.54	0.37	0.67	0.54
Average	0.54	0.37	0.67	0.54
β	0.019	0.012	0.018	0.007
	0.019	0.012	0.019	0.007
	0.019	0.012	0.018	0.007
Average	0.019	0.012	0.018	0.007
$\varepsilon_{f\text{crit}}$	4.87e-03	1.15e-03	8.87e-03	1.30e-03
	6.19e-03	2.10e-03	1.00e-02	2.10e-03
	4.87e-03	2.10e-03	7.87e-03	3.40e-03
Average	5.30e-03	1.79e-03	8.91e-03	2.27e-03
C	2.05e-03	1.00e-04	4.75e-03	1.40e-04
	3.40e-03	3.24e-04	5.62e-03	3.83e-04
	2.05e-03	3.24e-04	3.40e-03	1.05e-03
Average	2.50e-03	2.49e-04	4.59e-03	5.24e-04

Table 3.2: Converged parameters for $\varepsilon = 0.13$ and $\varepsilon = 0.267$ comparing the 1 cycle and 50 cycle preconditioning groups. For all cases, the L2-norm of the difference between the simulation and experimental engineering stress, normalized by the number of points, was less than 5.6×10^{-4} MPa

only changing fibril orientation.

3.4 Results and Discussion

Table 3.2 lists the material parameters determined for each TEM measured fibril orientation distribution function along with the averaged value for each experimental groups. Figure 3.2 shows the stress-stretch curve comparing the average stretch-stress curve to failure measured in experiments for different preconditioning strains and cycles and the model fits for four representative cases in Table 3.2. The modeling fits and cost function for all twelve different

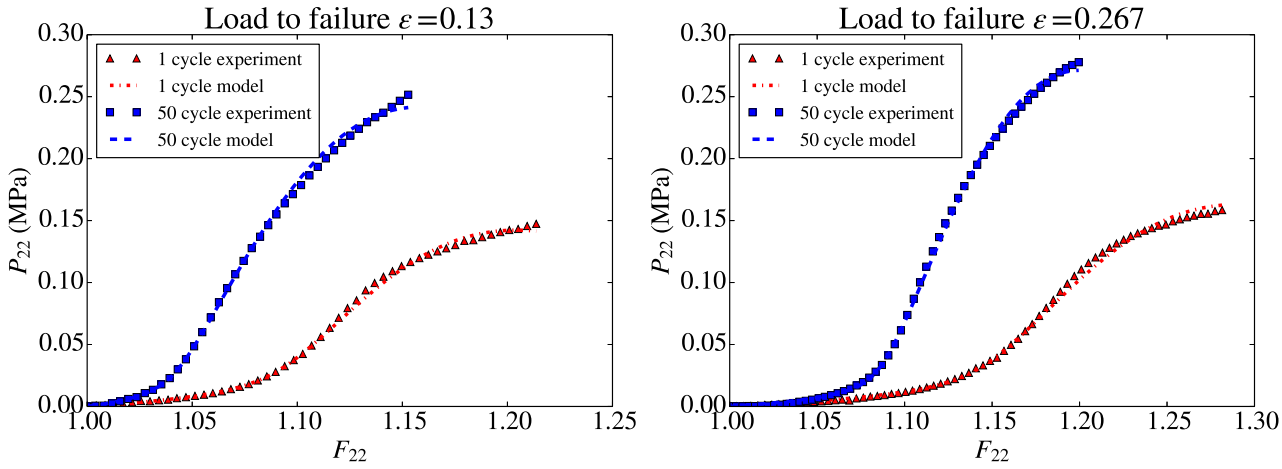

Figure 3.2: Model fits of average load-to-failure experimental stress-stretch curve, after cyclic preconditioning, for $\varepsilon = 0.13$ *(left)* and $\varepsilon = 0.267$ *(right)* for four representative cases in Table 3.2

fibril distributions across all four experimental groups are shown in Figures B.2 and B.3. For all cases, the cost function of the model fit was less than 5.6×10^{-4} MPa, and the average cost function for all cases was 3.6×10^{-4} MPa. While the modeling results for the stress-stretch curves agreed well with the experimental data before the inflection point, the agreement after the onset of damage was poorer. Specifically modeling results exhibited the maximum stress at a smaller strain. There were combinations of parameters $\frac{C}{\varepsilon_{f\text{crit}}^2}$ that resulted in similar values of the cost function and this resulted in larger variations in the damage parameters C and $\varepsilon_{f\text{crit}}$ (Fig. B.4) within the groups as shown in Table 3.2.

The paired t-tests showed that the specimens subjected to 50 preconditioning cycles had a significantly larger E_0 (p =1.56e-02 for 13% strain, $n = 3$ and p =5.80e-03 for 26.7% strain, $n = 3$), a smaller crimp angle Θ_0 (p = 1.39e-06 for 13%, $n = 3$ and p = 2.52e-05 for 26.7%,$n = 3$), and a smaller fibril slenderness ratio β (p =1.57e-04 for 13%, $n = 3$ and p = 2.39e-04 for 26.7%, $n = 3$). For the damage parameters, cyclic loading decreased the damage initiation strain $\varepsilon_{f\text{crit}}$ (p = 1.22e-02 for 13%, $n = 3$ and p =2.60e-02 for 26.7%, $n = 3$) and damage rate C for 26.7% strain (p =4.36e-02 for 26.7%, $n = 3$). A larger change

in the parameters was obtained for the 26.7% applied strain than the 13% applied strain (E_0, p =6.24e-02; Θ_0, p =4.23e-05; β, p =1.60e-03, $\varepsilon_{f\text{crit}}$, p =4.80e-02, C, p =9.81e-02). However, we did not find significant differences in the damage parameter C between the different precondition groups ($p > 0.05$) for 13% strain because of the large variations in the parameter.

For the parameter study, the three fibril orientation distribution functions of each experimental group were averaged and used along with the average material parameters in Table 3.2 to calculate the average stretch-stress curves for the 1 cycle and 50 cycles, 26.7% strain experimental groups. The average stress-stretch curves are plotted in Figure 3.3 along with the results of the parameter study varying each parameter one-by-one from the average values of the 1 cycle group to those of the 50 cycle group. The shaded area in Figure 3.3 denotes the 1 standard deviation range of the measured stress-stretch response for the 1 cycle and 50 cycle 26.7% strain groups. Also plotted in Figure 3.3 is the model stretch-stress curve calculated from the 1 cycle parameters, but with the averaged 50 cycle fibril distribution. This curve lies mostly within the range of experimental stretch-stress curves, which indicates that the differences in anisotropic fibril structure were not sufficient to explain the change in the stress-stretch curve with cyclic loading. To examine the effect of experimental error in measuring the fibril orientation distribution, we evaluated the uniaxial stress-stretch response for the average parameters of the 1 cycle experimental group and various von Mises distributions of the fibril orientations with different average orientation angle, m, and circular variance, $0 < v < 1$. A $v = 1$ signifies a random distribution of fibril orientations, while $v = 0$ denotes perfect alignment along the orientation m. Fitting the von Mises distribution to the average experimentally determined fibril orientation distribution of the 50 cycle, 26.7% group gave $m = 15.8°$ and $v = 0.35$ [156]. The results showed that for $m = 0°$ a significantly smaller $v = 0.12$ was needed for the stress-stretch response to have a linear

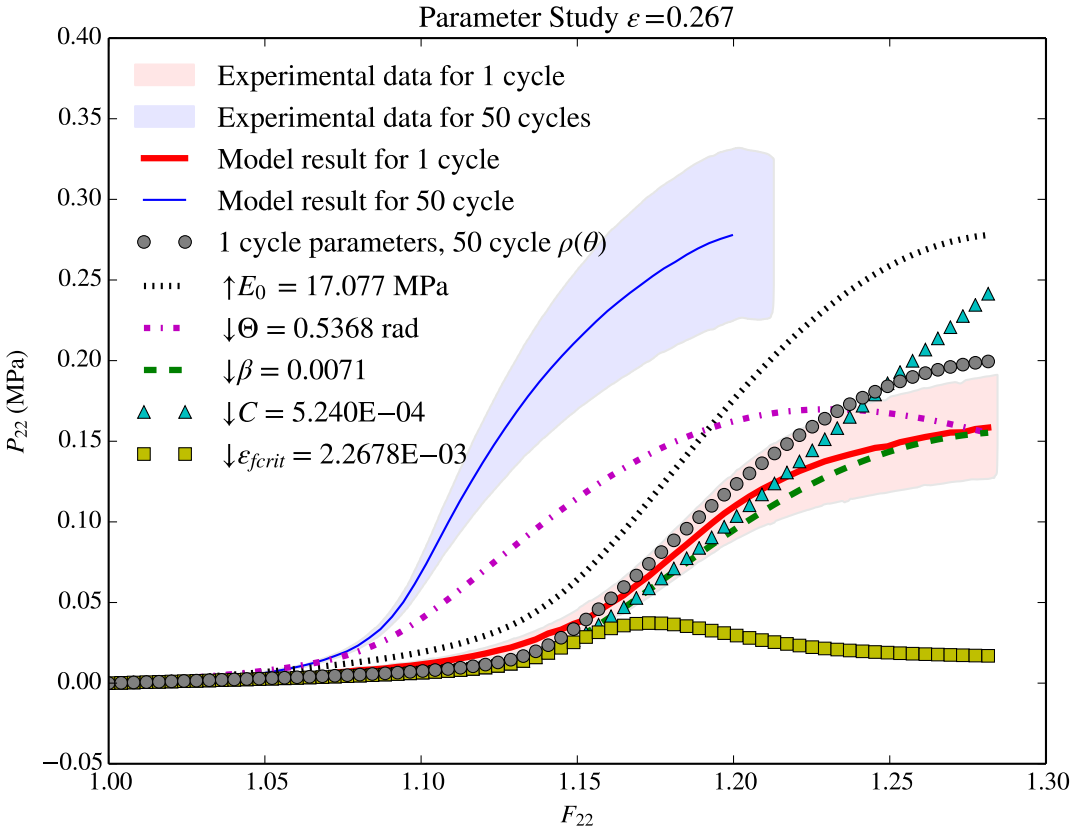

Figure 3.3: Effect of changes in fibril parameters with precondition at 26.7% strain and 50 cycles compared to 1 cycle on the tissue stress response. The shaded bands represent the one standard deviation range of measured stress-stretch curves for the $\varepsilon = 26.7\%$ experimental groups. The solid lines show the model calculations of the stress-stretch response using the averaged fibril parameters in Table 3.2 and the averaged TEM measured orientation distribution function for the $\varepsilon = 26.7\%$ experimental groups.

stiffness similar to the one measured for the 50 cycle group (Fig. 3.4). A greater degree of fibril alignment ($v < 0.12$) would be needed for the slight misalignment $m = 15.8°$ measured in experiments. This significantly higher degree of fibril alignment was not supported by the TEM data.

The crimp angle determines the strain at which the fibril behavior transitions from a bending dominated to a stretching dominated response. Thus, the smaller crimp angle of the 50 cycle group caused a marked decrease in the transition stretch of the strain-stiffening stress-strain curve without affecting the slope of the linear portion of the stretch-stress curve. The smaller slenderness ratio β caused a more compliant bending response, which decreased the slope of the toe-region and increased the transition stretch without noticeably affecting the linear portion of the stretch-stress curve. The larger effective stiffness E_0 of the fibril of the 50 cycle group caused a significant increase in the slope of the linear region of the stress-stretch curve without affecting the transition stretch. Both the variation in the crimp angle and effective fibril stiffness caused the baseline stress-strain curve to stiffen beyond the range of experimental variations measured for the stress response of the 1 cycle group, the former by decreasing the transition stretch and the latter by increasing the stiffness of the linear region of the stress-stretch curve, which suggests that cyclic loading increased the effective stiffness of the collagen fibrils and decreased the waviness of the collagen fibrils.

The smaller $\varepsilon_{f\text{crit}}$ of the 50 cycle group caused damage to initiate in the fibrils at an earlier strain. In the parameter study, this produced a significantly softer tissue-level stress-strain curve beyond the experimental variation. However, the smaller damage growth rate C of the 50 cycle group resulted in a larger tissue-level failure strain and failure stress in the parameter study, counteracting the decrease in the damage initiation strain. Experiments showed that the 50 cycle group had a smaller tissue failure strain. Moreover the decrease in C for the 50 cycle group was not statistically significant. Thus, the experimentally observed increase

in strength of dense collagen substrates with cyclic loading was likely caused mainly by the increase in the intrinsic fibril axial stiffness. Mubyana and Corr [101] measured the effect of cyclic loading on the stiffness and strength of developing tendon construction mediated by fibroblasts. They also observed an increase in the stiffness of the developing tendon fibers with cyclic loading, but did not find a change in failure strain.

3.5 Conclusions

We applied a micromechanical model for the nonlinear anisotropic behavior of collagen tissues to analyze the experimental measurements of Susilo et al. [156] and investigated the effects of cyclic loading on the mechanical properties of collagen fibrils in an acelluar collagen substrate. The anisotropic behavior of the tissues was described by the probability density distribution of collagen fibril orientation measured after cyclic loading using TEM. The parameters of the model described the fibril properties, including the axial stiffness, initial crimp angle, slenderness ratio, threshold strain for damage initiation, and damage growth rate. These were determined by fitting the experimentally measured uniaxial tension response to failure. We evaluated a different set of material parameters for each TEM measurement of the collagen structure to evaluate whether differences in the fibril material properties between the different experimental groups were greater than those caused by variations in the TEM measurements of collagen anisotropy. The main findings of this work are:

1. Cyclic loading increased the effective stiffness and decreased the crimp angle and the slenderness ratio of the collagen fibrils significantly in the dense disorganized collagenous substrates. The variation in these properties between experimental groups were greater than that caused by variations in the anisotropic fibril structure measured within the groups.

2. Cyclic loading significantly decreased the fibril damage initiation strain, which de-

creased the tissue-level failure strain and strength. This effect was mitigated by the decrease in the fibril damage growth rate, which increased the tissue-level failure strength and stress. However, the decrease in the fibril damage growth rate was not statistically significant.

3. The experimentally measured increase in the failure strength of the tissue construct may be attributed mainly to the increase in the effective fibril axial stiffness.

These findings suggest that cyclic loading increased the effective stiffness of collagen fibrils in the dense disorganized collagen substrates. The increased fibril stiffness, rather than changes in the anisotropic structure and the damage initiation strain, was responsible for the large increase in stiffness in the linear region and the increased strength observed in experiments after cyclic loading. Recall also that experiments did not measure alterations in the areal density of the collagen fibrils with cyclic loading.

The micromechanical model is based on a number of assumptions. The model assumed that the collagen fibrils are arranged all in a plane and deform affinely with the macroscopic deformation gradient. In contrast, TEM of the substrates showed short collagen fibrils, which may interweave out of the plane. Such materials would be described more appropriately using discrete fiber models that do not rely on the affine deformation assumption. Analysis using a discrete fiber model would likely return a larger fibril stiffness for all cases. Although the DDCS did not contain a cross-linking agent in the medium, some of the stiffening behavior exhibited may be caused by changes in the inter-fibrillar cross-linking and connectivity of the fiber network that this work does not take into consideration, such as those observed by Zhang and Sacks [176] for exogenously crosslinked bioprosthetic tissue. Accounting for interfibrillar interactions, such as in the structural model of Sacks et al. [144] and discrete network model of Huisman et al. [76], may cause fibril alignment with the loading direction to produce a more significant network stiffening response. The micromechanical model relies

on the assumptions of small crimp angles, which allowed for approximating the undeformed rotation angle of the midline as $\tan\Theta \sim \Theta$ and for linearizing the differential equation for the deformed rotation angle to obtain the solution shown in Eq. (3.1). The error associated with these linear approximations are on the order of $\frac{1}{3}\Theta^3$, which is 0.12 radians for the largest crimp angle 0.67 radians determined for the 1 cycle, 26.7% experimental group. The micromechanical model also attributed the toe region of the stress-strain curve to the straightening of wavy fibrils. While TEM images showed curved fibrils, the fibrils were too short to measure a crimp angle to compare to the modeling predictions. Moreover, the toe region of the stress-curve can be caused by the non-affine rotation and deformation of the short collagen fibrils in addition to their straightening, which the currently model cannot capture. We applied a simple 2 parameter damage law to describe the softening stress response at large strains. However, the model predicted failure at smaller strains and more rapid softening in the stress response than experimental data. A more sophisticated damage law may be able to provide a better fit for the damage properties.

Overall, the findings of this work demonstrated that cyclic mechanical loading in an acellular environment can increase the effective stiffness of the collagen fibril network independent of the anisotropic structure of the network. Further studies elucidating these chemomechanical processes and how they contribute to collagen remodeling is important for the engineering of collagen tissues and for understanding how biological tissues remodel in response to physiological and pathological changes in mechanical loading.

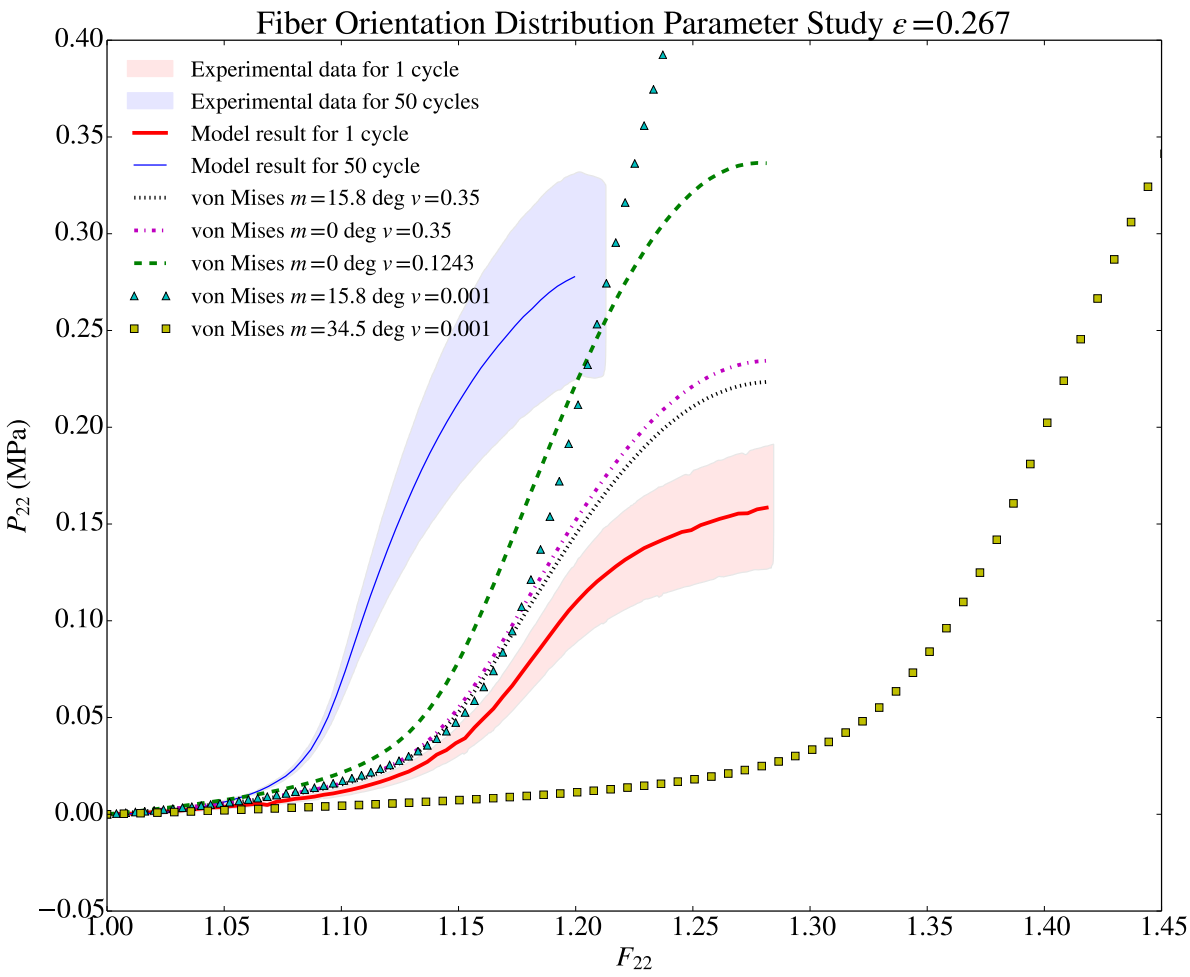

Figure 3.4: Effect of changes in fibril orientation distribution with cyclic loading at 26.7% on the tissue stress response. The shaded bands represent the one standard deviation range measured for the uniaxial stress response for the $\varepsilon = 26.7\%$ 1cycle and 50 cycle experimental groups. The solid lines show the model calculations of the uniaxial stress response using the averaged fibril parameters in Table 3.2 and the averaged TEM measured orientation distribution function for the $\varepsilon = 26.7\%$ experimental groups. Non-solid lines are the stress response evaluated for the average parameters of the 26.7%, 1 cycle group and various von Mises fibril orientation distributions functions with different average fibril orientation m and is the circular variance v, which signifies the degree of fibril alignment. The stress-stretch curve for $m = 34.5°$ $v = 0.001$ (yellow squares) and $m = 0°$ $v = 0.12$ (green dashed) have a similar linear stiffness to the experimental result for the 26.7%, 50 cycle group.

Chapter 4

Remodeling of the sclera in a mouse model of glaucoma

This chapter developed an inverse finite element analysis (FEA) to fit the parameters of the micromechanical model in Chapter 3 to determine the changes in the mechanical properties and morphology of the collagen fibers in the sclera of glaucoma mouse eyes. One eye of a CD1 mouse was subject to chronic pressure elevation to induce glaucoma axon damage and remodeling of the scleral tissue, and the other was left as control. The individual effects of the structural and material property changes from glaucoma on the pressure-displacement inflation response of mice sclera were then investigated.

4.1 Introduction

The scleral structure and its mechanical properties directly inform how the stress generated by the intraocular pressure (IOP) is translated to the optic nerve head (ONH) region, the principal damage site to retinal ganglion cells (RGCs) in glaucoma [2]. Imbalances in the growth and remodeling process may alter the scleral mechanical properties such that even at physiological levels of IOP, pathological levels of stress at the ONH occur [19]. There is evidence that glaucoma is associated with permanent alterations to scleral mechanical and structural properties.

Experiments have found differences in the inflation response and mechanical properties of normal and glaucoma eyes. Downs et al. [44] performed uniaxial tension tests on scleral specimen from monkey eyes. They showed that eyes with early-onset glaucoma had a larger relaxation time and a greater equilibrium modulus, a measure of long-term tissue stiffness after the material has fully relaxed from a rapid deformation, than normal eyes. Coudrillier et al. [35] compared the inflation response of glaucoma eyes at different stages of damage with normal eyes. The authors showed that glaucoma human eyes had a stiffer pressure-strain response in the meridional direction and a slower circumferential creep rate in the peripapillary sclera compared to normal eyes. Nguyen et al. [110] found that experimental glaucoma mouse eyes exposed to chronic IOP elevation had a stiffer pressure-strain response in both the circumferential and meridional directions than normal eyes.

Structural changes have also been measured. Nguyen et al. [110] reported axially longer and wider eyes, and a thinner scleral shell in glaucoma mouse eyes (Table 4.1). In a separate study, Downs et al. [43] found that the sclera progressively thins from the fovea to the equator in monkey eyes with ocular hypertension and monkey eyes with glaucoma. Coudrillier et al. [35], found no significant difference in scleral thickness in human glaucoma and normal eyes.

It has been suggested that changes in the scleral extracellular matrix (ECM) may contribute to the development of glaucoma [71]. Within the scleral ECM, collagen serves as the primary load-bearing component and dominates the anisotropic large-strain mechanical response of the tissue. Collagen fibers have a slight intrinsic crimp and are much stiffer than their surrounding matrix. As strain on the collagen fiber increases, the fiber progressively straightens and begins to axially stretch, giving the scleral tissue its characteristic non-linear "J-shaped" strain stiffening response [73, 169]. Recent studies have investigated the changes in the collagen network structure from glaucoma.

Quigley et al. [129] observed from electron microscopy images that the collagen fibers

	Axial length	Width (N-T)	Width (S-I)	Sec 1	Sec 2	Sec 3	Sec4	Sec 5
Glaucoma	3.84	3.74	3.61	48.7	41.1	36.8	34.5	35.6
Control	3.53	3.52	3.48	55.1	46.0	40.4	38.1	38.4

Table 4.1: Reported average structural changes between glaucoma CD1 mice eyes and control CD1 mice eyes. Data obtained from Table 1 in Nguyen et al. [110]. Width is reported in millimeters and thickness in micrometers. Thickness was measured in 5 sections, where Section 1 represents the area closest to the scleral apex and Section 5 represents the area closest to the fixture near the limbus.

were oriented more randomly in human glaucoma eyes than normal eyes. Pijanka et al. were able map changes in collagen fiber alignment in the posterior sclera using wide-angle x-ray scattering (WAXS), in mice [120] (Figure 4.1) and humans [119]. Pijanka et al. found that fiber orientations were less aligned in the glaucoma eyes (i.e. more isotropic), but found no overall differences in the dominant orientation between normal and glaucoma eyes. In the peripapillary sclera, they found a circumferential ring of fibers encircling the ONH. In the midposterior region, the collagen orientation is more isotropic. Pijanka et al. did not map the collagen fiber alignment near the limbus, however, a previous study by Boote et al. [14] showed that the collagen fibers are highly aligned near the limbus, and form an annulus that circumscribes the cornea.

While changes in the collagen fiber isotopy may contribute to the differences in mechanical behavior observed in normal and glaucoma eyes, how these microstructural changes affect the overall tissue response is not well understood. Coudrillier et al. estimated the material properties of glaucoma and human sclera [38], and found increases in matrix and fiber stiffness with increasing states of glaucoma damage that were not statistically significant.

The object of this study was to examine the effect of changes in the geometry of the sclera, collagen anisotropic structure, and material properties from glaucoma on the inflation response of the sclera. Measurements of the average change in the collagen structure, average changes in thickness, and diameters of the sclera, were taken from experimental data by

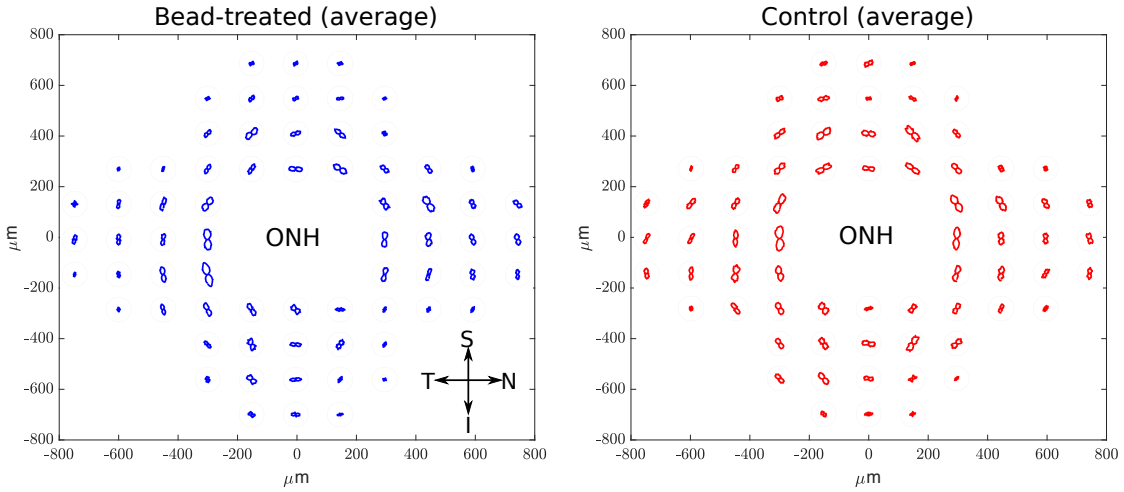

Figure 4.1: Polar maps of preferential collagen fiber orientation in the posterior sclera. Data from Pijanka et al. 2014 [120].

Pijanka et al. and Nguyen et al. [120, 110]. Finite element models of the posterior sclerae were created using the method of of Myers et al. [108] to exhibit the average thickness and diameters for each scleral section measured by Nguyen et al. for CD1 glaucoma and normal eyes (Table 4.1). An inverse FEA was applied to fit the parameters of the micromechanical model to the average pressure-displacement data from inflation tests of glaucoma and normal mouse eyes. The parameters of the micromechanical model describe the elastic properties of the collagen fiber and surrounding isotropic matrix and fiber morphology. A parametric study was designed to evaluate the individual contributions of changes in the parameters of the sclera of glaucoma eyes.

4.2 Experimental Methods

The following sections provide a brief summary of the mechanical testing, and imaging methods used in the experimental studies of Nguyen et al. (2013) [110] and Pijanka et al. (2014) [120].

4.2.1 Mechanical Testing

Four month old CD1 albino mice were anesthetized by an intraperitoneal injection of 50 mg/kg of ketamine, 10 mg/kg of xylazine, and 2 mg/kg of acepromazine. Glaucoma was induced in one eye of each mouse by the 4+1 bead injection protocol [30], where 2μL of 6 μm diameter beads (3×10^6 beads/μL concentration), followed by 2 μL of 1 μm diameter beads (1.5×10^7 beads/μL concentration) (Polybead Microspheres; Polysciences, Inc., Warrington, PA), and 1 μL of 10 mg/mL sodium hyaluronate (Healon; Advanced Medical Optics, Inc., Santa Ana, CA). The other eye of the mouse was left for scientific control. After 6 weeks, the mice received general anesthesia before sacrifice by exsanguination. The eyes were then enucleated and measured for axial length and width. Thickness was measured in 5 different sections from the peripapillary area to the limbus in the superior quadrant of the sclera, using an eyepiece micrometer [110] (Table 4.1).

Twenty CD1 control eyes and 20 CD1 glaucoma eyes underwent inflation testing. The eyes were glued to a custom fixture at the limbus using cyanoacrylate. To minimize dehydration, the tissue surface was kept moist with phosphate buffered saline. A needle connected to a programmable syringe-pump was inserted just anterior to the limbus [107]. The intraocular pressure of the specimen was measured using an in-line pressure transducer. Testing began at a baseline pressure of 0.80 - 1.07 kPa, when the sclera was not visibly wrinkled, and IOP was increased at a rate of 0.033 kPa/s to a final pressure of 4.00 kPa via syringe actuation. To capture the deformation of the posterior scleral edge, a CCD video camera (Grasshopper, model Gras-20S4M-C; Point Grey Research, Inc., Richmond, BC, Canada) connected to a dissecting microscope (Stereomicroscope Stemi 2000-CS; Carl Zeiss Microscopy, LLC, Thornwood, NY), was used to image the deforming sclera in profile. The two-dimensional (2-D) displacements were calculated from the images using a commercial digital image correlation (DIC) software (Vic-2D, Correlated Solutions, Columbia, SC), with an error of $\pm$0.46 μm.

4.2.2 Fiber orientation characterization

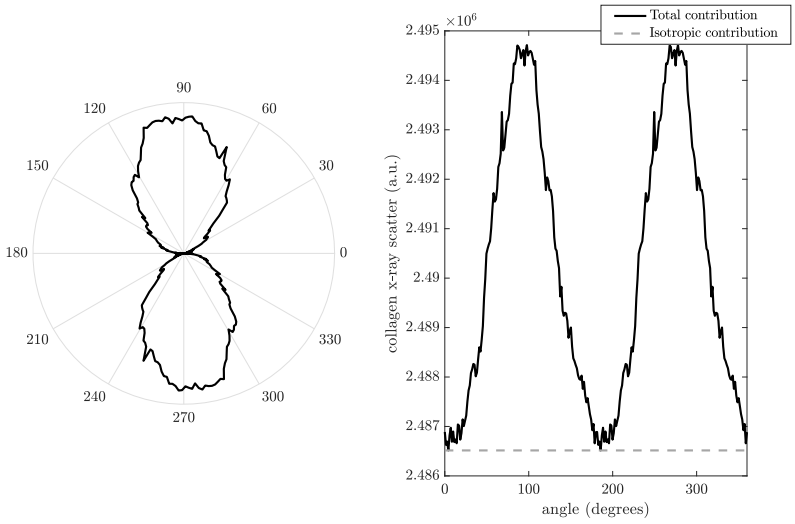

Figure 4.2: *(Left)* Polar vector plot displaying the aligned collagen scatter at a representative point on the peripapillary sclera. The shape shows the collagen anisotropy. *(Right)* The angular X-ray scatter intensity profile at the same representative point. The total scatter intensity can be decomposed into an isotropic component and an anisotropic component. Data from Pijanka et al. 2014 [120].

Twelve 9 month old CD1 mice eyes were analyzed using WAXS to determine the scleral collagen organization. Anesthesia and bead-injection procedures followed the same protocols described in the previous subsection (Section 4.2.1). Animals were euthanized 6 weeks after injection, and the eyes enucleated. The optic nerves were excised for qualitative evaluation of RGC damage, and the rest of the eyes were stored in a 4% paraformaldehyde solution. For the WAXS analysis, the cornea and anterior sclera were then removed and the posterior scleral cup flattened by making 5 meridional incisions from the equator to the midposterior sclera. A Beamline I02 at the Diamond Light Source UK synchrotron (Didcot, UK) was used for the WAXS experiments. The specimen was mounted on a stage that can translate in the plane and a 100 micron X-ray beam was used to map the scattering intensity at 68 points in a region within a 1.5 mm radius of the ONH. The WAXS intensity patterns provide a thickness-

averaged distribution of the fiber orientation angle. The WAXS intensity profile was further divided into anisotropic and isotropic components. The scattering intensity distribution was normalized and used directly to describe the local probability density function of fibers oriented in the θ direction, $\rho(\theta)$.

4.3 Modeling Methods

4.3.1 Geometry

To define the average scleral 2-D displacement for normal and glaucoma eyes from the experimental data (Section 4.2.1), the displacement of 7 control eyes were averaged together and the displacement of 7 glaucoma eyes were averaged together. The position of the scleral edge for each specimen was centered on a grid where the positive horizontal axis represented the temporal direction and the negative horizontal axis represented the nasal direction. The scleral apex, defined as the midpoint between the closest correlated tracking locations on either side of the ONH, lays on the vertical intercept of the grid (Figure 4.3). Poorly correlated data, near the limbus where the sclera was affixed, was discarded. Because DIC does not export displacements at regular grid points, to find the average displacement of the scleral edge at a given point on the nasal-temporal axis, an interpolation function was used (*interp1*, spline method, MATLAB 9.1, Natick, MA). The scleral edge displacement was interpolated from the experimental data every 10 μm along the nasal-temporal axis. This was done for 5 evenly spaced pressure states from 1.07 kPa to 4.00 kPa for each eye. The interpolated curves across the 7 eyes in each experimental group were then averaged together for every pressure state.

The nasal scleral edge for each experimental group was reconstructed by using the average measurements taken from the DIC images at the baseline pressure of 1.07 kPa. A rotated ellipse was fit to the averaged coordinates of the measured reference position of the nasal

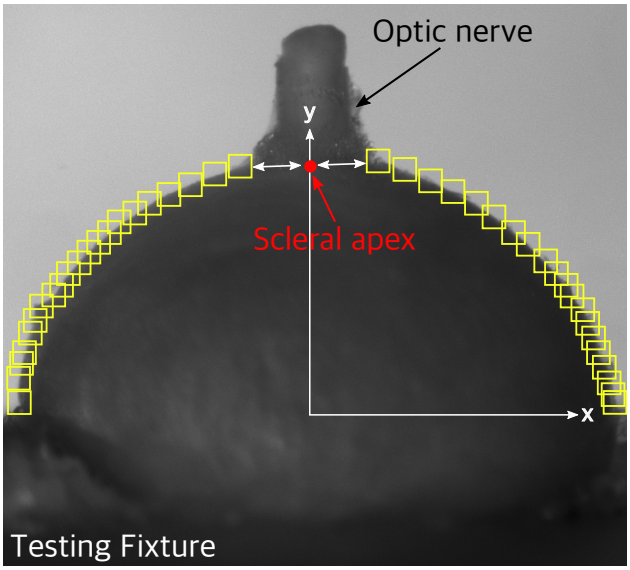

Figure 4.3: A snapshot from the DIC video of a normal CD1 mouse eye at the baseline pressure. Yellow boxes show the DIC tracking locations along the scleral edge. The scleral apex is defined as the midpoint between the closest correlated tracking locations on either side of the ONH. Image courtesy of Cathy Nguyen and Harry Quigley.

edge. This formed the outer edge of the scleral shell. A second rotated ellipse was fit to the average thickness measurements recorded by Nguyen et al. [110] to form the inner scleral edge. Then the inner and outer scleral edges were rotated 360° to form the scleral shell. The dimensions of the shell were adjusted by a multiplier such that it matched the average superior-inferior width and average nasal-temporal width reported [110] (Table 4.1). The finite element mesh generated with this geometry was discretized with trilinear hexahedral elements, with 3 elements spanning the thickness. The finite element meshes contained 7056 elements for the averaged CD1 control mouse eye geometry and 6180 elements for the averaged CD1 glaucoma mouse eye geometry, and each element contained its own probability density distribution of collagen fiber orientation distribution (Figure 4.4).

The fiber orientation probability density distribution near the peripapillary sclera was determined from the normalized WAXS intensity $\rho(\theta)$ measured by Pijanka et al. [120] (Figure 4.1). The WAXS data was measured on a flattened scleral shell, and the locations

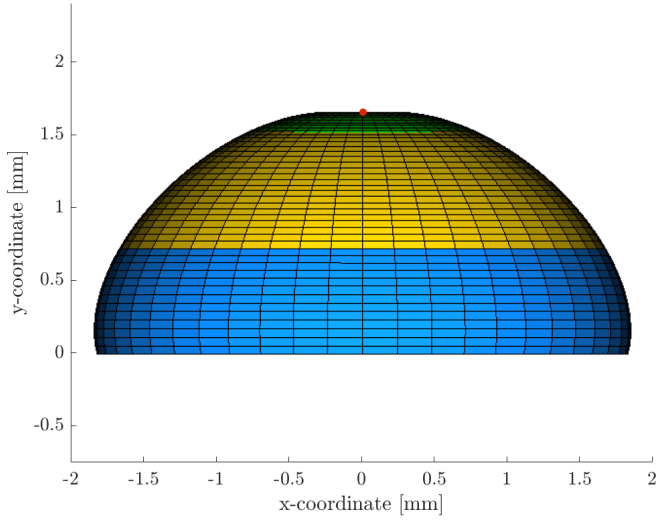

Figure 4.4: Representative finite element mesh. Blue represents the anisotropic limbus region, yellow the isotropic mid-posterior sclera region, and green the anisotropic region near the ONH. Red dot represents the scleral apex.

of the 68 regions polar maps were interpolated to the three-dimensional (3-D) FEM mesh of the sclera. The reported 2-D locations of these polar maps were represented as a plane located just above the apex of the sclera. The plane was projected down onto the curved outer scleral surface to determine the corresponding 3-D coordinates. The fiber orientation distribution of elements located between the reported 68 regions were assumed to be the normalized weighted average of their nearest neighbor regions. The region within 500 μm of the limbus was assumed to have preferentially circumferentially aligned collagen fibers with the parameter n_{limbus} concentration, where $n_{\text{limbus}} = 0$ represented a transversely isotropic case, and larger values represented increasing alignment. Because the DIC scleral displacement data near the limbus was excluded because of poor correlation, a value for the parameter $n_{\text{limbus}} = 6$ was chosen and fixed. This value is within the range of n_{limbus} found by Myers et al. for 11 month CD1 normal mouse eyes [108]. In the region near the mid-posterior sclera where there is no WAXS data and beyond 500 μm of the limbus, the

fiber orientation was assumed to be transversely isotropic.

4.3.2 Constitutive Model

The following sections describe the constitutive model used for the sclera. A micromechanical model was used to describe the collagen fibers. The matrix is assumed to to contain all non-fiberlar collagen constituents, e.g. cells, elastin, and proteoglycans. The constitutive model was implemented in the finite element code Tahoe[1]. (Sandia National Labs, Livermore, CA).

Fiber-level model

To derive the strain energy density of the collagen fibers, we apply the wavy elastica model developed by Comininou and Yannas [28]. This model is explained in detail in Chapter 3, but in short, the model represents the undeformed fiber as a simply supported planar sinusoidal beam, $X_2 = a \sin(bX_1)$ where $(X_1,\ X_2)$ are the coordinates along the horizontal and vertical axes. The "waviness" of the undeformed fiber is represented by the crimp angle, $\Theta_0 = ab$, the maximum angle the fiber makes with the horizontal axis, and the wave length of the fiber by $L = 2\pi/b$. The bending stiffness of the fiber is described by $E\beta$, where E is the Young's modulus of the fiber, $\beta = b^2r^2$ is the slenderness ratio, and r is the fiber radius. A horizontal force applied at the tip of the fiber $X_1 = L$, causes the fiber to first bend (straighten) and then axially stretch, describing the strain-stiffening behavior of the collagen fibers [161]. The resulting fiber macrostretch is defined as $\bar{\lambda}$, the ratio of deformed to undeformed wave length. The macrostretch $\bar{\lambda}$, as well as the deformed rotation angle, ϑ, and the axial stretch of the fiber midline, microstretch λ_f, can be solved analytically [161, 28, 26]. The fiber strain energy density is written as the sum of a bending component for the straightening of the wavy fiber and an axial component for the axial stretching of

[1] http://sourceforge.net/projects/tahoe/

the fiber as,

$$\Psi_{fib} = \frac{1}{L}\int_0^L \underbrace{\left[\frac{E\beta}{8}\left(\vartheta\left(X_1\right) - \Theta\left(X_1\right)\right)^2\right]}_{\Psi_{bending}} dX_1 + \frac{1}{L}\int_0^L \underbrace{\left[\frac{E}{2}\left(\lambda_f\left(X_1\right) - 1\right)^2\right]}_{\Psi_{axial}} dX_1. \tag{4.1}$$

Tissue-level model

At the tissue level, we assume the fibers deform affinely with the macroscopic deformation gradient, $\mathbf{F} = \partial\mathbf{x}/\partial\mathbf{X}$, where $\mathbf{X}$ denotes the undeformed coordinates of the material points and $\mathbf{x}$ the deformed coordinates. Then we can represent the macrostretch of a collagen fiber whose midline oriented in the θ direction as $\bar{\lambda}\left(\theta\right) = \sqrt{\mathbf{C} : \left(\mathbf{a}_0\left(\theta\right) \otimes \mathbf{a}_0\left(\theta\right)\right)}$, where $\mathbf{a}_0\left(\theta\right)$ is the unit orientation vector in the θ direction, and $\mathbf{C} = \mathbf{F}^{\mathrm{T}}\mathbf{F}$ the right Cauchy-Green deformation tensor. The strain energy density of the tissue is assumed to be additively decomposed into an isotropic, quasi-incompressible Neo-Hookean component for the matrix and an anisotropic component from the fibers:

$$\Psi = \underbrace{\frac{\mu}{2}\left(\bar{I}_1 - 3\right) + \frac{\kappa}{2}\left(I_3 - \ln\left(I_3\right) - 1\right)}_{\Psi_{matrix}} + \int_{-\pi}^{\pi} \Psi_{fib}\left(\bar{\lambda}\left(\theta\right)\right)\rho\left(\theta\right)d\theta \tag{4.2}$$

where μ is the shear modulus of the matrix, κ is the bulk modulus of the matrix, and $\bar{I}_1 = I_3^{-\frac{1}{3}} I_1$ is the distortional part of the first invariant of $\mathbf{C}$ ($I_1 = \mathrm{trace}\left[\mathbf{C}\right]$ and $I_3 = \det\left[\mathbf{C}\right]$). The value of $\kappa = 70$ MPa was fixed, a sufficiently large value to ensure incompressibility.

4.3.3 Inverse finite element method for parameter estimation

The material behavior of the sclera inflation was described by the following four parameters: the matrix shear modulus μ, the fiber stiffness E, the fiber slenderness ratio β, and the fiber crimp angle Θ_0. The parameters were determined by minimizing the difference between the averaged DIC displacement measurements and the model predictions at 5 evenly spaced

pressure states from 1.07 kPa to 4.00 kPa. Mathematically, this problem can be formulated as the minimization of the cost function C,

$$C = \frac{1}{n_{nodes} n_{steps}} \sqrt{\sum_{p=1}^{n_{steps}} \sum_{q=1}^{n_{nodes}} \left(\mathbf{u}_p^{Exp}(\mathbf{x}_q) - \mathbf{u}_p^{FEA}(\mathbf{x}_q)\right) \cdot \left(\mathbf{u}_p^{Exp}(\mathbf{x}_q) - \mathbf{u}_p^{FEA}(\mathbf{x}_q)\right)} \tag{4.3}$$

where n_{nodes} is the number of nodes on the scleral edge, $n_{steps} = 5$, $\mathbf{u}_p^{Exp}(\mathbf{x}_q)$ is the displacement vector of node q from the averaged DIC measurements at pressure level p, and $\mathbf{u}_p^{FEA}(\mathbf{x}_q)$ is the model prediction for node q at pressure level p.

Because of the computational expense of the model, the inverse FEA was performed in two steps. In the first step, the collagen anisotropy near the ONH was approximated as a von Mises function fit to the average WAXS data. The cost function was evaluated over the parameter range $\mu : [0.01 - 1\text{MPa}]$, $E = [1 - 30\ \text{MPa}]$, $\beta = [0.001 - 0.1]$, $\Theta_0 = [0 - 45^\circ]$ to find a subset of parameter ranges where $C < 0.2\ \mu$m. In the second step, the collagen anisotropy near the ONH was represented on an element-by-element basis directly from the WAXS data, as reported in Section 4.3.1. The reduced subset of parameter ranges from the first step were reevaluated, to find the combination that minimized the cost function. The approximation used in the first step was validated by comparing the cost function calculated in step 1 and the cost function calculated in step 2 for the same set of parameters. The average percent difference was less than 3%, which was deemed sufficiently small.

4.3.4 Parameter studies

A parameter study was conducted to evaluate the contribution of the material property changes to the pressure-displacement response at the scleral apex. First, the pressure-displacement response at the scleral apex was plotted using the experimental data, and then calculated using the material properties determined from inverse FEA (Table 4.2). The pressure-displacement response for the scleral apex of the average normal eye calculated

	E (MPa)	Θ_0 (degrees)	β	μ(MPa)
Control	7.0	14.32	0.010	0.40
Bead-treated glaucoma	9.0	12.03	0.011	0.42

Table 4.2: Fitted parameters for the average control eye and average glaucoma eye.

with the inverse FEA parameters, was defined as the baseline curve. Then, the material and structural parameters were varied one-by-one from the baseline case to the value of the glaucoma case. The parameters studied were E, Θ_0, β, μ, $\rho(\theta)$, scleral thickness, and overall scleral geometry. The displacement of the scleral apex at the maximum pressure, $p = 4.00$ kPa, for any given pressure-displacement curve is represented by $\mathbf{u}_{\max}^{param}$. $\mathbf{u}_{\max}^{n}$ and $\mathbf{u}_{\max}^{g}$ are the $\mathbf{u}_{\max}^{param}$ for the average normal and glaucoma curves calculated from the inverse FEA parameters, respectively. Finally, we define the normalized change in maximum displacement, $\Delta\mathbf{u}_{\max}$ as,

$$\Delta\mathbf{u}_{\max} = \frac{\mathbf{u}_{\max}^{param} - \mathbf{u}_{\max}^{n}}{\mathbf{u}_{\max}^{g} - \mathbf{u}_{\max}^{n}} \tag{4.4}$$

where $\Delta\mathbf{u}_{\max} = 0$ when $\mathbf{u}_{\max}^{param} = \mathbf{u}_{\max}^{n}$ and $\Delta\mathbf{u}_{\max} = 1$ when $\mathbf{u}_{\max}^{param} = \mathbf{u}_{\max}^{g}$. The normalized change in maximum displacement, $\Delta\mathbf{u}_{\max}$ gives a quantitative description of how much the displacement response shifts as an effect of parameter change at high pressures, relative to the baseline curve. A positive $\Delta\mathbf{u}_{\max}$ value implies a stiffer pressure-displacement response at high pressures and a negative $\Delta\mathbf{u}_{\max}$ value implies a more compliant pressure-displacement response at high pressures.

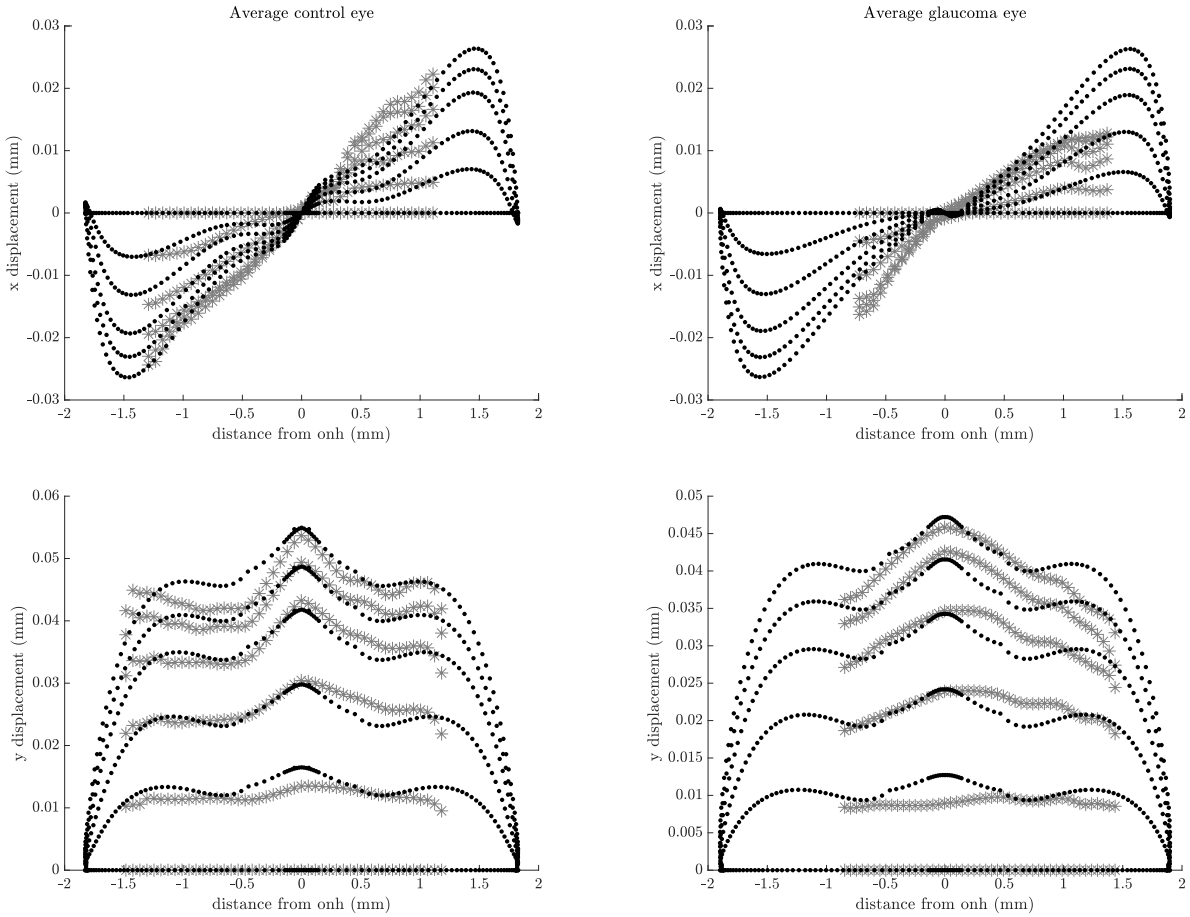

Figure 4.5: Model fits (black dots) of the *(left)* average control eye *(right)* average glaucoma eye to the experimental scleral edge displacements (grey asterisk) at 5 evenly spaced pressure states from 1.07 kPa to 4.00 kPa.

4.4 Results and discussion

4.4.1 Parameter fitting

The fitted material parameters showed that the average glaucoma eye had a 28.6% higher fiber stiffness modulus E, a 16.0% smaller initial crimp angle Θ_0, a 5% increase in fiber slenderness ratio β , and a 10% increase in matrix shear modulus μ (Table 4.2).

The model is able to capture the deformation response at high pressures (Figure 4.5). The cost function of the model fit for the average control eye was $C = 0.098$ μm and the

cost function of the model fit for the average glaucoma eye was $C = 0.104$ μm.

However, the model is not able to accurately represent the deformation response at low pressures for the average normal eye or glaucoma eye. This is in part because the experimental pressure-displacement curve is not the expected "J-shaped" curve. Instead, the "toe" region exhibited an initially stiff response followed by strain softening 4.6. The initially stiff response in the "toe" region is more prominent in the glaucoma eyes than the control eyes. This behavior is not evident in other inflation tests of normal mouse sclera [107, 155, 82] or other animal sclera [105, 86, 171], and may be from experimental error. The model is not able to capture this initial stiffening response, and as a result, underpredicts the displacement at low pressures.

Additionally, the experimental scleral edge displacements were not symmetric. Equidistant from the scleral apex, the displacements on the nasal side were larger than the displacements on the temporal side (an average of 0.153 microns larger in the average normal eye and an average of 0.140 microns larger in the average glaucoma eye). In the model, the finite element mesh is symmetric on the nasal side and the temporal side, and the only difference is the variation in regional collagen anisotropy. As a result, the model displacements are much more symmetric.

4.4.2 Parameter Studies

The parameter study depicts the simulated effect of material parameter changes (Figure 4.6, top), and structure changes (Figure 4.6, bottom) on the pressure-displacement behavior at the scleral apex. The structural features and material properties are changed one-by-one from the value for the baseline case, representative of the averaged normal mouse eye, to the ones for the glaucoma mouse eye.The solid line represents the pressure-displacement curves of the simulations, and the dashed lines represent the experimental pressure-displacement response, averaged across mice. The shaded bands represent the one standard deviation experiment

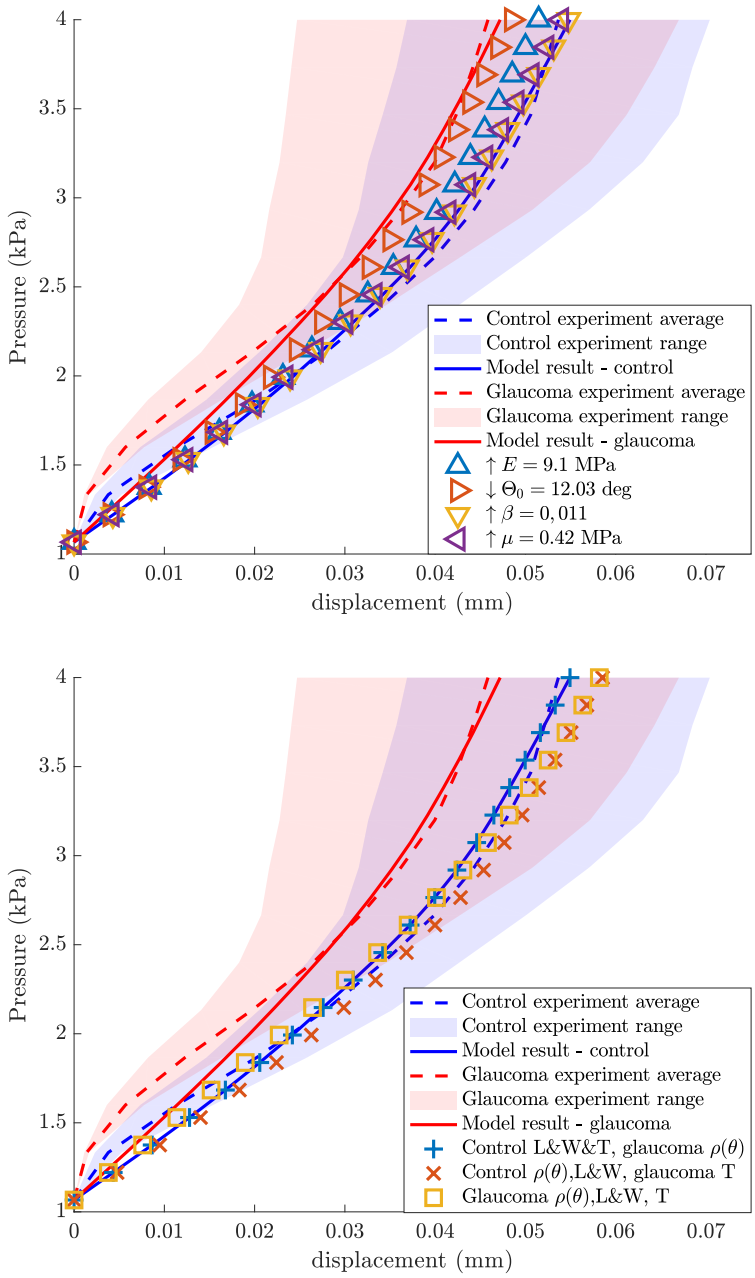

Figure 4.6: Effect of changes in *(top)* material parameters and *(bottom)* structure properties of the average control eye compared to the average glaucoma eye on the pressure-displacement curve at the scleral apex. Dashed lines represent the average experimental pressure-displacement response, and the shaded bands represent the one standard deviation experimental range. Solid lines represent the calculated pressure-displacement curve using the fitted parameters listed in Table 4.2. Shapes represent the model pressure-displacement response evaluated by varying the parameters one-by-one from the control eye values to the glaucoma eye values. L, W, T, are abbreviations for length, width, and thickness respectively.

range. There was large variation in the experimental data, and there is a large overlap between the control eye experiment range and the glaucoma eye experiment range. This overlap in experimental range contains the majority of the averaged experimental pressure-displacement responses, and therefore ascertaining if the effect of a parameter change is significant is difficult. A unpaired t-test comparing the strain at the maximum pressure of normal and glaucoma eyes, showed that the difference was not statistically significant (n=7, p=0.799).

Among all the parameters, the change in fiber crimp angle Θ_0 had the largest stiffening effect on the pressure-displacement response ($\Delta\mathbf{u}_{\max} = 0.835$). The change in fiber stiffness E had the next largest effect ($\Delta\mathbf{u}_{\max} = 0.450$), while the effect of changes in the fiber slenderness ratio β ($\Delta\mathbf{u}_{\max} = 0.018$) and matrix shear modulus μ ($\Delta\mathbf{u}_{\max} = 0.124$) were smaller.

We next examined the effects of changes in the structural features, i.e. collagen anisotropy, scleral thickness, and overall scleral geometry, on the pressure-displacement behavior at the scleral apex. Most notably, none of the structural changes induced a stiffer pressure-displacement response. In fact, the pressure-displacement curve calculated with the baseline material parameters and the average glaucoma scleral geometry resulted in a more compliant response ($\Delta\mathbf{u}_{\max} = -0.419$), as did the curve that just varied the scleral thickness ($\Delta\mathbf{u}_{\max} = -0.466$). This makes intuitive sense that a thinner scleral shell would result in a more compliant response. The change in collagen anisotropy near the ONH, made a negligible effect on the pressure-displacement response ($\Delta\mathbf{u}_{\max} = 0.00044$).

Alterations in fiber stiffness E and initial crimp angle Θ_0 had the largest contribution to the increased stiffness of the glaucoma mouse sclera. We varied these parameters to determine how much they have to change to increase the stiffness of the stress response to beyond experimental variation (Figure 4.7). The study used the FEM model and material

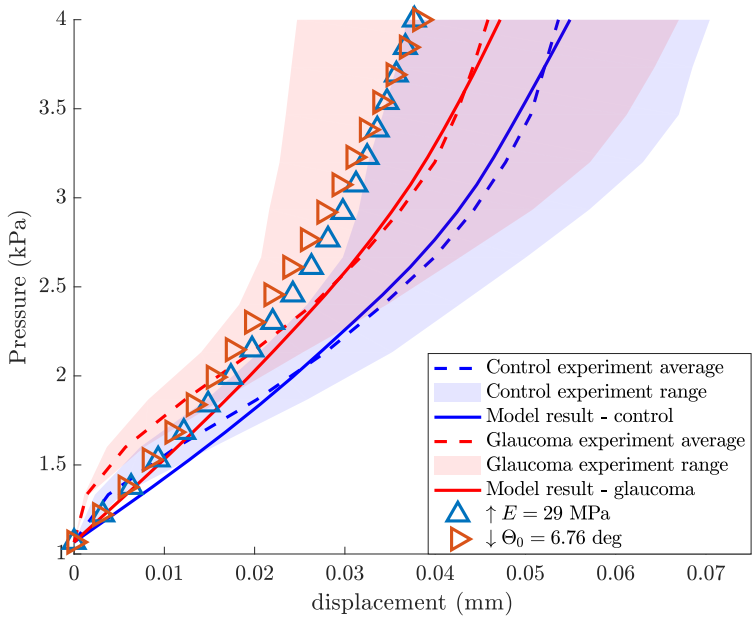

Figure 4.7: Effect of changes in fiber stiffness and fiber crimp angle of the average control eye compared to the average glaucoma eye on the pressure-displacement curve at the scleral apex. Dashed lines represent the average experimental pressure-displacement response, and the shaded bands represent the one standard deviation experimental range. Solid lines represent the calculated pressure-displacement curve using the fitted parameters listed in Table 4.2. Shapes represent the model pressure-displacement response evaluated by varying the parameters from the fitted control parameters. Changing the parameter $E = 29$ MPa or the parameter $\Theta_0 = 6.79°$, is sufficient to alter the model pressure-displacement response to shift it out of the control eye experimental range.

properties for the normal mouse sclera. Assuming all other parameters remain constant, the collagen fiber stiffness has to exceed 29 MPa, over a four-fold increase in the fiber stiffness determined by inverse FEA for the normal mouse eye. The reported scleral collagen fiber stiffness from other modeling efforts span a wide range from 5 MPa to more than 76 MPa in humans [38, 67] and tree shrews [64]. A collagen fiber stiffness of 29 MPa lies well within that range, however Coudrillier et al. [38] only estimated a 12% change in fiber stiffness in normal human posterior sclera and glaucoma human posterior sclera. The wide range in reported scleral collagen fiber stiffness may be from the different modeling methodologies, and a four-fold increase in collagen fiber stiffness from glaucoma may not be likely. To sufficiently alter the pressure-displacement curve to shift it out of the control eye experimental range, the crimp angle has to decrease to $\Theta_0 = 6.76°$, less than half of the fitted control eye parameter value, holding all other parameters constant. With such a small crimp angle, there is almost no bending contribution, and the pressure-displacement curve is almost linear, which is supported by the experimental measures [110].

4.5 Conclusion

We applied a micromechanical model in an inverse finite element analysis to estimate the changes in material properties from bead-injected glaucoma in the posterior sclera of CD1 mice. Nguyen et al. [110] conducted inflation tests of the mouse eyes which used DIC to track the motion of the scleral edge imaged in profile. The model was fit to the measured scleral edge displacements, and used the WAXS measurements of the collagen anisotropy [120] to describe the probability density distribution of fiber orientation in the peripapillary sclera. The model parameters describe the collagen fiber stiffness, initial crimp ratio, slenderness ratio, and the matrix shear modulus. A set of material parameters was determined for the average CD1 control mouse eye and another set of material parameters was determined for

the average CD1 glaucoma mouse eye. A parameter study was then conducted to evaluate the effects of changes in the material properties and structural features induced by experimental glaucoma.

The main findings of this work are:

1. A chronic increase in IOP increased the effective fiber stiffness, decreased the initial crimp angle, increased the fiber slenderness ratio and matrix shear of the posterior mouse sclera.

2. Of these material property changes, the change in initial crimp angle contributed the most to the stiffened pressure-displacement response, followed by the change in fiber stiffness

3. None of the experimentally measured structural changes, i.e. changes in scleral geometry and collagen reorientation, stiffened pressure-strain response at the scleral apex, and some structural changes made the pressure-strain response more compliant.

These findings suggest that the stiffening effect observed in the sclera from glaucoma were caused by changes to the collagen crimp morphology and fiber stiffness, rather than structural changes. The increase in the fiber stiffness parameter may be a reflection of an increase in collagen crosslinks [158, 82]. Collagen cross-links increase with age [60, 40], and may be associated with glaucoma. Kimball et al. [82] found that experimentally cross-linked CD1 mice eyes had a stiffer pressure-strain response and greater RGC axon loss than control or buffer-treated mice eyes at elevated IOP levels. This suggests that remodeling changes to the collagen fiber properties and collagen cross-linking may be an important contribution to the progression of glaucoma damage.

This study relies on a number of approximations and assumptions. First, the scleral geometry and edge displacements for each of the experimental groups were inferred from

averaging over 7 eyes. A more accurate approach would be to develop specimen-specific meshes, based on each eye's individual geometry, and fit a set of material parameters to each eye's individually measured displacements. To fit the material parameters, the parameter space was mapped to find a global minima. Because of computational expense, the parameter space was small. However this does not affect the findings of this work which examined the relative change in material properties and structural features on the pressure-displacement response.

We assumed that the material properties (i.e. collagen fiber stiffness, fiber crimp angle, fiber slenderness ratio, and matrix shear modulus) were uniform across the entire sclera. However, collagen diameter has been shown to vary across the sclera from the peripapillary sclera to the mid-posterior and through the scleral thickness [131, 174]. Additionally, the collagen fibers were assumed to be oriented in the plane of the sclera, but interwoven lamellae have been observed to be crossing out of the scleral plane[119].

The finite elements were developed using experimental data from CD1 mouse groups of different ages. The inflation tests were performed on 4 month old CD1 mouse eyes. The WAXS measurements of collagen anisotropy used older, 9 month old CD1 mouse eyes. The collagen anisotropy and mechanical properties can change significantly with age. Coudrillier et al. [34] showed that fiber alignment significantly decreased with age in human sclera. Myers et al. [107] found a stiffer pressure-displacement response in 11 month old C57BL/6 mice sclera than 2 month old C57BL/6 mice.

Overall, we identified changes in collagen fiber material properties as a consequence of bead-injected glaucoma. Alterations in the curvature and thickness of the sclera associated with glaucoma did not contribute to the stiffening of the pressure-displacement curve. The estimated changes in fiber crimp angle and fiber stiffness had the greatest contribution in the observed stiffening behavior. Further study of the mechanisms behind the collagen

fiber property changes would be beneficial in determining if glaucoma causes fiber property changes or if the property changes help cause glaucoma.

Chapter 5

Conclusions and Future Work

5.1 Summary of findings

Chapter 2 developed a method to measure small deformations from inflation tests of human posterior sclera. It adapted a protocol used to degrade GAGs from porcine sclera for the study of human sclera. A previous study had shown that the digestion of GAGs using the enzyme ChABC from porcine posterior sclera induced structural and mechanical changes [105]. There was motivation to determine if GAG removal induced similar changes in the mechanical response of human eyes, as a study of human eyes would be more relevant to the understanding of the mechanics of glaucoma and myopia. To capture the smaller displacements of the human sclera, the experimental methods were changed to enhance the magnification and lighting. Furthermore, the circumferential and meridional strain calculations as well as the stress-strain curve analysis were improved to use fewer approximations and thereby minimize the influence of noise on the data. The inflation response of the sclera and the scleral thickness on the same eye were measured after incubation in a buffer alone, and after incubation in a buffer containing ChABC. Sclera after being treated with ChABC had a significantly larger low-pressure stiffness, larger high-pressure stiffness, larger hysteresis, and smaller scleral thickness compared to when they were incubated in buffer-only. The scleral thinning and change in mechanical response after GAG digestion may be explained by

the partial replacement of bound water with free water in the tissue, and/or microstructure rearrangements such as the fusion or thinning of collagen fibrils. However GAG digestion of posterior porcine sclera [105], and human myopic eyes with a lower GAG content [5], had more compliant mechanical response compared to normal eyes, instead of the overall stiffer mechanical response reported here. It is hypothesized that because the human myopic eyes and porcine eyes tested were much younger than the eyes tested in this chapter, that aging may have affected the microstructure of the sclera, specifically through the addition of non-enzymatic collagen crosslinks that inhibited the tissue-softening effects of GAG degradation. This may explain why the results in this chapter are consistent with the increased stiffness measured in human eyes with glaucoma [35, 62]. This chapter concludes that GAGs play a significant role in the structure and mechanical properties in the human posterior sclera, via their effects on collagen-collagen interaction and tissue hydration. These effects may be mitigated or changed with age as the microstructure of the sclera remodels.

Chapter 3 developed a micromechanical model for the anisotropic hyperelastic behavior with damage of collagen constructs to investigate the effects of cyclic loading on the collagen network properties. Numerous studies have measured changes in the collagen structure and mechanical properties of cellularized native and engineered tissues in response to cyclic mechanical loading [172, 157, 163]. However, a recent experimental study demonstrated that cyclic loading also caused significant stiffening and strengthening of acellular collagen constructs [156]. This model was used to determine whether the measured changes in the tissue-level properties can be attributed to changes in the anisotropic collagen structure or mechanical properties of the collagen fibrils. The model parameters describing the elastic properties, damage properties, and morphology of the fibril were fit to the stress-stretch response measured for the constructs subjected to different preconditioning strains and cycles. The results showed that the changes in the collagen anisotropy measured in experiments were

insufficient to explain the increase in the stiffness and strength of the collagen constructs with cyclic loading and that the increase in the strength of the collagen constructs may be attributed mainly to the increase in the effective stiffness of the fibrils. These findings suggest that mechanical loading can induce changes in the stiffness and failure properties of the collagen fibril network through passive chemomechanical processes in addition to active cellular processes.

In Chapter 4, the micromechanical model from Chapter 3 was used to characterize how structural and material property changes from glaucoma affect the pressure-displacement inflation response of mice sclera. Previous experimental studies have measured the inflation response [110, 108] and collagen fiber orientation distribution [120] of glaucoma and normal CD1 mouse eyes. An inverse finite element method was used to fit the micromechanical model parameters describing the fiber and matrix elastic properties and fibril morphology to the average measured scleral edge displacements of glaucoma and normal CD1 mouse eyes. The model was then extended to investigate the individual effects of the structural and mechanical properties changes from glaucoma on the pressure-displacement inflation response of mice sclera. The results showed that the changes in fiber material properties were responsible to the observed stiffening response, and simulated changes in scleral geometry, and collagen anisotropy did not result in a stiffer mechanical response.

This dissertation presents 3 case studies within the broader study of mechanochemistry of collagen network remodeling in the posterior sclera. The case studies showed instances where changes in ECM composition and properties of the collagen network altered the inflation response of the posterior sclera, and an instance where changes in mechanical load could significantly alter the collagen network properties in an acellular collagen construct.

The case studies showed that a variety of factors can contribute to an observed strain stiffening response at the tissue level: removal of GAGs, cyclic preconditioning, or patho-

logical changes. Attempts were made to understand the mechanisms behind the stiffening response by estimating the changes in the collagen network, such as the increase of the effective collagen fiber stiffness and the decrease of the fiber crimp. Additionally, we theorize collagen cross-linking may explain the observed stiffening response in both GAG degraded eyes and eyes subjected to chronic pressure elevation.

The scleral thickness was observed to decrease in human eyes after GAG degradation and in mouse eyes that were subjected to chronic pressure elevation to induce glaucoma axon damage. A decrease in thickness increases the hoop stress in scleral shell, but a FEA simulation showed that (Figure 4.6) a thinner scleral shell results in a more compliant pressure-displacement response. Although the change in scleral thickness makes the pressure-displacement response more compliant, in both instances, it is outweighed by other factors that cause the sclera to stiffen, such as changes in the collagen network material properties, composition, and morphology.

This dissertation, through these case studies, sheds some light on the multi-scale implications of remodeling in the sclera. It examines how remodeling can be caused by changes in the mechanical environment, which in turn can cause pathological effects. It shows how remodeling affects the mechanical properties and structural features of the sclera, and demonstrates how changes in the collagen network can affect tissue-level responses.

5.2 Key contributions

This work contributes 4 key contributions to the field of scleral biomechanics

1. **The demonstration that GAGs play a measurable mechanical and structural role in the human posterior sclera, via their effect on tissue hydration and interactions with collagen fibrils.** The removal of GAGs induced an overall stiffening effect on the mechanical response of the posterior human sclera. The findings

suggest that the effect of GAG degradation is dependent on age and could be involved in the mechanical alterations observed in glaucoma.

2. **The finding that cyclic loading significantly increased the effective stiffness and altered the morphology of collagen fibrils in acellular collagen constructs.** The variation in these properties between experimental groups were greater than that caused by variations in the anisotropic fibril structure measured within the groups. The results suggest that mechanical loading can induce changes in collagen fibril network properties through passive chemomechanical processes.

3. **The development of a micromechanical model for the anisotropic hyperelastic behavior with damage**. Hierarchal micromechanical models help describe tissue-level behavior at fiber-level processes. In this work, a micromechanical model for collagen fibers developed by Cominou and Yannas [28] and Tonge et al. [161] was expanded to include fibril damage beyond a threshold strain. This model was implemented in an open-source finite element program, Tahoe (Sandia National Labs, Livermore, CA) [1] to determine the scleral collagen fibril-level changes from glaucoma in mice.

4. **The finding that changes in collagen fiber material properties are responsible for the observed stiffening effect in glaucoma mouse eyes.** The observed changes in structural features associated with glaucoma did not meaningfully stiffen the mechanical response.

[1] http://sourceforge.net/projects/tahoe/

5.3 Future Directions

Future directions include examining active versus passive remodeling processes, improving the micromechanical model discussed in this work, a more through investigation in the scleral microstructural changes in response to mechanical perturbations, and applying the methodologies developed in this thesis to other systems.

This dissertation examined remodeling under active processes, where mice eyes were exposed to chronic pressure elevation over a 6 week period *in-vivo*, and under passive processes where an acellular collagen construct was cyclically loaded. In the latter, we showed that remodeling can occur through passive chemomechanical processes. It would be interesting to study the contribution of passive remodeling processes versus active remodeling processes from chronic pressure elevation in the sclera. To help determine the passive contribution, collagen constructs could be inflated to comparable pressures as those found in normal and glaucoma mouse eyes, and held for an extended period of time. The change in collagen fiber orientation and long-term creep response could be evaluated.

Another focus of future work is to evaluate the microstructural changes with remodeling. In this work, we demonstrated that small changes in the fibril crimp make a large difference in the mechanical response. The crimp angle parameter reported throughout this work is determined from an inverse finite element analysis model to represent the nonlinear stress response, and is not a direct measurement of the microstructure. However, this could be experimentally validated by observing the change in fibril crimp in glaucoma and normal eyes, or before and after cyclic loading, using second harmonic generation imaging [68] or magnetic resonance imaging (MRI) [72]. Fibril-fibril interaction, specifically cross-linking, should also be investigated. Age-related changes in scleral collagen cross-linking may affect GAG degradation and increased scleral cross-linking has been shown to increase the susceptibility of RGC damage [82]. Experimentally, the mechanical response of GAG degradation

can be compared between normal sclera and sclera treated with a cross-linking agent.

Cross-linking can also be incorporated to the micromechanical model. Early attempts at modeling cross-linking have included representing fibril-fibril and fibril-matrix interaction as a statistical ensemble [144], modeling the force balance at fibril-fibril intersections [24], or adapting non-affine models from polymer physics [97]. Incorporation of a cross-linking scheme into the micromechanical model will enable the model to be used to help determine if glaucoma accelerates collagen cross-linking in the sclera. This would also be useful for other applications, such as evaluating the effectiveness of crosslinking treatments for corneal ectasia, or determining age-related changes in the skin.

This work only considers remodeling, and does not incorporate growth mechanisms such as collagen degradation or deposition. Previous works have incorporated collagen degradation and deposition [161, 78] into the micromechanical model discussed in this work. It would be useful to implement these features into a finite element program, to investigate how homeostasis is achieved in sclera in response to a pressure perturbation. This would be helpful in understanding why some eyes with elevated IOP do not develop glaucoma, or why some eyes develop glaucoma at "normal" IOP levels [125].

The micromechanical model can be further improved by incorporating poroelastic and electrostatic features. Such a model would be useful in evaluating the tissue swelling and hydration effects of GAG degradation. While poroelastic-multiphasic [84, 170] and electrostatic models [20, 79] have been developed to describe GAGs, none include the effects of GAG-collagen interaction. Viscoelastic models have been developed to describe the interactions between GAGs and collagen [27, 154] but are phenomenological.

The finite element model was used in this work to simulate the entire posterior sclera, however it would be of great interest to focus on the peripapillary sclera, and use a more anatomically detailed mesh to study how changes in the structure and mechanical properties

affect the stresses exerted on the nearby lamina cribrosa. The model can also be used to study myopia, where remodeling processes axially elongate the eye, thin the scleral shell, and alter the collagen fibril diameter and alignment [91, 138]. Myopic eyes also demonstrate a more compliant load response [117]. In this work, we tangentially showed that a thinner scleral shell and axial elongation resulted in a more compliant mechanical response. It would interesting to determine how much the structural changes associated with myopia contribute to the observed mechanical behavior.

Finally, the model can be applied to other tissue systems and applications, such as wound healing and scar formation in the skin. Scarring is associated with a change in resistance to failure, change in collagen anisotropy, and morphology [32, 173]. The model could be used to study how scars affect the skin's ability to bear load. Another application where the model can be used is to investigate the mechanical durability of engineered tissues. For example, bioprosthetic heart valves often only have a lifespan of 10-15 years, and primarily fail because of structural damage [176]. The model can be used to help determine how changes in the valve structure, microstructure, and material properties cause stress concentrations, which lead to structural damage.

Appendix A

Experimental details for Chapter 2

A.1 Inflation test: Experimental protocol

A.1.1 Equipment List

- **Honeywell TJE pressure transducer**
  - P/N 068-075C-03TJG, 2 psig range, 0.1% full scale accuracy, data converted from analog to digital and written to a log file.
- **MTS driven pump system:**
  - MTS driven syringe pump: MTS Insight 5, 0.01 mm position accuracy, 1 kN load cell, 1.535 mV/V sensitivity.
  - Syringes: Plunger of a 60 cc plastic syringe attached to MTS crosshead, syringe encased in aluminum and mounted on the base of the MTS machine.
  - Saline: Dulbecco's Phosphate Buffered Saline (DPBS) without calcium or magnesium (BioWhittaker, Catalog No. 17-512F)
- **Camera setup**
  - Cameras: Point Grey GRAS-20S4M/C, with 1/1.8" image sensors

  - Lenses: Edmund Optics, NT59-870, 16 mm focal length, f/8 aperture
  - 5mm Length, C-Mount extension tube

- **Digital Image Correlation system**
  - Calibration grid: 1" calibration grid (Correlated Solutions, #055893)
  - Software: VicSnap 2011 & Vic3D 2009 by Correlated Solutions

- **Speckling system**
  - Compressor: Iwata Medea, Smart Jet model
  - Airbrush: Iwata Medea, Eclipse HP-CS model, 0.35-mm needle and nozzle combination
  - Ink: Higgans black magic, semi-flat finish, waterproof, and acid-free, part 44011

- **Lighting**
  - Ring light (Commercial Electric 2700 K T9 Circline CFL Light bulb)

- **Inflation chamber**
  - Inflation chamber, custom made, designed by Professor Kristin Myers
  - Scleral holder: Custom made from acrylic to fit scleral specimen. Used holders 2a and 2b described in Murienne 2016 [103].

A.1.2 Inflation Test Procedure

1. Receive donor globes from NDRI
2. Measure axial length and width with calipers, mark nasal side of the sclera

3. Remove extraocular fat and muscles

4. Glue to custom-made scleral holder with cyanoacrylate, with the hole centered around the ONH. Let dry 5 minutes

5. Remove anterior sclera, and intraocular structures (lens, iris, vitreous humor, choroid, and retina)

6. Incubate posterior sclera in buffer solution or buffer solution with ChABC

7. Speckle sclera with India Ink

8. Position main chamber of the inflation chamber underneath cameras, secure to optical table, and connect to pressure transducer

9. Tare pressure on TestWorks and reset the motor on the MTS

10. Open release valve in pressure transducer, and fill MTS pump system with DPBS saline solution. When the release valve releases a steady stream of saline (all air bubbles disappeared), close the valve, and let the saline solution fill up the main chamber

11. Fit the rubber O-ring to seal along the groove along the inner diameter of the main chamber of inflation chamber.

12. Align the sample fixture to the red markings on the main chamber (along the nasal-temporal and superior-inferior directions).

13. Tightly screw in the top ring of the inflation chamber. If the pressure reading does not increase, then there may be a leak in the system. Do not proceed.

14. Place humidity chamber around the setup with moist filters inside to prevent tissue dehydration.

15. Open release valve on the connector of the pressure transducer and pour in more saline solution to the pump system. Close valve when there are no longer air bubbles.

16. Using the manual control for the MTS system, lower the plunger head into the pump system. If the pressure is too high, open the valve until the pressure comes back down to the appropriate baseline pressure (0.03 psi for human).

17. Let specimen equilibrate at the baseline pressure (method in TestWorks).

18. Calibrate cameras, and adjust focus

19. Start inflation test

A.2 Donor Information

Eye ID	Sex	Age (yr)	Race	Eye
FC72-OD	F	72	Caucasian	R
FC72-OS	F	72	Caucasian	L
MC75-OD	M	75	Caucasian	R
MC75-OS	M	75	Caucasian	L
MC84-OS	M	84	Caucasian	L
FC80-OD	F	80	Caucasian	R
FC80-OS	F	80	Caucasian	L
FC49-OD*	F	49	Caucasian	L
MC57-OD	M	57	Caucasian	R
MC57-OS	M	57	Caucasian	L

Table A.1: List of human donor eyes in order of date. Asterisked eye denotes eye used for s-GAG quantification and hydration testing. All other eyes subjected to inflation testing.

Appendix B

Additional Figures for Chapter 3

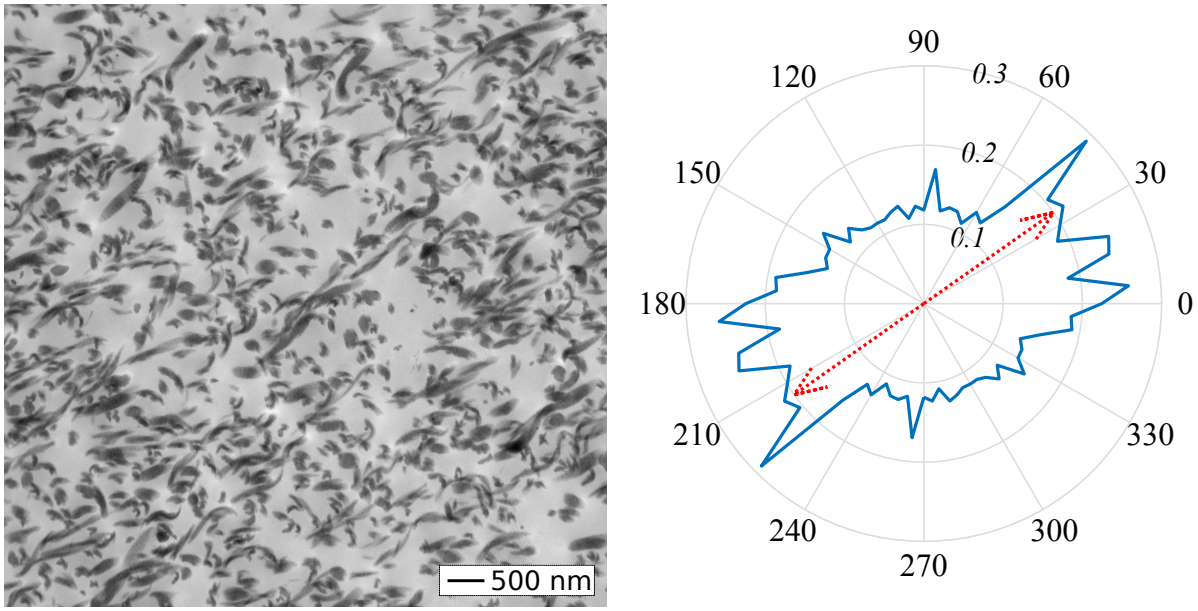

Figure B.1: *(left)* A sample TEM image of the DDCS section. *(right)* The normalized fibril orientation histogram of the TEM image with angular resolution of 5°; the red dotted line denotes the loading direction of the sample. The fibril orientation probability density distribution is formed by aggregating the histograms for all the images taken for that sample, correcting for the loading direction and normalizing the result. Image courtesy of Monica Susilo.

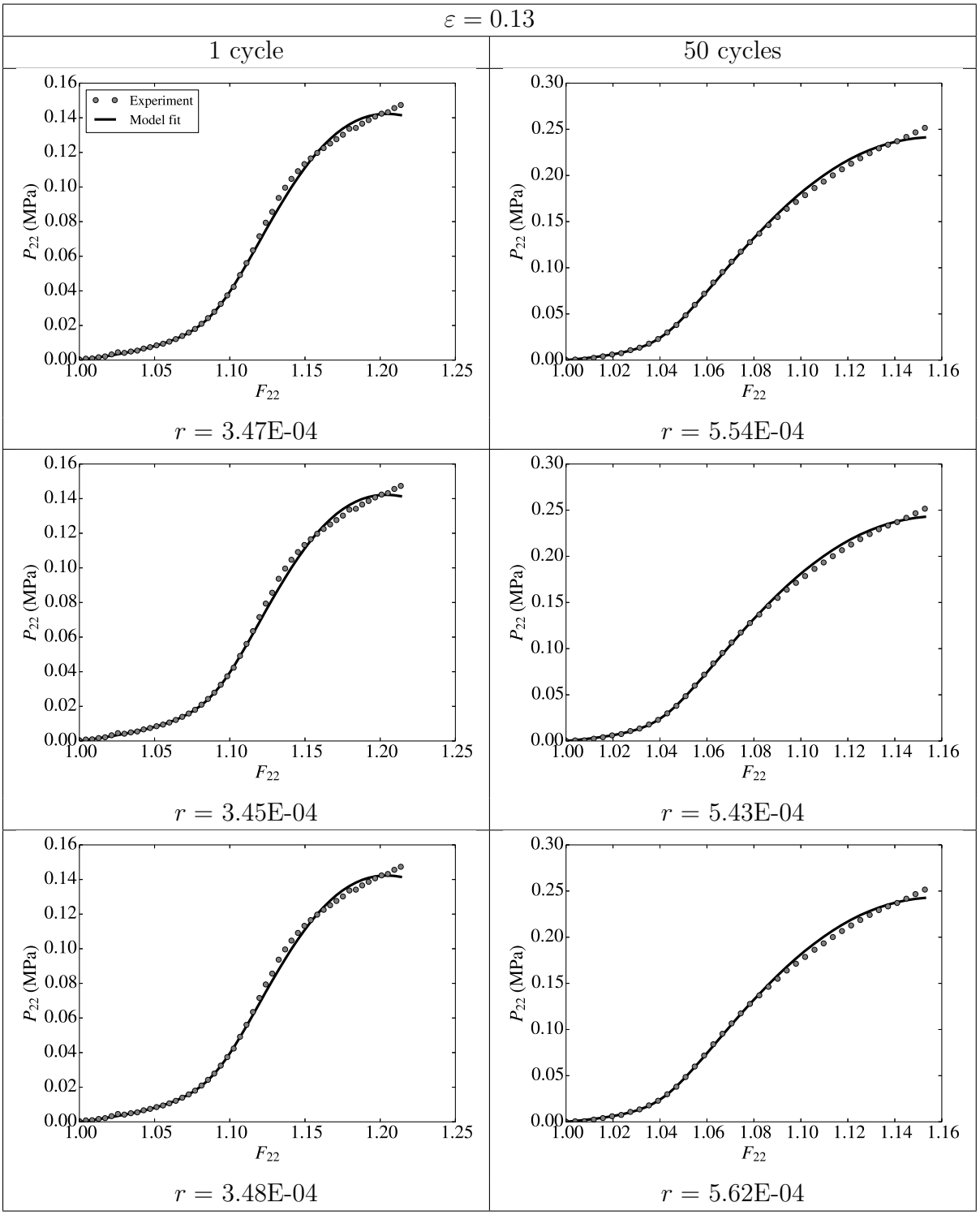

Figure B.2: Model fits of individual fibril distribution load-to-failure experimental stress-stretch curve for $\varepsilon = 0.13$, with cost function r as defined in section 3.3.3. Model plots correspond to the fitted parameters in Table 3.2

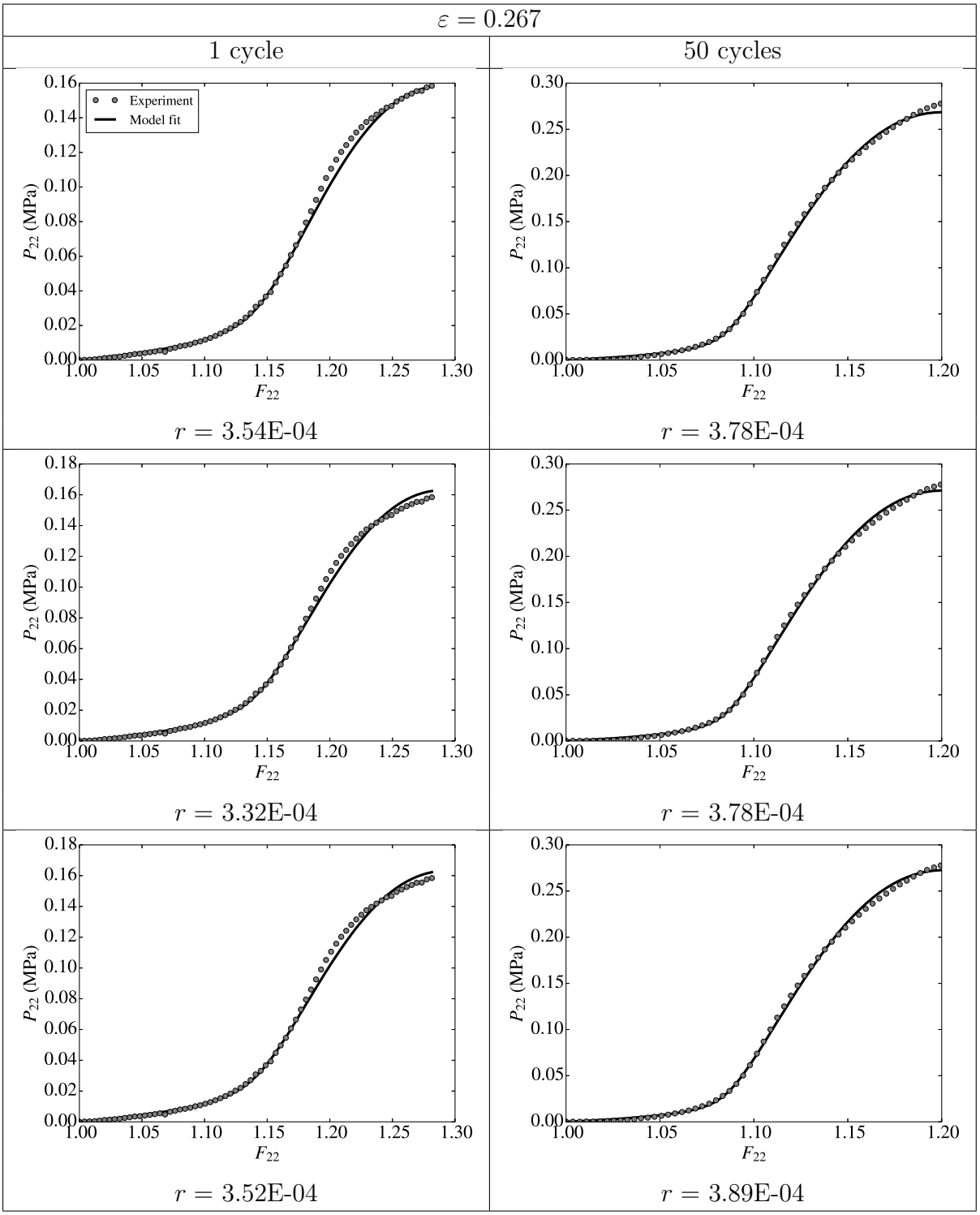

Figure B.3: Model fits of individual fibril distribution load-to-failure experimental stress-stretch curve for $\varepsilon = 0.267$, with cost function r as defined in section 3.3.3. Model plots correspond to the fitted parameters in Table 3.2

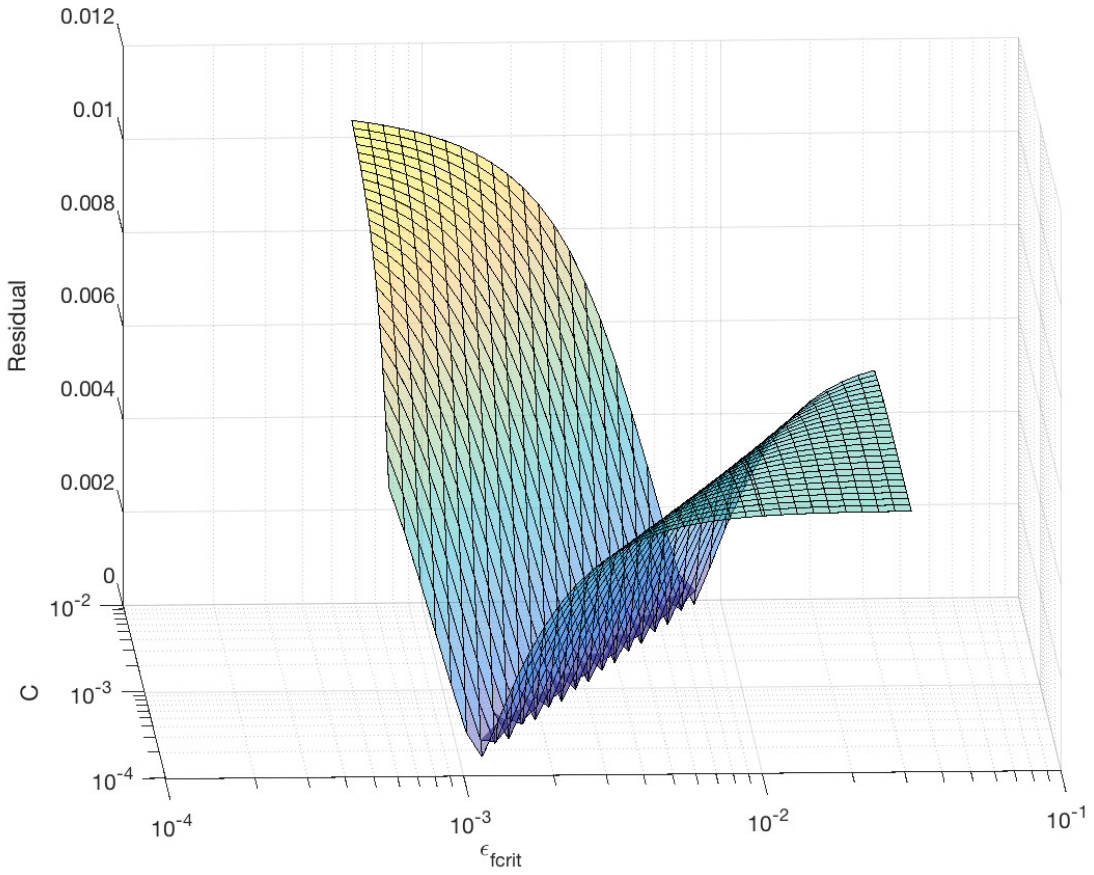

Figure B.4: Contour map of the cost function as a function of varying $\varepsilon_{f\text{crit}}$ and C for a $\varepsilon = 0.13$, 1 cycle fibril distribution. There was a combination of damage parameters, $\frac{C}{\varepsilon_{f\text{crit}}^2}$, that produced a similar error norm.

Bibliography

[1] Alberts, B., Johnson, A., Lewis, J., Raff, M., Roberts, K., and Wlater, P. *Molecular Biology of the Cell*. Garland Publishing Inc., New York, 4th edition, 2002.

[2] Anderson, D. R. and Hendrickson, A. Effect of intraocular pressure on rapid axoplasmic transport in monkey optic nerve. *Investigative Ophthalmology & Visual Science*, 13: 771–783, 1974.

[3] Atchison, D. A., Jones, C. E., Schmid, K. L., Pritchard, N., Pope, J. M., Strugnell, W. E., and Riley, R. A. Eye shape in emmetropia and myopia. *Investigative Ophthalmology & Visual Science*, 45(10):3380–3386, 2004.

[4] Avetisov, E. S., Savitskaya, N. F., Vinetskaya, M. I., and Iomdina, E. N. A study of biochemical and biomechanical qualities of normal and myopic eye sclera in humans of different age groups. *Metabolic, Pediatric, and Systemic Ophthalmology*, 7(4):183–188, 1982.

[5] Avetisov, E., Savitskaya, N., Vinetskaya, M., and Iomdina, E. A study of biochemical and biomechanical qualities of normal and myopic eye sclera in humans of different age groups. *Metabolic, pediatric, and systemic ophthalmology*, 7(4):183–188, 1983.

[6] Ayad, S., Boot-Handford, R., Humphries, M. J., Kadler, K. E., and Shuttleworth, A. *The Extracellular Matrix Factsbook, 2nd {E}dition*. Factsbook series. Academic Press, London, 1994. ISBN 9780120689101.

[7] Aziz, J., Shezali, H., Radzi, Z., Yahya, N. A., Hayaty, N., Kassim, A., Czernuszka, J., and Rahman, M. T. Molecular Mechanisms of Stress-Responsive Changes in Collagen and Elastin Networks in Skin. *Skin Pharmacology and Physiology*, 29(4):190–203, 2016. doi: 10.1159/000447017.

[8] Bailey, A. Structure , Function and Ageing of the Collagens of the Eye. *Nature Publishing Group*, 1(2):175–183, 1987. ISSN 0950-222X. doi: 10.1038/eye.1987.34. URL `http://dx.doi.org/10.1038/eye.1987.34`.

[9] Barraglioli, J. L. and Kamm, R. D. Measurements of the Compressive Properties of Sclerol Tissue. *Investigative Ophthalmology & Visual Science*, 25(1):59–65, 1984.

[10] Bekerman, I., Gottlieb, P., and Vaiman, M. Variations in Eyeball Diameters of the Healthy Adults. *Journal of Opthamology*, 2014, 2014.

[11] Bengtsson, B. The prevalence of glaucoma. *British Journal of Ophthalmology*, 65(1): 46–49, 1981.

[12] Bettelheim, F. A. and Plessy, B. The hydration of proteoglycans of bovine cornea. *Biochimica et Biophysica Acta (BBA)-General Subjects*, 381(1):203–214, 1975.

[13] Bhole, A. P., Flynn, B. P., Liles, M., Saeidi, N., Dimarzio, C. A., and Ruberti, J. W. Mechanical strain enhances survivability of collagen micronetworks in the presence of collagenase: implications for load-bearing matrix growth and stability. *Philosophical Transactions of the Royal Society A: Mathematical, Physical and Engineering Sciences*, 367(1902):3339–3362, 2009. ISSN 1364-503X. doi: 10.1098/rsta.2009.0093. URL `http://rsta.royalsocietypublishing.org/cgi/doi/10.1098/rsta.2009.0093`.

[14] Boote, C., Hayes, S., Abahussin, M., and Meek, K. M. Mapping Collagen Organization

in the Human Cornea : Left and Right Eyes Are Structurally Distinct. *Investigative Ophthalmology & Visual Science*, 47(3):901–908, 2005. doi: 10.1167/iovs.05-0893.

[15] Borcherding, M. S., Blacik, L. J., Sittig, R. A., Bizzell, J. W., Breen, M., and Weinstein, H. G. Proteoglycans and collagen fibre organization in human corneoscleral tissue. *Experimental Eye Research*, 21(1):59–70, 1975.

[16] Boubriak, O., Urban, J., and Bron, A. Differential effects of aging on transport properties of anterior and posterior human sclera. *Experimental Eye Research*, 76(6):701–713, 2003. doi: 10.1016/S0014-4835(03)00053-8.

[17] Breen, M., Johnson, R. L., Sittig, R. A., Weinstein, H. G., and Veis, A. The acidic glycosaminoglycans in human fetal development and adult life: Cornea, sclera and skin. *Connective Tissue Research*, 1(4):291–303, 1972.

[18] Buehler, M. J. Nature designs tough collagen : Explaining the nanostructure of collagen fibrils. *Proceedings of the National Academy of Sciences of the United States of America*, 103(33), 2006.

[19] Burgoyne, C. F., Downs, J. C., Bellezza, A. J., Suh, J. F., and Hart, R. T. The optic nerve head as a biomechanical structure : a new paradigm for understanding the role of IOP-related stress and strain in the pathophysiology of glaucomatous optic nerve head damage. *Progress in Retinal and Eye Research*, 24(1):39–73, 2005. doi: 10.1016/j.preteyeres.2004.06.001.

[20] Buschmann, M. and Grodzinsky, A. A molecular model of proteoglycan-associated electrostatic forces in cartilage mechanics. *Journal of Biomechanical Engineering*, 117 (2):179–192, 1995.

[21] Campbell, I. C., Coudrillier, B., and Ethier, C. R. Biomechanics of the Posterior Eye : A Critical Role in Health and Disease. *Journal of Biomechanical Engineering*, 136 (2), 2014. doi: 10.1115/1.4026286.

[22] Caprioli, J. and Coleman, A. L. Intraocular Pressure Fluctuation: A Risk Factor for Visual Field Progression at Low Intraocular Pressures in the Advanced Glaucoma Intervention Study. *Ophthalmology*, 115(7):1123–1129, 2008. doi: 10.1016/j.ophtha.2007.10.031.

[23] Celorio, J. and Pruett, R. C. Prevalence of lattice degeneration and its relation to axial length in severe myopia. *American Journal of Ophthalmology*, 111(1):20–23, 1991.

[24] Chandran, P. L. and Barocas, V. H. Affine Versus Non-Affine Fibril Kinematics in Collagen Networks : Behavior. *Journal of Biomechanical Engineering*, 128(2):259–270, 2006. doi: 10.1115/1.2165699.

[25] Chen, K., Rowley, A. P., Weiland, J. D., and Humayun, M. S. Elastic properties of human posterior eye. *Journal of Biomedical Materials Research, Part A*, 102(6): 2001–2007, 2013. doi: 10.1002/jbm.a.34858.

[26] Chen, M. L., Ruberti, W., and Nguyen, T. D. Increased stiffness of collagen fibrils following cyclic tensile loading. *Journal of the Mechanical Behavior of Biomedical Materials*, 82:345–354, 2018. doi: 10.1016/j.jmbbm.2018.03.027.

[27] Ciarletta, P., Amar, M. B., and Supe, N. A finite dissipative theory of temporary interf ibrillar bridges in the extracellular matrix of ligaments and tendons. *Journal of The Royal Society Interface*, 6(39):909–924, 2008. doi: 10.1098/rsif.2008.0487.

[28] Comninou, M. and Yannas, I. Dependence of stress-strain nonlinearity of connective

tissues on the geometry of collagen fibres. *Journal of Biomechanics*, 9:427–433, 1976. doi: 10.1016/0021-9290(76)90084-1.

[29] Comper, W. D. and Laurent, T. C. Physiological function of connective tissue polysaccharides. *Physiological Reviews*, 58(1):255–315, 1978.

[30] Cone, F. E., Steinhart, M. R., Oglesby, E. N., Kalesnykas, G., Pease, M. E., and Quigley, H. A. The effects of anesthesia, mouse strain and age on intraocular pressure and an improved murine model of 59. experimental glaucoma. *Experimental Eye Research*, 99(1):27–35, 2012. doi: 10.1016/j.exer.2012.04.006.The.

[31] Cone-Kimball, E., Nguyen, C., Oglesby, E. N., Pease, M. E., Steinhart, M. R., and Quigley, H. A. Scleral structural alterations associated with chronic experimental intraocular pressure elevation in mice. *Molecular Vision*, 19:2023, 2013.

[32] Corr, D. T. and Hart, D. A. Biomechanics of scar tissue and uninjured skin biomechanics of scar tissue and uninjured skin. *Advances in wound care*, 2(2), 2013.

[33] Corsi, A., Xu, T., Chen, X.-D., Boyde, A., Liang, J., Mankani, M., Sommer, B., Iozzo, R. V., Eichstetter, I., Robey, P. G., and Others. Phenotypic effects of biglycan deficiency are linked to collagen fibril abnormalities, are synergized by decorin deficiency, and mimic {E}hlers{-D}anlos-like changes in bone and other connective tissues. *Journal of Bone and Mineral Research*, 17(7):1180–1189, 2002.

[34] Coudrillier, B. *Age and glaucoma related changes in the mechanical properties and collagen structure of the human posterior sclera*. PhD thesis, 2013.

[35] Coudrillier, B., Tian, J., Alexander, S., Myers, K. M., Quigley, H. A., and Nguyen, T. D. Biomechanics of the Human Posterior Sclera: Age- and Glaucoma-Related

Changes Measured Using Inflation Testing. *Investigative Ophthalmology & Visual Science*, 53(4):1714–1728, 2012. doi: 10.1167/iovs.11-8009.

[36] Coudrillier, B., Tian, J., Alexander, S., Myers, K. M., Quigley, H. A., and Nguyen, T. D. Biomechanics of the human posterior sclera: {A}ge-and glaucoma-related changes measured using inflation testing. *Investigative Ophthalmology & Visual Science*, 53(4):1714–1728, 2012.

[37] Coudrillier, B., Boote, C., Quigley, H. A., and Nguyen, T. D. Scleral anisotropy and its effects on the mechanical response of the optic nerve head. *Biomechanics and Modeling in Mechanobiology*, 12(5):941–963, 2013. doi: 10.1007/s10237-012-0455-y.Scleral.

[38] Coudrillier, B., Pijanka, J. K., Jefferys, J. L., Goel, A., Quigley, H. A., Boote, C., and Nguyen, T. D. Glaucoma-related Changes in the Mechanical Properties and Collagen Micro-architecture of the Human Sclera. *PLoS ONE*, 10(7):1–14, 2015.

[39] Cui, W., Bryant, M. R., Sweet, P. M., and Mcdonnell, P. J. Changes in gene expression in response to mechanical strain in human scleral fibroblasts. *Experimental eye research*, 78:275–284, 2004. doi: 10.1016/j.exer.2003.10.007.

[40] Curtin, B. J. Physiopathologic aspects of scleral stress-strain. *Transactions of the American Ophthalmological Society*, 67:417–61, 1969.

[41] Curtin, B. J., Iwamoto, T., and Renaldo, D. P. Normal and staphylomatous sclera of high myopia: {A}n electron microscopic study. *Archives of Ophthalmology*, 97(5): 912–915, 1979.

[42] Danielson, K. G., Baribault, H., Holmes, D. F., Graham, H., Kadler, K. E., and Iozzo, R. V. Targeted disruption of decorin leads to abnormal collagen fibril morphology and skin fragility. *The Journal of Cell Biology*, 136(3):729–743, 1997.

[43] Downs, J. C., Ensor, M. E., Bellezza, A. J., Thompson, H. W., Hart, R. T., and Burgoyne, C. F. Posterior Scleral Thickness in Perfusion-Fixed Normal and Early-Glaucoma Monkey Eyes. *Investigative Ophthalmology and Visual Science*, 42(13):3202–3208, 2001.

[44] Downs, J. C., Suh, J.-k. F., Thomas, K. A., Bellezza, A. J., Hart, R. T., and Burgoyne, C. F. Viscoelastic Material Properties of the Peripapillary Sclera in Normal and Early-Glaucoma Monkey Eyes AND. *Invest Ophthalmology Vis Sci.*, 46(2):540–546, 2005. doi: 10.1167/iovs.04-0114.

[45] Eilaghi, A., Flanagan, J. G., Tertinegg, I., Simmons, C. A., Brodland, G. W., and Ethier, C. R. Biaxial mechanical testing of human sclera. *Journal of Biomechanics*, 43(9):1696–1701, 2010. ISSN 0021-9290. doi: 10.1016/j.jbiomech.2010.02.031. URL `http://dx.doi.org/10.1016/j.jbiomech.2010.02.031`.

[46] Elliott, G. F., Goodfellow, J. M., and Woolgar, A. E. Swelling studies of bovine corneal stroma without bounding membranes. *The Journal of Physiology*, 298(1):453–470, 1980.

[47] Elliott, G. F. and Hodson, S. A. Cornea, and the swelling of polyelectrolyte gels of biological interest. *Reports on Progress in Physics*, 61(10):1325–1365, 1998.

[48] Elsheikh, A., Geraghty, B., Alhasso, D., Knappett, J., Campanelli, M., and Rama, P. Regional variation in the biomechanical properties of the human sclera. *Experimental Eye Research*, 90(5):624–633, 2010. ISSN 0014-4835. doi: 10.1016/j.exer.2010.02.010. URL `http://dx.doi.org/10.1016/j.exer.2010.02.010`.

[49] Ethier, C. R. and Simmons, C. A. *Introductory biomechanics: from cells to organisms*. Cambridge University Press, 2007. ISBN 9780521841122.

[50] Fechtner, R. D. and Weinreb, R. N. Mechanisms of optic nerve damage in primary open angle glaucoma. *Survey of Ophthalmology*, 39(1):23–42, 1994.

[51] Flynn, B. P., Bhole, A. P., Saeidi, N., Liles, M., Dimarzio, C. A., and Ruberti, J. W. Mechanical strain stabilizes reconstituted collagen fibrils against enzymatic degradation by mammalian collagenase matrix metalloproteinase 8 (MMP-8). *PLoS ONE*, 5 (8):21–23, 2010. ISSN 19326203. doi: 10.1371/journal.pone.0012337.

[52] Flynn, B. P., Tilburey, G. E., and Ruberti, J. W. Highly sensitive single-fibril erosion assay demonstrates mechanochemical switch in native collagen fibrils. *Biomechanics and Modeling in Mechanobiology*, 12(2):291–300, 2013. ISSN 16177959. doi: 10.1007/s10237-012-0399-2.

[53] Foolen, J., Van Donkelaar, C. C., Soekhradj-Soechit, S., and Ito, K. European Society of Biomechanics S.M. Perren Award 2010: An adaptation mechanism for fibrous tissue to sustained shortening. *Journal of Biomechanics*, 43(16):3168–3176, 2010. ISSN 00219290. doi: 10.1016/j.jbiomech.2010.07.040.

[54] Freed, A. D. and Doehring, T. C. Elastic Model for Crimped Collagen Fibrils. *Journal of Biomechanical Engineering*, 27(4):587–593, 2005. doi: 10.1115/1.1934145.

[55] Fujikura, H., Seko, Y., Tokoro, T., Mochizuki, M., and Shimokawa, H. Involvement of Mechanical Stretch in the Gelatinolytic Activity of the Fibrous Sclera of Chicks , In Vitro. *Japanese Journal of Ophthalmology*, 46(1):24–30, 2000.

[56] Fung, Y. Biorheology of soft tissues. *Biorheology*, 10(2):139 – 155, 1973.

[57] Garcia-Valenzuela, E., Shareef, S., Walsh, J., and Sharma, S. C. Programmed cell death of retinal ganglion cells during experimental glaucoma. *Experimental Eye Research*, 61(1):33–44, 1995.

[58] Gelman, S., Cone, F. E., Pease, M. E., Nguyen, T. D., Myers, K., and Quigley, H. A. The presence and distribution of elastin in the posterior and retrobulbar regions of the mouse eye. *Experimental eye research*, 90:210–215, 2010. doi: 10.1016/j.exer.2009.10.007.

[59] Genovese, K. A video-optical system for time-resolved whole-body measurement on vascular segments. *Optics and Lasers in Engineering*, 47(9):995–1008, 2009. ISSN 01438166. doi: 10.1016/j.optlaseng.2009.04.017. URL `http://dx.doi.org/10.1016/j.optlaseng.2009.04.017`.

[60] Girard, J. A., Suh, J. F., Bottlang, M., Burgoyne, C. F., and Downs, J. C. Scleral Biomechanics in the Aging Monkey Eye AND. *Investigative Ophthalmology & Visual Science*, 50(11):5226–5237, 2009. doi: 10.1167/iovs.08-3363.

[61] Girard, M. J. A., Downs, J. C., Bottlang, M., Burgoyne, C. F., and Suh, J.-K. F. Peripapillary and posterior scleral mechanics Part II: Experimental and inverse finite element characterization. *Journal of Biomechanical Engineering*, 131(5):51012, 2009.

[62] Girard, M. J. A., Suh, J.-K. F., Bottlang, M., Burgoyne, C. F., and Downs, J. C. Biomechanical changes in the sclera of monkey eyes exposed to chronic IOP elevations. *Investigative Ophthalmology & Visual Science*, 52(8):5656, 2011.

[63] Grytz, R. and Meschke, G. Constitutive modeling of crimped collagen fibrils in soft tissues. *Journal of the Mechanical Behavior of Biomedical Materials*, 2(5):522–533, 2009. ISSN 1751-6161. doi: 10.1016/j.jmbbm.2008.12.009. URL `http://dx.doi.org/10.1016/j.jmbbm.2008.12.009`.

[64] Grytz, R. and Siegwart Jr, J. T. Changing Material Properties of the Tree Shrew Sclera

During Minus Lens Compensation and Recovery. *Anatomy and Pathology/Oncology*, 56(3):2065–2078, 2015. doi: 10.1167/iovs.14-15352.

[65] Grytz, R., Meschke, G., and Jonas, J. B. The collagen fibril architecture in the lamina cribrosa and peripapillary sclera predicted by a computational remodeling approach. *Biomechanics and Modeling in Mechanobiology*, 10(3):371–382, 2011. doi: 10.1007/s10237-010-0240-8.

[66] Grytz, R., Sigal, I. A., Ruberti, J. W., Meschke, G., and Downs, J. C. Lamina cribrosa thickening in early glaucoma predicted by a microstructure motivated growth and remodeling approach. *Mechanics of Materials*, 44:99–109, 2012. ISSN 0167-6636. doi: 10.1016/j.mechmat.2011.07.004. URL `http://dx.doi.org/10.1016/j.mechmat.2011.07.004`.

[67] Grytz, R., Fazio, M. A., Girard, J. A., Libertiaux, V., Bruno, L., Gardiner, S., Girkin, C. A., and Downs, J. C. Material properties of the posterior human sclera. *Journal of the Mechanical Behavior of Biomedical Materials*, 29:602–617, 2014. doi: 10.1016/j.jmbbm.2013.03.027.

[68] Han, M., Gunter, G., and Bille, J. F. Second harmonic generation imaging of collagen fibrils in cornea and sclera. *Optics Express*, 13(15):5791–5797, 2005.

[69] Hedbom, E. and Heinegård, D. Binding of fibromodulin and decorin to separate sites on fibrillar collagens. *Journal of Biological Chemistry*, 268(36):27307–27312, 1993.

[70] Hedbys, B. O. The role of polysaccharides in corneal swelling. *Experimental Eye Research*, 1(1):81–91, 1961.

[71] Hernandez, M. R., Andrzejewska, W. M., and Neufeld, A. H. Changes in the Extracellular Matrix of the Human Optic Nerve Head in Primary Open-Angle Glau-

coma. *American Journal of Ophthalmology*, 109(2):180–188, 1990. ISSN 0002-9394. doi: 10.1016/S0002-9394(14)75984-7. URL `http://dx.doi.org/10.1016/S0002-9394(14)75984-7`.

[72] Ho, L. C., Sigal, I. A., Jan, N.-j., Squires, A., Tse, Z., Wu, E. X., Kim, S.-g., Schuman, J. S., and Chan, K. C. Magic Angle - Enhanced MRI of Fibrous Microstructures in Sclera and Cornea With and Without Intraocular Pressure Loading. *Investigative Ophthalmology & Visual Science*, 55(9):5662–72, 2014. doi: 10.1167/iovs.14-14561.

[73] Holzapfel, G. Biomechanics of soft tissue. In *The Handbook of Materials Behavior Models, vol 3*, pages 1049–1063. 2001.

[74] Huang, C. and Yannas, I. V. Mechanochemical studies of enzymatic degradation of insoluble collagen fibers. *Journal of Biomedical Materials Research*, 11(1):137–154, 1977. ISSN 10974636. doi: 10.1002/jbm.820110113.

[75] Huang, Y. and Meek, K. M. Swelling studies on the cornea and sclera: {T}he effects of p{H} and ionic strength. *Biophysical Journal*, 77(3):1655–1665, 1999.

[76] Huisman, E. M., Van Dillen, T., Onck, P. R., and Van Der Giessen, E. Three-dimensional cross-linked F-actin networks: Relation between network architecture and mechanical behavior. *Physical Review Letters*, 99(20), 2007. ISSN 00319007. doi: 10.1103/PhysRevLett.99.208103.

[77] Jan, N.-j., Brazile, B. L., Hu, D., Grube, G., Wallace, J., Gogola, A., and Sigal, I. A. Crimp around the globe; patterns of collagen crimp across the corneoscleral. *Experimental Eye Research*, 172:159–170, 2018.

[78] Jia, Z. and Nguyen, T. D. A micromechanical model for collagenous tissues under mechano-mediated collagen deposition and degradation. 2019.

[79] Jin, M. and Grodzinsky, A. J. Effect of Electrostatic Interactions between Glycosaminoglycans on the Shear Stiffness of Cartilage : A Molecular Model and Experiments. *Macromolecules*, 34(23):8330–8339, 2001. doi: 10.1021/ma0106604.

[80] Kanai, A. and Kaufman, H. E. Electron microscopic studies of the elastic fiber in human sclera. *Investigative Ophthalmology & Visual Science*, 11(10):816–821, 2019.

[81] Kielty, C. M., Sherratt, M. J., and Shuttleworth, C. A. Elastic fibres. *Journal of Cell Science*, 115:2817–2828, 2002.

[82] Kimball, E. C., Nguyen, C., Steinhart, M. R., Nguyen, T. D., Pease, M. E., Oglesby, E. N., Oveson, B. C., and Quigley, H. A. Experimental scleral cross-linking increases glaucoma damage in a mouse model. *Experimental eye research*, 128:129–140, 2014. ISSN 10960007. doi: 10.1016/j.exer.2014.08.016. URL `http://dx.doi.org/10.1016/j.exer.2014.08.016`.

[83] Knepper, P. A., Goossens, W., Hvizd, M., and Palmberg, P. F. Glycosaminoglycans of the human trabecular meshwork in primary open-angle glaucoma. *Investigative Ophthalmology & Visual Science*, 37(7):1360–1367, 1996.

[84] Lai, W., Hou, J., and Mow, V. A triphasic theory for the swelling and deformation behaviors of articular cartilage. *Journal of Biomechanical Engi- neering*, 113(3):245–258, 1991.

[85] Lanir, Y. A structural theory for the homogeneous biaxial stress-strain relationships in flat collagenous tissues. *Journal of Biomechanics*, 12(6):423–436, 1979.

[86] Lari, D. R., Schultz, D. S., Wang, A. S., Lee, O.-T., and Stewart, J. M. Scleral mechanics: comparing whole globe inflation and uniaxial testing. *Experimental eye*

research, 94(1):128–35, 2012. ISSN 1096-0007. doi: 10.1016/j.exer.2011.11.017. URL http://www.sciencedirect.com/science/article/pii/S0014483511003927.

[87] Lewis, P. N., Pinali, C., Young, R. D., Meek, K. M., Quantock, A. J., and Knupp, C. Structural Interactions between Collagen and Proteoglycans Are Elucidated by Three-Dimensional Electron Tomography of Bovine Cornea. *Structure/Folding and Design*, 18(2):239–245, 2010. ISSN 0969-2126. doi: 10.1016/j.str.2009.11.013. URL http://dx.doi.org/10.1016/j.str.2009.11.013.

[88] Lindahl, U., Couchman, J., and Kimata, K. Proteoglycans and Sulfated Glycosaminoglycans. In Varki, A., Cummings, R., and Esko, J., editors, *Essentials of Glycobiology*, chapter 17. Cold Spring Harbor Laboratory Press, New York, 3 edition, 2017. doi: 10.1101/glycobiology.3e.017. URL https://www.ncbi.nlm.nih.gov/books/NBK453033/.

[89] Malik, N. S., Moss, S. J., Ahmed, N., Furth, A. J., Wall, R. S., and Meek, K. M. Ageing of the human corneal stroma: structural and biochemical changes. *Biochimica et Biophysica Acta (BBA)-Molecular Basis of Disease*, 1138(3):222–228, 1992.

[90] Marcus, M. W., de Vries, M. M., Montolio, F. G. J., and Jansonius, N. M. Myopia as a risk factor for open-angle glaucoma: {A} systematic review and meta-analysis. *Ophthalmology*, 118(10):1989–1994, 2011.

[91] Markov, P. P., Eliasy, A., Pijanka, J. K., Htoon, H. M., Paterson, N. G., Sorensen, T., Elsheikh, A., Girard, M. J. A., and Boote, C. Bulk changes in posterior scleral collagen microstructure in human high myopia. *Molecular Vision*, 24(June):818–833, 2018.

[92] Mathews, M. B. and Decker, L. The effect of acid mucopolysaccharides and acid

mucopolysaccharide-proteins on fibril formation from collagen solutions. *Biochemical Journal*, 109:517–526, 1968.

[93] Maurice, D. M. The structure and transparency of the cornea. *The Journal of Physiology*, 136(2):263–286, 1957.

[94] Mcbrien, N. A. and Gentle, A. Role of the sclera in the development and pathological complications of myopia. *Progress in Retinal and Eye Research*, 22(3):307–338, 2003.

[95] McBrien, N. A., Cornell, L. M., and Gentle, A. Structural and ultrastructural changes to the sclera in a mammalian model of high myopia. *Investigative Ophthalmology & Visual Science*, 42(10):2179–2187, 2001.

[96] Meyer, A. and Silberberg, A. In Vitro Study of the Influence of Some Factors Important for any Physicochemical Characterization of Loose Connective Tissue in the Microcirculation. *Microvascular Research*, 8(3):263–273, 1974.

[97] Miehe, C., Goktepe, S., and Lulei, F. A micro-macro approach to rubber-like materials–Part I: the non-affine micro-sphere model of rubber elasticity. *Journal of the Mechanics and Physics of Solids*, 52(11):2617–2660, 2004. ISSN 00225096. doi: 10.1016/j.jmps.2004.03.011. URL `http://linkinghub.elsevier.com/retrieve/pii/S0022509604000808`.

[98] Miller, B. F., Olesen, J. L., Hansen, M., Døssing, S., Crameri, R. M., Welling, R. J., Langberg, H., Flyvbjerg, A., Kjaer, M., Babraj, J. A., Smith, K., and Rennie, M. J. Coordinated collagen and muscle protein synthesis in human patella tendon and quadriceps muscle after exercise. *The Journal of Physiology*, 567(3):1021–1033, 2005. ISSN 00223751. doi: 10.1113/jphysiol.2005.093690. URL `http://doi.wiley.com/10.1113/jphysiol.2005.093690`.

[99] Minckler, D. S., Bunt, A. H., and Johanson, G. W. Orthograde and retrograde axoplasmic transport during acute ocular hypertension in the monkey. *Investigative Ophthalmology & Visual Science*, 16(5):426–441, 1977.

[100] Moses, R., Grodzki, W., and Starcher, B. Elastin content of the scleral spur, trabecular mesh, and sclera. *Investigative Ophthalmology & Visual Science*, 17(8):817–818, 1978.

[101] Mubyana, K. and Corr, D. T. Cyclic Mechanical Loading Improves Tensile and Failure Properties of Scaffold-Free Engineered Tendon Fibers. In *International Symposium on Ligaments and Tendons*, pages 16–18, Orlando, 2016.

[102] Muir, H. Proteoglycans as organizers of the intercellular matrix. In *Seventeenth CIBA Medical Lecture*, pages 613–622. Biochemical Society Transactions, 1982.

[103] Murienne, B. J. *Glycosaminoglycan contribution to the structure-mechanical properties of the posterior sclera*. PhD thesis, 2016.

[104] Murienne, B. J., Jefferys, J. L., Quigley, H. A., and Nguyen, T. D. The effects of glycosaminoglycan degradation on the mechanical behavior of the posterior porcine sclera. *Acta Biomaterialia*, 12:195–206, 2014.

[105] Murienne, B. J., Jefferys, J. L., Quigley, H. a., and Nguyen, T. D. The effects of glycosaminoglycan degradation on the mechanical behavior of the posterior porcine sclera. *Acta Biomaterialia*, 12:195–206, 2015. ISSN 17427061. doi: 10.1016/j.actbio.2014.10.033. URL `http://linkinghub.elsevier.com/retrieve/pii/S174270611400484X`.

[106] Murienne, B. J., Chen, M. L., Quigley, H. A., and Nguyen, T. D. The contribution of glycosaminoglycans to the mechanical behaviour of the posterior human sclera. *Journal of The Royal Society Interface*, 13(119):20160367, 2016. ISSN 1742-5689. doi:

10.1098/rsif.2016.0367. URL `http://rsif.royalsocietypublishing.org/lookup/doi/10.1098/rsif.2016.0367`.

[107] Myers, K. M., Cone, F. E., Quigley, H. A., Gelman, S., Pease, M. E., and Nguyen, T. D. The in vitro inflation response of mouse sclera. *Experimental eye research*, 91 (6):866–875, 2010. doi: 10.1016/j.exer.2010.09.009.

[108] Myers, K. M., Cone, F., and Quigley, H. The Scleral Inflation Response of Mouse Eyes to Increases in Pressure . In *Society for Experimental Mechanics Series*, volume 2, pages 87–92, 2011. ISBN 9781461402190. doi: 10.1007/978-1-4614-0219-0.

[109] Newton, R. H. and Meek, K. M. Circumcorneal Annulus of Collagen Fibrils in the Human Limbus. *Investigative Ophthalmology & Visual Science*, 39(7), 1998.

[110] Nguyen, C., Cone, F. E., Nguyen, T. D., Coudrillier, B., Pease, M. E., Steinhart, M. R., Oglesby, E. N., Jefferys, J. L., and Quigley, H. A. Studies of Scleral Biomechanical Behavior Related to Susceptibility for Retinal Ganglion Cell Loss in Experimental Mouse Glaucoma. *Investigative Ophthalmology & Visual Science*, 54(3):1767–1780, 2013. doi: 10.1167/iovs.12-10952.

[111] Norman, R. E., Flanagan, J. G., Rausch, S. M. K., Sigal, I. A., Tertinegg, I., Eilaghi, A., Portnoy, S., Sled, J. G., and Ethier, C. R. Dimensions of the human sclera : Thickness measurement and regional changes with axial length. *Experimental Eye Research*, 90(2):277–284, 2010. ISSN 0014-4835. doi: 10.1016/j.exer.2009.11.001. URL `http://dx.doi.org/10.1016/j.exer.2009.11.001`.

[112] Norton, T. T. and Rada, J. A. Reduced Extracellular Matrix in Mammalian Sclera with Induced Myopia. *Vision Research*, 35(9):1271–1281, 1995.

[113] Nouri-mahdavi, K., Hoffman, D., Coleman, A. L., Liu, G., Li, G., Gaasterland, D., and Caprioli, J. Predictive Factors for Glaucomatous Visual Field Progression in the Advanced. *Ophthalmology*, 111(9):1627–1635, 2004. doi: 10.1016/j.ophtha.2004.02.017.

[114] Öbrink, B. A study of the interactions between monomeric tropocollagen and glycosaminoglycans. *European Journal of Biochemistry*, 33(2):387–400, 1973.

[115] Peña, E., Peña, J. A., and Doblaré, M. International Journal of Solids and Structures On the Mullins effect and hysteresis of fibered biological materials : A comparison between continuous and discontinuous damage models. *International Journal of Solids and Structures*, 46(7-8):1727–1735, 2009. ISSN 0020-7683. doi: 10.1016/j.ijsolstr.2008.12.015. URL `http://dx.doi.org/10.1016/j.ijsolstr.2008.12.015`.

[116] Pereira, P. N. R., Bedran-de Castro, A. K. B., Duarte, W. R., and Yamauchi, M. Removal of noncollagenous components affects dentin bonding. *Journal of Biomedical Materials Research Part B: Applied Biomaterials*, 80(1):86–91, 2007.

[117] Phillips, J. R. and McBrien, N. A. Form deprivation myopia: elastic properties of sclera. *Ophthalmic and Physiological Optics*, 15(5):357–362, 1995.

[118] Phillips, J. R., Khalaj, M., and Mcbrien, N. A. Induced Myopia Associated with Increased Scleral Creep in Chick and Tree Shrew Eyes. *Investigative Ophthalmology & Visual Science*, 41(8):2028–2034, 2000.

[119] Pijanka, J. K., Coudrillier, B., Ziegler, K., Sorensen, T., Meek, K. M., Nguyen, T. D., Quigley, H. A., and Boote, C. Quantitative Mapping of Collagen Fiber Orientation in Non-glaucoma and Glaucoma Posterior Human Sclerae. *Investigative Ophthalmology & Visual Science*, 53(9):5258–5270, 2012. doi: 10.1167/iovs.12-9705.

[120] Pijanka, J. K., Kimball, E. C., Pease, M. E., Abass, A., Sorensen, T., Nguyen, T. D., Quigley, H. A., and Boote, C. Changes in Scleral Collagen Organization in Murine Chronic Experimental Glaucoma. *Invest Ophthalmology Vis Sci.*, 55(10):6554–6563, 2014. doi: 10.1167/iovs.14-15047.

[121] Pinsky, P. M., Heide, D. V. D., and Chernyak, D. Computational modeling of mechanical anisotropy in the cornea and sclera. *Journal of Cataract & Refractive Surgery*, 31 (1):136–145, 2005. doi: 10.1016/j.jcrs.2004.10.048.

[122] Pogany, G., Hernandez, D. J., and Vogel, K. G. The \textit{in vitro} interaction of proteoglycans with type {I} collagen is modulated by phosphate. *Archives of Biochemistry and Biophysics*, 313(1):102–111, 1994.

[123] Quacci, D., Dell'Orbo, C., and Diaz, G. Collagen fibril ultrastructure alters after glycanolytic digestion. *Annals of Anatomy-Anatomischer Anzeiger*, 174(6):569–574, 1992.

[124] Quigley, H. A. Neuronal Death in Glaucoma. *Progress in Retinal and Eye Research*, 18(1):39–57, 1999.

[125] Quigley, H. A. New paradigms in the mechanisms and management of glaucoma. *Eye*, 19(12):1241–1248, 2005. doi: 10.1038/sj.eye.6701746.

[126] Quigley, H. A. and Anderson, D. R. The dynamics and location of axonal transport blockade by acute intraocular pressure elevation in primate optic nerve. *Investigative Ophthalmology & Visual Science*, 15(8):606–616, 1976.

[127] Quigley, H. A., Addicks, E. M., Green, W. R., and Maumenee, A. E. Optic nerve damage in human glaucoma. {II}. {T}he site of injury and susceptibility to damage. *Archives of Ophthalmology*, 99(4):635–649, 1981.

[128] Quigley, H. A., Dunkelberger, G. R., and Green, W. R. Retinal Ganglion Cell Atrophy Correlated With Automated Perimetry in Human Eyes With Glaucoma. *American Journal of Ophthalmology*, 107(5):453–464, 1989. ISSN 0002-9394. doi: 10.1016/0002-9394(89)90488-1. URL `http://dx.doi.org/10.1016/0002-9394(89)90488-1`.

[129] Quigley, H. A., Brown, A., and Dorman-pease, M. E. Alterations in elastin of the optic nerve head in human and experimental glaucoma. *British Journal of Opthamology*, 75 (9):552–557, 1991. doi: 10.1136/bjo.75.9.552.

[130] Quigley, H. A., Brown, A., and Dorman-Pease, M. E. Alterations in elastin of the optic nerve head in human and experimental glaucoma. *British Journal of Ophthalmology*, 75(9):552–557, 1991.

[131] Quigley, H. A., Dorman-Pease, M. E., and Brown, A. E. Quantitative study of collagen and elastin of the optic nerve head and sclera in human and experimental monkey glaucoma. *Current Eye Research*, 10(9):877–888, 1991.

[132] Quigley, H. A., Nickells, R. W., Kerrigan, L. A., Pease, M. E., Thibault, D. J., and Zack, D. J. Retinal ganglion cell death in experimental glaucoma and after axotomy occurs by apoptosis. *Investigative Ophthalmology & Visual Science*, 36(5):774–786, 1995.

[133] Quinn, K. P. and Winkelstein, B. A. Preconditioning is Correlated With Altered Collagen Fiber Alignment in Ligament. *Journal of Biomechanical Engineering*, 133(6): 064506, 2011. ISSN 01480731. doi: 10.1115/1.4004205. URL `http://biomechanical.asmedigitalcollection.asme.org/article.aspx?articleid=1406417`.

[134] Rada, J. A., Cornuet, P. K., and Hassell, J. R. Regulation of corneal collagen fibrillo-

genesis in vitro by corneal proteoglycan (lumican and decorin) core proteins. *Experimental eye research*, 56(6):635–648, 1992.

[135] Rada, J. A., Achen, V. R., Perry, C. A., and Fox, P. W. Proteoglycans in the Human Sclera Evidence for the Presence of Aggrecan. *Investigative Ophthalmology & Visual Science*, 38(9):1740–1751, 1997.

[136] Rada, J. A., Achen, V. R., Penugonda, S., Schmidt, R. W., and Mount, B. A. Proteoglycan Composition in the Human Sclera During Growth and Aging. *Investigative Ophthalmology & Visual Science*, 41(7):1639–1648, 2000.

[137] Rada, J. A., Achen, V. R., Penugonda, S., Schmidt, R. W., and Mount, B. A. Proteoglycan composition in the human sclera during growth and aging. *Investigative Ophthalmology & Visual Science*, 41(7):1639–1648, 2000.

[138] Rada, J. A., Shelton, S., and Norton, T. T. The sclera and myopia. *Experimental Eye Research*, 82:185–200, 2006. doi: 10.1016/j.exer.2005.08.009.

[139] Raspanti, M., Viola, M., Forlino, A., Tenni, R., Gruppi, C., and Tira, M. E. Glycosaminoglycans show a specific periodic interaction with type {I} collagen fibrils. *Journal of Structural Biology*, 164(1):134–139, 2008.

[140] Read, S. A., Collins, M. J., and Iskander, D. R. Diurnal Variation of Axial Length , Intraocular Pressure , and Anterior Eye Biometrics. *Investigative Ophthalmology & Visual Science*, 49(7):3–10, 2008. doi: 10.1167/iovs.08-1833.

[141] Reissner, E. On One-Dimensional Finte-Strain Beam Theory: the Plane Problem. *Journal of Applied Mathematics and Physics*, 23(5):795–804, 1972.

[142] Resnikoff, S., Pascolini, D., Etya, D., Kocur, I., Pararajasegaram, R., Pokharel, G. P.,

and Mariotti, S. P. Global data on visual impairment in the year 2002. *Bulletin of the World Health Organization*, 82(11):844–51, 2004.

[143] Rigozzi, S., Muller, R., Stemmer, A., and Snedeker, J. G. Tendon glycosaminoglycan proteoglycan sidechains promote collagen fibril sliding – AFM observations at the nanoscale. *Journal of Biomechanics*, 46(4):813–818, 2013. doi: 10.1016/j.jbiomech.2012.11.017.

[144] Sacks, M. S., Zhang, W., and Wognum, S. A novel fibre-ensemble level constitutive model for exogenous cross-linked collagenous tissues. *Interface Focus*, 6(1):20150090, 2015. ISSN 2042-8898. doi: 10.1098/rsfs.2015.0090. URL `http://www.scopus.com/inward/record.url?eid=2-s2.0-84951914776{&}partnerID=tZOtx3y1`.

[145] Sander, E. A. and Barocas, V. H. Comparison of 2D fiber network orientation measurement methods. *Journal of Biomedical Materials Research - Part A*, 88(2):322–331, 2009. ISSN 15493296. doi: 10.1002/jbm.a.31847.

[146] Sander, E. A., Barocas, V. H., and Tranquillo, R. T. Initial fiber alignment pattern alters extracellular matrix synthesis in fibroblast-populated fibrin gel cruciforms and correlates with predicted tension. *Annals of Biomedical Engineering*, 39(2):714–729, 2011. ISSN 00906964. doi: 10.1007/s10439-010-0192-2.

[147] Schultz, D. S., Lotz, J. C., Lee, S. M., Trinidad, M. L., and Stewart, J. M. Structural Factors That Mediate Scleral Stiffness. *Investigative Ophthalmology & Visual Science*, 49(10):4232–4236, 2008. doi: 10.1167/iovs.08-1970.

[148] Scott, J. E. Proteoglycan: collagen interactions and corneal ultrastructure. *Biochemical Society Transactions*, 19(4):877–881, 1991.

[149] Scott, J. E. and Bosworth, T. R. A comparative biochemical and ultrastructural study of proteoglycan-coliagen interactions in corneal stroma Functional and metabolic implications. *Biochemical Journal*, 270(2):491–497, 1990.

[150] Shapiro, S. D., Pierce, J. A., and Campbell, E. J. Marked longevity of human lung parenchymal elastic fibers deduced from prevalence of D- aspartate and nuclear weapons-related Find the latest version :. *The Journal of Clinical Investigation*, 87(5): 1828–1834, 1991.

[151] Shelton, L. and Rada, J. S. Effects of cyclic mechanical stretch on extracellular matrix synthesis by human scleral fibroblasts. *Experimental Eye Research*, 84(2):314–322, 2007. doi: 10.1016/j.exer.2006.10.004.

[152] Siegwart, J. T. and Norton, T. T. Regulation of the mechanical properties of tree shrew sclera by the visual environment. *Vision Research*, 39(2):387–407, 1999.

[153] Sommer, A., Tielsch, J. M., Katz, J., Quigley, H. A., Gottsch, J. D., Javitt, J., and Singh, K. Relationship between intraocular pressure and primary open angle glaucoma among white and black Americans: {T}he Baltimore Eye Survey. *Archives of Ophthalmology*, 109(8):1090–1095, 1991.

[154] Sopakayang, R. and Vita, R. D. Medical Engineering & Physics A mathematical model for creep , relaxation and strain stiffening in parallel-fibered collagenous tissues. *Medical Engineering and Physics*, 33(9):1056–1063, 2011. ISSN 1350-4533. doi: 10.1016/j.medengphy.2011.04.012. URL `http://dx.doi.org/10.1016/j.medengphy.2011.04.012`.

[155] Steinhart, M. R., Cone, F. E., Nguyen, C., Nguyen, T. D., Pease, M. E., Puk, O., Graw, J., Oglesby, E. N., and Quigley, H. A. Mice with an induced mutation in collagen 8A2

develop larger eyes and are resistant to retinal ganglion cell damage in an experimental glaucoma model. *Molecular Vision*, 18:1093–1106, 2012.

[156] Susilo, M. E., Paten, J. A., Sander, E. A., Nguyen, T. D., and Ruberti, J. W. Collagen network strengthening following cyclic tensile loading. *Interface focus*, 6 (1):20150088, 2016. ISSN 2042-8898. doi: 10.1098/rsfs.2015.0088. URL `http://rsfs.royalsocietypublishing.org/content/6/1/20150088`.

[157] Sverdlik, A. and Lanir, Y. Time-Dependent Mechanical Behavior of Sheep Digital Tendons , Including the Effects. *Journal of biomechanical engineering*, 124(February 2002):78–84, 2002. doi: 10.1115/1.1427699.

[158] Thornton, I. L., Dupps, W. J., Roy, A. S., and Krueger, R. R. Biomechanical Effects of Intraocular Pressure Elevation on Optic Nerve / Lamina Cribrosa before and after Peripapillary Scleral Collagen Cross-Linking. *Investigative Ophthalmology & Visual Science*, 50(3):1227–1233, 2009. doi: 10.1167/iovs.08-1960.

[159] Tong, P. and Fung, Y.-c. The stress strain relationship for the skin. *Journal of Biomechanics*, 9(10):649–657, 1976.

[160] Tonge, T. K., Murienne, B. J., Alexander, S., and Rothkopf, W. Minimal Preconditioning Effects Observed for Inflation Tests of Planar Tissues. *Journal of Biomedical Engineering*, 135(11):114502, 2013. doi: 10.1115/1.4025105.

[161] Tonge, T. K., Ruberti, J. W., and Nguyen, T. D. Micromechanical Modeling Study of Mechanical Inhibition of Enzymatic Degradation of Collagen Tissues. *Biophysical Journal*, 109(12):2689–2700, 2015. ISSN 15420086. doi: 10.1016/j.bpj.2015.10.051. URL `http://dx.doi.org/10.1016/j.bpj.2015.10.051`.

[162] Tonge, T. K., Ruberti, J. W., and Nguyen, T. D. A micromechanical modeling study of the mechanical stabilization of enzymatic degradation of collagen tissues. pages 1–29, 2015.

[163] Tower, T. T., Neidert, M. R., and Tranquillo, R. T. Fiber alignment imaging during mechanical testing of soft tissues. *Annals of Biomedical Engineering*, 30(10):1221–1233, 2002. ISSN 00906964. doi: 10.1114/1.1527047.

[164] Trier, K. The Sclera. In *Advances in Organ Biology*, volume 10, pages 353–373. 2005. ISBN 0444509259. doi: 10.1016/S1569-2590(05)10013-5.

[165] Trier, K., Olsen, E. B., and Ammitzbøll, T. Regional glycosaminoglycans composition of the human sclera. *Acta Ophthalmologica*, 68(3):304–306, 1990.

[166] Vogel, K. G., Paulsson, M., and Heinegard, D. Specific inhibition of type I and type II collagen fibrillogenesis by the small proteoglycan of tendon. *Biochemical Journal*, 223 (3):587–597, 1984.

[167] Vurgese, S., Panda-Jonas, S., and Jonas, J. B. Scleral thickness in human eyes. *PloS one*, 7(1):e29692, 2012.

[168] Wang, M. and Corpuz, C. C. C. Effects of scleral cross-linking using genipin on the process of form-deprivation myopia in the guinea pig: a randomized controlled experimental study. *BMC ophthalmology*, 15(1):89, 2015.

[169] Watson, P. G. and Young, R. D. Scleral structure, organisation and disease. A review. *Experimental Eye Research*, 78(3):609–623, 2004. ISSN 00144835. doi: 10.1016/S0014-4835(03)00212-4.

[170] Wilson, W., Donkelaar, C. C. V., and Huyghe, J. M. Biphasic Swelling Theories for

Soft Hydrated Tissues. *Journal of Biomechanical Engineering*, 127(1):158–165, 2005. doi: 10.1115/1.1835361.

[171] Wong, F. F., Lari, D. R., Schultz, D. S., and Stewart, J. M. Whole globe inflation testing of exogenously crosslinked sclera using genipin and methylglyoxal. *Experimental Eye Research*, 103:17–21, 2012. ISSN 00144835. doi: 10.1016/j.exer.2012.06.010. URL `http://dx.doi.org/10.1016/j.exer.2012.06.010`.

[172] Wong, M., Siegrist, M., and Goodwin, K. Cyclic tensile strain and cyclic hydrostatic pressure differentially regulate expression of hypertrophic markers in primary chondrocytes. *Bone*, 33(4):685–693, 2003. ISSN 87563282. doi: 10.1016/S8756-3282(03)00242-4.

[173] Xue, M. and Jackson, C. J. Extracellular matrix reorganization during wound healing and its impact on abnormal scarring. *Advances in wound care*, 4(3):119–1136, 2015.

[174] Young, R. D. The Ultrastructural Organization of Proteoglycans and Collagen in Human and Rabbit Scleral Matrix. *Journal of Cell Science*, 74:95–104, 1985.

[175] Zareian, R., Church, K. P., Saeidi, N., Flynn, B. P., Beale, J. W., and Ruberti, J. W. Probing collagen/enzyme mechanochemistry in native tissue with dynamic, enzyme-induced creep. *Langmuir*, 26(12):9917–9926, 2010. ISSN 07437463. doi: 10.1021/la100384e.

[176] Zhang, W. and Sacks, M. S. Modeling the response of exogenously crosslinked tissue to cyclic loading : The effects of permanent set. *Journal of the Mechanical Behavior of Biomedical Materials*, 75(July):336–350, 2017. doi: 10.1016/j.jmbbm.2017.07.013.

Vita

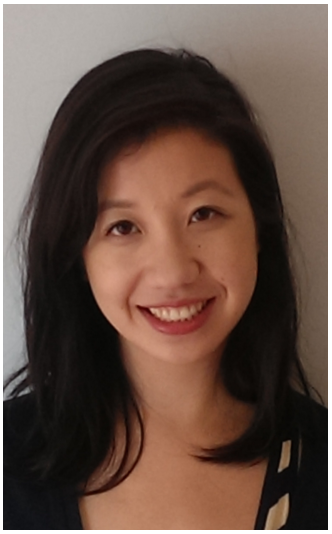

Michelle L. Chen was born in State College, Pennsylvania in 1990. She received her B.S. in Materials Science and Engineering from Northwestern University in 2012 and her M.S. in Materials Engineering from University of Illinois at Chicago in 2014. She joined Professor Nguyen's group at The Johns Hopkins University in 2014, to pursue a Ph.D. in Mechanical Engineering. Her research in ocular biomechanics and collagen network remodeling has been published in the *Journal of the Royal Society Interface* and the *Journal of the Mechanical Behavior of Biomedical Materials*. Starting in March 2019, she will begin employment as an Associate at Exponent in Natick, Massachusetts.